Fall 2020

Catalytic utilization of carbon dioxide as renewable feedstock for production of chemicals and fuels

Abbas Alaa Jawad

Department: Chemical and Biochemical Engineering

CATALYTIC UTILIZATION OF CARBON DIOXIDE AS RENEWABLE FEEDSTOCK FOR PRODUCTION OF CHEMICALS AND FUELS

by

ABBAS ALAA JAWAD

A DISSERTATION

Presented to the Faculty of Graduate School of the

MISSOURI UNIVERSITY OF SCIENCE AND TECHNOLOGY

In Partial Fulfillment of the Requirements for the Degree

DOCTOR OF PHILOSOPHY

in

CHEMICAL ENGINEERING

2020

Approved by:

Ali Rownaghi , Advisor
Muthanna Al Dahhan
Douglas Ludlow
Fateme Rezaei
Mark Fitch

PUBLICATION DISSERTATION OPTION

This dissertation has been prepared in the form of four articles, formatted in the style used by Missouri University of Science and Technology:

Paper I, Pages 24-55, have been published in Utilization CO_2 Journal.

Paper II, Pages 56-91, have been published in Catalysis Today Journal.

Paper III, Pages 92-126, have been submitted to Catalysis Today Journal.

Paper IV, Pages 127-173, will be submitted.

ABSTRACT

The utilization of CO_2 as a renewable feedstock for producing commodity chemicals and fuels is an interesting challenge to explore new concepts and opportunities in catalysis and industrial chemistry. This sustainable approach not only leads to production of useful chemicals, but also has the potential to mitigate anthropogenic CO_2 emissions to the atmosphere. CO_2 itself is a sustainable and inexhaustibly available carbon source, however, it is inextricably linked to its inherent inertness. It is a thermodynamically stable molecule (ΔG_f= -394.01 kJ.mol−1) with high oxidation state, hence, reactions of CO_2 must be combined with a high-energy reactant to gain a thermodynamic driving force. It has been shown that catalytic reaction is the best strategy to address this challenge. Although several processes for production of urea, methanol, and salicylic acid have been developed through CO_2 utilization, many of them rely on extremes of temperature and pressure to work. Owing to the growing energy demand and increasing atmospheric carbon dioxide (CO_2) concentration, it is desirable to identify effective hydrocarbon transformation reactions in tandem with CO_2 conversion. Research on direct transformation of light paraffins -such as methane, ethane and propane into light olefins -such as ethylene and propylene and aromatics has gained considerable importance recently because of its potential large-scale implementation for production of fine chemicals, pharmaceuticals, plastics and liquid fuels from C_1-C_4 hydrocarbons in the shale gas. The catalytic conversion of propane into propylene in the presence of CO_2 as a soft oxidant opens opportunities to simultaneously reduce CO_2 to CO and convert paraffin into value-added products.

ACKNOWLEDGMENTS

I would like to express my sincere gratitude to my supervisors, Dr. Ali Rownaghi, for his support. It would have been complicated to complete this dissertation without his support, understanding, and encouragement.

I wish to extend special appreciation to my committee members Dr. Muthanna Al Dahhan, Dr. Douglas Ludlow, Dr. Fateme Rezaei, and Dr. Mark Fitch.

I would like to thank the Higher Committee for Educational Development in Iraq (HCED) for their financial support. The authors would also like to acknowledge the Iraqi Ministry of Oil/ AL-Doura Refinery Company for their support.

I would like to thank Dr. Xin Li, Marktus Atanga, Busuyi Adebayo in Chemical and Biochemical Engineering Department and Dave Satterfield and Jonathon Sidwell in Chemistry Department and Dr. Eric Bohannan in Materials Research Center for their help and support

Finally, I would like to express my sincere gratitude to my wife, Sura, who has been my pillar of strength throughout this Ph.D. journey. Her support and patience made this whole process a wonderful journey. I would like to thank my daughters (Larean, Eva) and my son Yousif, who have been my bundle of joy. I would also like to thank my dad, mom, and brothers and sisters, who kept me encouraged from home.

TABLE OF CONTENTS

PAPER

LIST OF FIGURES

PAPER I Page

PAPER II

PAPER III

PAPER IV

LIST OF TABLES

PAPER IV

LIST OF SCHEMES

PAPER I Page

SECTION

1. INTRODUCTION

The significant challenge in the development of sustainable processes to produce valuable chemicals is the identification and efficient use of renewable resources. Carbon dioxide (CO_2) can be considered an ideal building block and inexhaustibly available carbon source since it is a by-product of fuel combustion and of many industrial processes and is thus inexpensive and widely available.[1] In this regard, catalytic installation of CO_2 [2] into energy-rich substrates, such as epoxides to produce cyclic carbonate or polycarbonates has attracted much attention. Therefore, the high CO_2 pressure was still required to implement a quantitative yield of cyclic carbonates.[3] The 100% atom efficient cycloaddition of *epoxides* and CO_2 to produce *five-membered cyclic* is most promising techniques.[4] Cyclic carbonate products can act as high-boiling polarity and aprotic solvents, main species for the preparation of polymeric species such as polycarbonates and polyurethanes.[5] Combining basic-acidic sites of bifunctional catalysts is commonly depending on merging low-cost species into chemically functionalize materials to activate the electrophilic and nucleophilic partners simultaneously.[6] Bifunctional catalysts can act as cooperative catalysts in presence basic-acidic sites can serve to cooperate catalysts for achieving higher reaction rates greater than those achieved using the catalytic species alone.[7] The catalysts have short lifetime and relatively high energy needs for recycling are obstacles of homogeneous catalysts that restrict their utilization in industrial applications. Therefore, the creation of more substantial heterogeneous catalysts based on

integrating acid and base sites, which interact with single support material instead of homogeneous catalysts. Recently, cyclic carbonates have been catalyzed by coupling with epoxides using organic amine molecules directly.[8] Among of supported amines have been adopted for synthesizing this type of reaction.[9,10] One primary advantage of this type of nonmetal-doped catalyst system is that it would not introduce metal contaminant(s) to products and the environment impacts. Nevertheless, the reaction mechanism and the role(s) of amine are not yet obvious. On the other hand, amines which are being used to adsorb CO_2; liquid amines, such as monoethanolamine, are widely utilized commercially for scrubbing CO_2 from gas streams. Amine molecules chemically bonded to a silica surface have also been observed to adsorb CO_2 with highly efficient regenerability and stability.

The utilization of CO_2 as a Building-block for synthesizing value-added chemicals has received attention due to reduction of CO_2 emissions and ocean acidification effects [11–14]. Dry reforming of methane (DRM) with CO_2 has paid attention because of utilization of two major greenhouse gases (CH_4 and CO_2) as useful chemical feedstocks, and provides a route to convert them into the low H_2/CO ratio syngas, which can be directly used as fuel or to produce chemicals and fuels by the methanol synthesis and Fischer-Tropsch (FT) processes. [15]

Oxidative dehydrogenation of propane (ODHP) is among promising alternative technologies that has attracted petrochemical players' attention to overcome the disadvantages. This process in contrast to nonoxidative pathways, is exothermic and the conversion becomes significant at a lower reaction temperature. [16,17]

2. LITERATURE REVIEW

2.1. CHALLENGE AND OPPORTUNITIES

The molecular transformation of carbon dioxide (CO_2) into value-added products has intrigued chemists ever since the advent of the area of catalysis. The "Sabatier reaction" converts a mixture of CO_2 and H_2 into methane, and its discovery has been pivotal in the development of the principle of catalysis in its modern understanding. The major challenge of "activating" a small and relatively unreactive molecule has stimulated the curiosity and creativity of generations of scientists. In particular, the ingenious and remarkably complex mechanism of nature's capability to build up enormous amounts of carbon based materials in very short periods of time solely on the basis of CO_2, water, and sunlight is still humbling the prodigious progress of modern synthetic chemistry. While capitalizing on this natural process indirectly through the utilization of today fossil resources forms the basis of our global energy system and material value chains, only very few chemical processes utilizing CO_2 as feedstock are of industrial relevance. In recent years, the interest in catalytic conversion of CO_2 has experienced a very dynamic growth.[18–22] This escalation results at least partly from scientific insight into the problems arising from continuous and ever-increasing emissions of CO_2 as waste material from fossil-based energy systems.[23] Remarkably, the utilization of a waste stream of one sector as feedstock for the value chain of another industry can be economically and ecologically attractive, contributing to the concept of a circular economy.[24] As Graedel [25] noticed, the sustainability is pointed to the rate of resource utilization and the rate of waste generation. In order to be sustainable a technology must fulfill two constraints: (i) natural resources

should be utilized at rates that do not unacceptably deplete supplies over the long term and (ii) residues should be generated at rates no higher than can be assimilated readily using the natural environment. With regard to that (i), it is perceptibly, for instance, that non-renewable fossil resources – oil, coal and natural gas – are being used at a much higher rate than they are replaced by natural geological processes and their use is, therefore, not sustainable in the long term. Furthermore, the use of fossil resources is generating carbon dioxide at rates that can't be assimilated by the natural environment and this is widely accepted to be a root cause of climate change. This marked discrepancy between the time scale of formation of natural resources and their exploitation is referred[26] to as the "ecological time-scale violation". The aim to reduce carbon dioxide emissions directly by converting CO_2 into chemicals or fuels has motivated a number of analyses on the potential amounts of CO_2 to be captured Among those surrogates, carbon dioxide gas, as the most abundant and important carbon source in the atmosphere, is much more attractive. CO_2 acts as an attractive C1 building block in organic synthesis since it is non-toxic, abundant, low cost, and recyclable, as well as an intrigued and appealing potential as a renewable source.[27] The conclusion one can draw from foregoing data is that to mitigate anthropogenic carbon dioxide emissions directly by converting CO_2 into chemicals or fuels has motivated a number of analyses on the potential amounts of anthropogenic CO_2 to be captured.[28] To put this in some perspective, is motivated by searching for solutions to quantitatively reduce carbon dioxide emissions of the fossil-based energy system. Given the different scales of the energy sector and the material value chain, it should go without saying that the production of CO_2-based organic chemicals cannot provide a quantitative "sink" for carbon dioxide to reduce substantially the enormous CO_2 emissions from fossil

power generation. Producing liquid fuels for transportation needs much more carbon and could therefore demand significant amounts of CO_2. However, the combustion of the fuel generates the equivalent amount of carbon dioxide and therefore does not lead to a direct net "consumption" of CO_2. But even if CO_2 conversion can't provide a silver bullet to solve the CO_2 mitigation problem, there are still very better reasons why CO_2 conversion will play synergistic role in moving towards a sustainable future. (1) CO_2 conversion for a less carbon-intensive and more benign chemical industry. The focus on the global challenge of CO_2 mitigation is important, but it should not prevent us from identifying the potential benefit of CO_2 utilization for the chemical value chain. From this viewpoint, the question to be asked is as follows: Can the use of CO_2 as feedstock reduce the carbon footprint and environmental impact of chemical production? The efforts to minimize the carbon footprint of the petrochemical industry via process optimization and intensification are reaching ever-higher maturity, already approaching in certain cases saturation. Alternative feedstocks such as CO_2 (or biomass[29]) come into view to open new doors for disruptive changes. Hereby, the contribution of CO_2 conversion could be realized by two distinct approaches: First, CO_2 can be funneled into the existing treelike structure of the chemical industry at different positions via certain key components such as carbon monoxide, methanol, etc. Second, novel synthetic routes can be opened using a different coupling of starting materials and reagents whereby CO_2 serves as a C1 building block. In both cases, potential advantages from using CO_2 can go significantly beyond the reduction of rescaled global warming impact by addressing other crucial environmental impacts such as mitigating fossil resource depletion or providing access to more benign production pathways. (2) CO_2 conversion for the production of synthetic fuels. As aforementioned,

is very useful for the chemical sector, wherein the individual molecular structures identify their use and lifetime. This is different for transportation fuels, where the point of reference is not a given molecular structure, but the function of the fuel to provide effective and clean propulsion. This function could be fulfilled by a wide range of possible molecular fuel components and shifting the raw material and energy input from fossil to renewable expands the molecular diversity even further. This new degree of freedom of "fuel design" should be optimized to the overall well-to-wheel environmental footprint associated with the propulsion efficacy as the function is served best.[30] As result, the question to be asked here would be as follows: Can CO_2 serve effectively as an energy vector to harvest renewable electricity into the mobility and transportation sector? Again, two scenarios may be distinguished: First, CO_2 and renewable hydrogen can be utilized to produce hydrocarbons that are largely identical to today's pool of fuels (gasoline, diesel, or liquefied natural gas, LNG). Second, the opportunity to produce novel molecular structures can lead to advanced fuels, allowing combination of reductions in global warming impact with enhancements in other highly relevant impact categories such as local pollutant emission. In the present review, we address the above two questions regarding the potential role of CO_2 conversion for a sustainable development in an interdisciplinary approach between chemistry and systems engineering from a life cycle perspective.

2.2. CARBON DIOXIDE AS A BUILDING BLOCK FOR CHEMICAL STRUCTURE

2.2.1. Cyclic Carbonate. Cyclic carbonates have general structure[31] and the most important cyclic carbonates contain a five-membered ring [32]. Among these alternatives, the reaction of CO_2 with epoxides, which can lead to the formation of cyclic carbonate

product, is an important chemical reaction, making use of CO_2 as a renewable feedstock. Such cyclic carbonate synthesis from CO_2 and epoxide is an important subject in catalytic chemistry.[33–36] Compounds have many applications including as polar aprotic solvents1,2 capable of replacing traditional solvents such as N,N-dimethylformamide (DMF), Dimethyl sulfoxide (DMSO), N-methylpyrrolidinone (NMP) and acetonitrile which are likely to be banned under the European REACH regulations and which generate NO_x or SO_x when incinerated.[37] The direct conversion of CO_2 to five- or six-membered cyclic carbonates[38,39]is one of the most promising strategies for producing highly desirable solvents that are used as the electrolytes in lithium-ion batteries which power a profusion of portable electronic devices and are increasingly used in electric vehicles.[40,41] Cyclic carbonates are also intermediates in the synthesis of other small molecules[42] and polymers.[43] Cyclic carbonates have wide industrial applications such as in the pharmaceutical and fine chemical industries, and also play a crucial role as an intermediate for the synthesis of fuel additives.[44,45] Although the copolymerization of CO_2 with epoxides over homogeneous catalysts has been well-definition since 1969 and huge steps in homogeneous catalysis have been researched over the last years [46], the separation of catalyst from the reactants and products is a significant challenge which typically requires more energy input and results in the decomposition of the homogeneous catalysts.[47,48] The facile ability to separate and recycle heterogeneous catalysts from reactive fluids makes them attractive targets for incorporating acid–base cooperativity in new materials.[49,50] Among a number of heterogeneous catalysts such as metal oxides (e.g., MgO, FeO, CaO, ZnO, Zr_2O, La_2O_3, CeO_2, and Al_2O_3)[48,51,52], porous organic polymers (POPs)[52,53], metal organic frameworks (MOFs)[54–56], polymeric/supported ionic liquids[3,57], and cooperative

catalysts[7] have been developed to catalyze the copolymerization of CO_2 with epoxides for the synthesis of cyclic carbonates, at present the most important and commercial route to cyclic carbonates is the 100%. The proposed reaction mechanism for cycloaddition between an epoxide and carbon dioxide catalyzed by Br/APS/Zr-PAIHFs catalyst.[52] Thus, the catalyst will optionally provide a Lewis- or Brønsted acid to activate the epoxide. The catalyst then always provides a good nucleophile to ring-open the (activated) epoxide (A), forming an alkoxide (B) which reacts with carbon dioxide to form a carbonate (C). The nucleophile provided by the catalyst must also be a good leaving group as in the final step of the mechanism this is displaced intramolecularly by the carbonate to form the five-membered ring and regenerate the catalyst.[58] Halides (especially e.g., Br^-, I^-) make as the most useful bifunctional catalysts for the cooperatively catalyzing CO_2 cycloaddition contain a halide as part of their structure.[59–61]. Jadhav et al.[62] studied the effect of various anions such as Cl^-, Br^-,BF_4^-,PF_6^-, and NTf_2^- on polymer-supported ionic liquids (PSILs). It was shown that PSIL-NTf_2 was the most efficient catalyst exhibiting 100% conversion and 91% yield of the respective cyclic carbonate under 100 °C reaction temperature and 8 bar pressure in 8 h reaction time. Repo and co-workers[63,64] synthesized bifunctional Schiff base iron (III) complex and assessment as an intramolecular catalyst for cyclic carbonates synthesis from CO_2 coupling with epoxides. It was found that Lewis acidic iron center and Lewis basic imidazoles can activate the coupling reaction of propylene oxide (PO) and CO_2 without an additional co-catalyst even though the iron compound acts as a monomolecular catalyst. In another study, the cooperative action of MgII and Br^- in bifunctional Mg (II) Porphyrin catalyst was depicted to enhance the cyclic carbonate formation from epoxides and CO_2[65]. Recently, we illustrated the concept of cooperative organo-catalysis based on

polymer hollow fiber support and its usage for chemical transformation[7,66]. Building from the previous research conducted on both homogeneous and heterogeneous catalysts, we have hypothesized that porous polymeric hollow fibers can provide new design elements that are challenging to employ with homogeneous catalysts. Porous polymeric hollow fibers are pseudo monolithic materials that have great potential to make the reaction more reactive and attractive by creating a high surface area to volume ratio, increase in flow pattern reliability for scale-up, and the ability to tune mass transfer resistances. This type of porous hollow fiber is readily available and inexpensive which makes such a catalyst highly attractive in the context of green chemistry and in view of potential large-scale applications.[58] Therefore, the high CO_2 pressure was still required to implement a quantitative yield of cyclic carbonates.[3] Furthermore, structure and synthetization of functionalized heterogeneous materials for efficient CO_2 activation and subsequent conversion under mild conditions is still urgently required. The 100% atom efficient cycloaddition of *epoxides* and CO_2 to produce *five-membered cyclic* is most promising techniques.[4] Cyclic carbonate products can act as high-boiling polarity and aprotic solvents, main species for the preparation of polymeric species such as polycarbonates and polyurethanes.[5] Combining basic-acidic sites of bifunctional catalysts is commonly depending on merging low-cost species into chemically functionalize materials to activate the electrophilic and nucleophilic partners simultaneously.[6] Bifunctional catalysts can act as cooperative catalysts in presence basic-acidic sites can serve to cooperate catalysts for achieving higher reaction rates greater than those achieved using the catalytic species alone.[7] The catalysts have short lifetime and relatively high energy needs for recycling are obstacles of homogeneous catalysts that restrict their utilization in industrial

applications. Therefore, the creation of more substantial heterogeneous catalysts based on integrating acid and base sites, which interact with single support material instead of homogeneous catalysts. Recently, cyclic carbonates have been catalyzed by coupling with epoxides using organic amine molecules directly.[8] Among of supported amines have been adopted for synthesizing this type of reaction.[9,10] One primary advantage of this type of nonmetal-doped catalyst system is that it would not introduce metal contaminant(s) to products and the environment impacts. Nevertheless, the reaction mechanism and the role(s) of amine are not yet obvious. On the other hand, amines which are being used to adsorb CO_2; liquid amines, such as monoethanolamine, are widely utilized commercially for scrubbing CO_2 from gas streams. Amine molecules chemically bonded to a silica surface have also been observed to adsorb CO_2 with highly efficient regenerability and stability. Kozak et al.[67] it can be seen that the mechanistic investigation and continuous-flow catalytic system for chemical transformation that demands only catalytic quantities of feedstock chemicals, bromine itself or a combination of N-bromosuccinimide (NBS) and benzoyl peroxide (BPO) in N,N-dimethylformamide (DMF), the conversion of epoxides coupling with CO_2 to produce cyclic carbonates that were of 86% and N-methyltetrahydropyrimidine was found to catalyze gas transfer of CO_2 to medium solution to catalyze with n-butyl glycidyl ether to produce cyclic carbonate. In this study, Lewis acid/base species and nucleophilic parts have been development of cooperative catalyst, which are immobilized in the pores of a polyamide-imide (PAI) hollow fiber support was investigated. The porous Br/APS/Zr-PAIHF catalyst was emerged by crosslinking of bare ZrO_2-PAIHF polymer with 3-aminopropyltrimethoxysilane (APS) followed by alkylation with 1,2-dibromoethane at 110 °C, thereby further immobilized with nucleophilic bromide

ions and highly stability of solvent. Porous ZrO_2-PAIHF provides a physical restriction to suppress cooperative Lewis acid/base species and nucleophilic parts mobility, assemblage, and released from the support towards the product stream. The reactivity of Br/APS/Zr-PAIHFs as a heterogeneous catalyst for CO_2 cycloaddition to styrene oxide (SO) reaction, resulting in synthesis of styrene carbonate (SC). The reaction was carried out several reaction factors involving reaction temperature, reaction time, impact of solvent, and influence of CO_2 pressure were tested. The obtained data implied that the decisive interaction impact of nucleophilic bromide ion (Br^-) and Lewis acid/base species on PAI-HF supports; thus a maximum SC selectivity of 99%. As well as, SO conversion and SC selectivity were of 100 and 98%, respectively over Br/APS/Zr-PAI-HF catalyst as illustrated in paper I.

2.2.2. Conversion CO_2 to Syngas. Recently, the production of synthesis gas (syngas) via carbon dioxide dry reforming has received renewed attention because of environmental concerns and the clear need to minimize GHGs (Green House Gases) emissions. The syngas produced using dry reforming has a lower H_2/CO ratio, being preferred for the production of valuable oxygenated chemicals and long chain hydrocarbons.[68] Dry reforming can also be used in chemical energy transmission systems (CETS) based on the high endothermicity of this reaction.[69] A previous review article of CO_2 reforming of methane was done by[70] which presented a comprehensive review of the thermodynamics, catalyst selection and activity, reaction mechanism, and kinetics of this reaction. Since then, there is extensive research on the CO_2 reforming of methane, in particular on the Ni-based catalysts. It is mostly common catalyst used in the industries. This review was conducted to identify the gap in the reaction process and the ways to

overcome the problems especially coke deposition associated with Ni-based catalysts. Coke formation and sintering of catalyst are the primary causes of catalyst deactivation that could lead to decline the conversion of reactants. Hence, it is timely to provide a comprehensive review on the CO_2 reforming of methane over Ni-based catalysts. The literature was selected based on current developments in the CO_2 reforming of methane to improve the catalytic activity and increase the conversion of CO_2 and CH_4, respectively. The review also comprises of thermodynamic analysis for the reaction process, the development of catalyst, and the outlook for future research associated with DRM. Carbon dioxide (CO_2), which is one of the main contributors to the greenhouse effect, can be utilized as a mild oxidant for the selective oxidation of hydrocarbons. Dehydrogenation of alkanes by CO_2 to olefins is a promising alternative to dehydrogenation and oxidative dehydrogenation (ODH) by oxygen, which suffer from either coking problems or over-oxidation. CO_2 has also been noticed to be an effective oxidant in the oxidative coupling of methane (OCM) to ethane (C_2H_6) and ethylene (C_2H_4), the ODH of C_2-C_4 alkanes to alkenes, the dehydroaromerization of lower hydrocarbons (methane (CH_4), C_2H_6, and propane (C_3H_8)) to benzene (C_6H_6), and the ODH of ethylbenzene (EB) to styrene. For all these reactions, several efficient catalyst systems have been developed, and their redox property dominates the catalytic performance. In those reactions, CO_2 can have different roles, depending on the catalyst systems and reactions: (i) CO_2 can produce active oxygen species; (ii) CO_2 reoxidizes the reduced oxides, forming the redox cycle; and (iii) CO_2 oxidizes the carbon species, reducing coking. However, few investigations have been conducted in the past to explore the reaction mechanism for those reactions, and the active sites for hydrocarbon activation are still under debate. Therefore, it is recommended that

the future research should be more focused on reaction mechanisms and kinetics, to provide more information on the catalyst design. For CH_4 coupling with CO_2, more efficient catalyst systems should be developed to meet the theoretical prediction. In CO_2 dehydrogenation and dehydroaromerization of lower alkanes to alkenes, deactivation of the catalyst is a problem for developing new catalyst systems with long-term stable performance.[71] However, DRM is an endothermic and very energy serve reaction and is usually conducted at very high operation temperature (>800 °C). Another major drawbacks for long-term operation of DRM reaction is catalyst deactivation due to severe carbon deposition. [72–74] In that regard, significant efforts have been dedicated to the development of metal catalysts using modifying chemical composition, supports, promoters, different preparation methods/conditions and morphology to bear high catalytic performances toward syngas formation from DRM. Over the past few decades, the majority of the catalysts investigated for DRM are generally made up of Group 8 transition metals due to their high activity and low price. [72–74] Promoting nickel-based catalysts with various metals such as Zr, Cr, Ce, V, Mo, Rh, Pt, Pd and Ru is the most widely practiced approach for modifying DRM catalysts. In particular, nobel metals (i.e. Pt, Rh, and Ru) show high reactivity towards DRM which enhance stability against carbon formation as compared to the other non-promoted nickel-based catalysts. The performance of catalyst has been observed to be dependent upon the ratio of Ni/metal and the behavior of the support. In particular, it has been shown that Ni catalyst is highly reducible in presence of noble metals which enables both methane combustion and reforming to occur simultaneously, thereby resulting in higher energy efficiency and enhanced performance of catalyst. Both promoters and support play important roles in metal electron transfer, cluster stabilization,

and reducibility [2]. Although noble metals have been observed to be much more coke resistance than other metal-based catalysts, they are generally uneconomical. On the contrary, developing bimetallic catalysts via combining nickel with other metals is an alternative route to highly create coke-resistant Ni-based catalysts for DRM reaction. Several studies have been dedicated to improving the Ni-based CeO_2-Al_2O_3 performance and stability through addition of second metal promoters such as Co, Pd, Pt. It has been confirmed that adding a trace of transition metals can modify Ni surface properties by promoting the reducibility of Ni and thus increasing the number of active sites to achieve better catalytic performance. For example, several bimetallic catalysts such as Ni-Co, Ni-Pd and Ni-Pt with different supports (e.g., SiO_2, Al_2O_3, CeO_2, MgO, TiO_2, ZrO_2, HZSM-5) exhibited a much higher performance and carbon resistance for Ni-based catalyst than monometallic of Ni catalyst [75–77].

2.2.2.1. Ni-based catalysts for DRM. Nickel and noble metals are widely utilized as active metals in reforming catalysts. Noble-metal-supported catalysts (Rh, Ru, Pd, Pt, and Ir) have shown promising catalytic activity in terms of conversion and selectivity in dry reforming. Due to their high cost and limited availability, however, noble metals are not suitable for industrial applications. An alternative metal such as transition metals, alkaline earth metals, and nickel are more commonly used as the active metal in reforming processes because of its relative abundance and low cost.[78] Nevertheless, the major drawback is that nickel easily induces carbon formation thus, leads to catalytic deactivation. Therefore, numerous studies have been carried out to enhance the catalytic activity and stability of nickel-based catalysts in reforming processes.[79] The addition of second metal can enhance dispersion of the active metal and adjust the interaction between

Ni and the support species, besides increase the performance of catalyst such supports with basic character, such as MgO, CaO, Mo, and Fe_2O_3[80], which has small number of Lewis acid sites as well as redox promoter/supporter such like CeO_2, and ZrO_2, which has high oxygen mobility and thermal stability, thereby resulting in that have been enhanced the adsorption and dissociation of acidic CO_2 take place on the surface of the catalyst support,[58] and thus release carbon and resist the accumulation of carbon.[81] To commercialize DRM reaction in the industries, the development of cheap and cost-effective catalysts that have high activity and high resistance to carbon formation is the prime concern. Researchers have conducted investigations on the type of support used [82] and the impact of adding promoters to Ni-based catalysts to find the best way to refine its resistance to carbon formation. Moreover, recent attempts to improve catalytic performance and inhibit carbon formation have been carried out by combining two or three metals as active sites.[83] Preparation technique and catalyst pretreatment process also play a synergistic effect in the change of structural properties, the reduction behavior, and also the catalytic activity.

2.2.2.2. Role of the support on catalyst activity. DRM has been studied over a series of supported Pt, Pd, Rh, and Ru catalysts [84][85] and other supported transition metals like Co and Fe.[86][87] The most widely used metal for this reaction is Ni,[88][89] but many Ni-based catalysts undergo severe deactivation due to carbon deposition and subsequent loss of activity over time.[90] A number of supports for these active metals have also been investigated, including SiO_2, La_2O_3, ZrO_2, TiO_2, CeO_2, Al_2O_3, and MgO. The activity, kinetics, and mechanistic steps over these various catalysts have been investigated in order to attenuate carbon deposition and other mechanisms of deactivation.[91] There is a strong

agreement in the literature that the mechanism of DRM is bi-functional: CH_4 is activated on the metal and CO_2 activates on an acidic/basic supports. For catalysts supported on relatively inert materials like SiO_2, the mechanism is thought to follow a mono-functional pathway, where both reactants are activated by the metal alone. On acidic supports CO_2 activates by formation of formates with the surface hydroxyls and on basic supports by forming oxy-carbonates.[92] However, on inert supports, once carbon deposition occurs by dehydrogenation of methane, proceeding activation of CO_2 and reaction with carbon is limited, leading to inactivity of the catalyst.[92] Thus catalysts based on inert supports like SiO_2 have relatively weak metal–support interaction and are less stable and less active compared to the mildly acidic (Al_2O_3) or basic (like La_2O_3, CeO_2,Mg) supports.[93] This weaker interaction between metal and inert supports has an advantage over acidic/basic supports and is reported to refine the metal–metal interaction in case of bimetallic catalysts. For example, Pino et al.[94] investigated the performance catalyst enhancement by 5 at.% (~1.76 wt.%) Ni based catalysts supported on CeO_2 and on La-doped ceria to improve the catalyst activity: the CH_4 and CO_2 conversion reaches 96% and 86.5%, respectively. Strong and extensive interactions nickel–lanthana–surface oxygen vacancies of ceria, which induce the formation of Ce^{3+} sites and enhance the Ni dispersion, can promote the catalytic activity. The presence of intermediate and strong basic sites created by lanthana addition determines more strongly interactions of CO_2 with the catalyst surface enhancing the catalyst activity. Miguel et al.,[95] found formation of Pt-Ni bimetallic cluster which augmented the reducibility of Ni, resulting in higher and more stable activity for over 6500 min. This suggests that not only the nature of the support is important but the complex interfacial site chemistry and the particular active metal-support combination is very

crucial for catalysis of DRM.[96] Other than being directly involved in the reactant activation process on its acidic or basic sites, the supports also play an indirect role in the reaction mechanism by impacting the metal particle size or metal dispersion.[97] Sokolov et al.[98] synthesized a series of supported Ni catalysts to observe the impact of the support materials on the catalysts' activity. The study was conducted using Ni/Al_2O_3, Ni/MgO, Ni/TiO_2, Ni/SiO_2, Ni/ZrO_2, Ni/La_2O_3-ZrO_2 and Ni supported on mixed-metal oxides (Ni/Siral 10 and Ni/PuralMG30) at low temperature (400 ^oC). From the experiment, catalysts containing Zr within the support demonstrated the highest initial activities. Ni/La_2O_3-ZrO_2 yielded CO and H_2 that is close to equilibrium, and they displayed the highest stability, followed by Ni/ZrO_2. Although Ni/SiO_2 catalyst had the highest specific surface area, the initial yield of H_2 was the lowest followed by Ni/Al_2O_3, Ni/MgO, and Ni/TiO_2. Nevertheless, it is remarkable for Ni/MgO to implement an initial H_2 yield of 2.5% considering that the catalyst had low surface area. Typically, the activity of the catalysts (based on H_2 yield) can be reordered as: Ni/La_2O_3-ZrO_2 > Ni/ZrO_2 > Ni/PuralMG30 > Ni/Siral 10 > Ni/TiO_2 > Ni/MgO > Ni/Al_2O_3 > Ni/SiO_2. To have a better understanding of the resistance of the catalyst towards deactivation, the yield of H_2 at 0 h and at 100 h time-on-stream were compared. It is observed that Ni/La_2O_3-ZrO_2 had the highest stability with only 9% loss of H_2 yield from the initial state. The least stability of catalyst with the loss of 20% of H_2 yield was Ni/ZrO_2 and 89% of H_2 yields was Ni/TiO_2. The enhancement Ni-support interaction on mesoporous La_2O_3-ZrO_2 probably emerges from partial encapsulation of NiO_x species by mesopores during the preparation of the catalyst which resulted in a formation of strong chemical bonding that has a greater portion of each Ni particle in following steps.[98]

2.2.2.3. Effect promoter on catalytic activity. Several works have demonstrated that dry reforming of methane proceeds easily with Rh, Ir, Ru, and Pt catalysts. Nevertheless, the utilization of noble metals at industrial scale is difficult due to the limited resource and high price. In 1993, Rostrup-Nielsen and Hansen[99] compared the activity of Ni and a series of noble metal catalysts for dry reforming of methane; it was performed that Ni possessed similar activity as noble metals, but coke formation on Ni catalyst was a major drawback. A noble material promoter such as Pt can suppress sintering from occurring which provides better performance of the catalyst. Wu at el.[100] pointed out that sintering also causes the catalyst to deactivate. During the calcination of the catalyst, when Pt is integrated as a promoter in 4 wt% Ni catalysts supported over Al_2O_3 were studied in the dry reforming of methane (DRM), their structure is changed, thereby affecting the catalyst performance. The interaction of Pt from the promoter Ni catalysts at a structural level lowers the sintering resistance. The competition between Pt and Ni during the interaction aids in the formation of reducible Ni species. The concentration of Pt affects the conversion of CO_2 and CH_4 in DRM reaction. For instance, lower concentrations of Pt formed ionic oxides strongly and increased the conversion of CH_4. Besides promoting with Pt, the addition of potassium Au as a promoter to Ni-based catalysts was also reported by Wu at el.[100] leads to formation of a synergistic interaction, which induces easy reduction of NiO species and reduce of particle size. This kind of interaction leads to both effects, improved reduction of NiO species and enhanced catalytic activity of the bi-/trimetallic catalysts. The carbon accumulation on the surface of the catalysts depends on the composition of the active sites (NiAu, NiPt, NiAuPt). Moreover, a direct relation between catalytic activity and typology/amount of carbonaceous species was observed.

The best catalyst NiAuPtAl is the ones with the better combination of these two parameters (high amount of carbon nanotubes together with low quantity of total carbon).

2.2.2.4. Bi-trimetallic catalysts. Developing bi/trimetallic catalysts is a practical and crucial method to develop highly coke-resistant Ni-based catalysts for DRM and there has been significant research activity in this direction in recent years. Combining nickel with other metals can readily change its surface properties to implement better catalytic activity; a phenomenon that is also termed the synergistic influence.[101] Based on a study by Elsayed et al.[102], supported bimetallic catalysts demonstrate high activity and stable DRM reaction performances. In an experiment to test the stability, platinum (0.2–2 wt.%) and/or nickel (8 wt.%) and magnesium (8 wt.%) immobilized onto a ceria-zirconia support. Ceria-zirconia (0.6:0.4) solid solutions were synthesized by precipitation and the metals were loaded by the incipient wetness method. It can be observed that The combination of Pt with NiMg/(Ce,Zr)O_2 catalysts augment the low temperature dry reforming activity compared to the control catalysts without Ni and Mg and Pt. One of the major key factors responsible for the excellent catalytic performance of this bi/trimetallic catalyst is the high dispersion and synergistic effects between the platinum and oxide phases, which is correlated to the reduction temperature and the number of basic sites. In general, the formation of carbon is efficiently hindered by the formation of PtNiMg/(Ce,Zr)O_2 over the course of the 100.5 h on stream compared to the single Ni sites.

Herein, the promotional effects of Fe, Mg, and Pt on Ni-based catalyst supported on Al_2O_3-CeO_2 (Ni/Al_2O_3-CeO_2) have been investigated in DRM reaction. To illustrate the influence of metal promoters on the catalytic activity of Ni/Al_2O_3-CeO_2 materials, the catalytic reaction was conducted in a continuous fixed-bed flow reactor in temperature

range of (550-700 °C), space velocity of 12,000 $ml g_{cat}^{-1} h^{-1}$ and different feedstocks (pure CH_4 or 50% CH_4/CO_2 mixture) under atmospheric pressure for 10 h time-on-stream. The combination of material characterization and catalytic test revealed that Fe and Mo-doped Ni/Al_2O_3-CeO_2 are excellent catalysts for this process by helping to achieve around 78% CH_4 conversions and 81 % CO_2 conversions, respectively and selectivity to syngas (~90%) and stability of the obtained $FeMo/Ni/Al_2O_3$-CeO_2 composite catalyst. Meanwhile, obtained results implied that the incorporation of 0.005 wt% Pt to the $FeMo/Ni/Al_2O_3$-CeO_2 composite catalyst leads to a highly reactivity at 700 °C by helping to achieve around 81% CH_4 conversions and 86 % CO_2 conversions, respectively during DRM reaction as depicted in paper II.

The performance and stability of Al_2O_3-CeO_2 supported Fe/, Pt/Fe/, MgFe/, Pt/MgFe/ -doped Ni catalysts have been tested towards DRM reaction. The catalysts were synthesized using impregnation with various loadings of Ni, Fe, Mg, and Pt and they were characterized using BET, XRD, H_2-TPR, CO_2-TPD, and FTIR-Pyridine techniques. The reforming of methane with carbon dioxide has been investigated on Ni-based catalyst supported on Al_2O_3-CeO_2 in a fixed-bed continuous-flow reactor. The catalytic reaction was conducted at various reaction temepratures (550-700 °C), space velocity of 12,000 $ml g_{cat}^{-1} h^{-1}$ and different feedstocks (pure CH_4 or 50% CH_4/CO_2 mixture) under atmospheric pressure for 10 h time-on-stream. The co-doped Ni/Al_2O_3-CeO_2 catalysts with Fe and Mg significantly enhanced the catalyst performance (higher than 83% methane and 84% CO_2 conversion). Moreover, our results found that the incorporation of 0.005 wt% Pt to the MO_xNi/Al_2O_3-CeO_2 (MO_x = Mg, and Fe) composite catalysts lead to high catalytic activity as well as the results revealed the the impact of secondary and tertiary metal doping on Ni-

based Al_2O_3-CeO_2 catalyst and the highest methane (>85%) and CO_2 (~90%) conversions and high selectivity towards H_2/CO ratio (0.97) were obtained over Pt/MgFe/Ni/Al_2O_3-CeO_2 composite catalyst and illustrated very stable reactivity with very low carbon formation as depicted in Paper III.

2.2.3. Oxidative Dehydrogenation of Propane with CO_2. Remarkably, demand for short-chain alkenes, essentially ethene and propene. It is determined that production of these building-blocks chemical will exceed 300 M tonne during 2020. In the case of propene[103], is a significant chemical feedstocks for the manufacturing industry such as polymer and rubber manufacture. Based on above, there are major wo type of commercial processes (steam cracking of naphtha or liquid petroleum gas, LPG, and fluid catalytic cracking, FCC, of heavier oil fractions) have already reached their optima for propene production.[104] Thus, there has been deceived investigation of substitutional routes with less consumption of energy, like transformation of alkanes towards alkenes besides, other new processes. The non-oxidative catalytic dehydrogenation of propane (CDP) has received attention recently, which carried out at high temperatures (above 527 ^oC) in order to circumvent thermodynamic restrictions, with consequent catalyst deactivation due to propane/propene cracking and carbon formation, thus it is found propene selectivity and yield were declined.[105] The oxidative dehydrogenation of propane (ODP) is attractive because the reaction is exothermic, and it can proceed at lower temperatures, suppressing coke formation. However, the main drawback represents loss of propene selectivity because of the overoxidation of propane to carbon dioxide in the reaction. Handling the potentially explosive oxygen-containing mixture is also difficult. This drastic decline in the olefins yield, due to the low concentrations of propane employed. In order to overcome

these obstacles and enhance the selectivity and yield process, carbon dioxide has been suggested as a mild oxidant instead of oxygen.[106] The hydrogen could be removed propane dehydrogenation and shifts the dehydrogenation equilibrium towards the propene formation and augments propene yield, can be received using higher propane concentrations in the process and/or coke gasification using CO_2. Oxidative dehydrogenation (ODH) of hydrocarbons has been extensively studied over supported vanadia catalysts. Support plays an important role in heterogeneous catalytic reactions. It promotes the reactions not only by enhancing the surface area and thereby increasing the metal dispersion but also by interacting with the active metal. The silica, alumina and titania. are the most commonly used as supports. Recently zirconia, usually used as a ceramic material, is also attracting attention. It can be used either as a support[107] or as an active material.[108] The important properties of addition zirconia over the conventional supports has strong interaction with the active metal phase resulting in excellent dispersion and higher thermal and chemical stability. It is reported to be stable even under reducing conditions.[109] Zirconia is the only metal oxide possessing all the four chemical properties important for catalysis: acidity, basicity, reducing ability and oxidizing ability. These unique features of zirconia make it suitable as catalytic material for many reactions. Currently, it is widely utilized either as a single support or mixed support for vanadia catalysts in various reactions. Furthermore, Cr-based catalysts have been widely utilized for the oxidative dehydrogenation of alkanes[110], which uses an RWGS process to suppress the hydrogen generated from alkanes with CO_2 to produce CO. Additionally, carbon formation can also be mitigated by carbon reduction with CO_2. We reported the compared to Ga/H-zsm-5, the as-prepared Cr/, and V/ doped H-ZSM-5 catalysts mixed oxide

catalysts reveal dramatically enhanced activity for propane dehydrogenation. Our results show that the highest catalytic performance can be attained at a Cr/V-Ga/H-ZSM-5 catalyst which allows the steady formation of a maximum propane conversion and propene selectivity of 67 and 56% , respectively in the catalytic dehydrogenation of propane at 550 ^{o}C.

PAPER

I. POLYMERIC HOLLOW FIBERS AS BIFUNCTIONAL CATALYSTS FOR CO_2 CONVERSION TO CYCLIC CARBONATES

Abbas Jawad, Fateme Rezaei, Ali A. Rownaghi*

Department of Chemical & Biochemical Engineering, Missouri University of Science and Technology, 1101 N. State Street, Rolla, Missouri 65409, United States

ABSTRACT

In this study, development of cooperative catalyst is demonstrated whereby Lewis acid/base species and nucleophilic parts are immobilized in the pores of a polyamide-imide (PAI) hollow fiber support. The highly solvent-stable and porous Br/APS-grafted ZrO_2-PAI hollow fiber (Br/APS/Zr-PAIHF) catalyst was created by crosslinking of bare ZrO_2-PAIHF polymer with 3-aminopropyltrimethoxysilane (APS) followed by alkylation with 1,2-dibromoethane at 110 °C. This bifunctional catalyst consists of a porous ZrO_2-PAIHF polymer crosslinked with APS that was further immobilized with nucleophilic bromide ions. Porous ZrO_2-PAIHF provides a physical barrier to prevent cooperative Lewis acid/base species and nucleophilic parts movement, aggregation, and detachment from the support into the product stream. The performance of Br/APS/Zr-PAIHFs as heterogeneous catalyst was investigated for the reaction of carbon dioxide (CO_2) with styrene oxide (SO) which leads to the formation of styrene carbonate (SC). The influence of various reaction parameters including reaction temperature, reaction time, solvents, and CO_2 pressure were systematically investigated in detail. Our results indicated that the synergistic cooperative

effect of nucleophilic bromide ion (Br^-) and Lewis acid/base species on PAIHF supports leads to a maximum SC selectivity of 99.1%. Additionally, SO conversion of 100% and excellent SC selectivity of 98% were obtained over Br/APS/Zr-PAI-HF catalyst.

Keywords: Porous ZrO_2-PAI hollow fiber polymer; immobilizing acid/base and nucleophilic species; cooperative heterogeneous catalyst; CO_2 cycloaddition.

1. INTRODUCTION

The utilization of CO_2 as a renewable feedstock for producing commodity chemicals and fuels is an interesting challenge to explore new concepts and opportunities in catalysis and industrial chemistry. [1–8] This sustainable approach not only leads to production of useful chemicals, but also has the potential to mitigate antropogenic CO_2 emissions to the atomosphere.[9–12] CO_2 itself is a sustainable and inexhaustibly available carbon source, however, it is inextricably linked to its inherent inertness.[9,10,13–15] It is a thermodynamically stable molecule (ΔG_f = -394.01 kJ.mol^{-1}) with high oxidation state, hence, reactions of CO_2 must be combined with a high-energy reactant to gain a thermodynamic driving force. [16–18] It has been shown that catalytic reaction is the best strategy to address this challenge.[19,20]

Although several processes for production of urea [21], methanol [22], and salicylic acid [23] have been developed through CO_2 utilization, many of them rely on extremes of temperature and pressure to work. In this context, reacting CO_2 with relatively high free energy compounds such as epoxides, hydrogen, or amines should be an alternative approach to overcome this limitation.[24] Among these alternatives, the reaction of CO_2

with epoxides, which can lead to the formation of cyclic carbonate and/or polycarbonate products, is an important chemical reaction, making use of CO_2 as a renewable feedstock. Such cyclic carbonate synthesis from CO_2 and epoxide is an important subject in catalytic chemistry.[25,26] Cyclic carbonates have wide applications in the pharmaceutical and fine chemical industries, and also play a vital role as an intermediate for the synthesis of fuel additives.

Although the copolymerization of CO_2 with epoxides over homogeneous catalysts has been known since 1969 and huge steps in homogeneous catalysis have been made over the last years [27–30], the separation of catalyst from the reactants and products is a significant challenge which typically requires more energy input and results in the decomposition of the homogeneous catalysts. In addition to homogeneous catalysts, a number of heterogeneous catalysts such as metal oxides (*e.g.*, MgO, FeO, CaO, ZnO, Zr_2O,La_2O_3, CeO_2, and Al_2O_3) [31,32] porous organic polymers (POPs) [33,34], metal organic frameworks (MOFs) [35,36], polymeric/supported ionic liquids [37,38], and cooperative catalysts [24,39–41] have been developed to catalyze the copolymerization of CO_2 with epoxides for the synthesis of cyclic carbonates. A number of researchers have studied the immobilization of homogeneous catalysts such as amines, ammonium salts, imidazolium salts, and phosphonium salts onto a solid support for the cyclic carbonate synthesis.[42,43] The immobilization of homogeneous catalysts onto solid materials facilitates the separation of catalyst from the products and improves its usability in the continuous flow reaction applications. Cooperative catalysts combining weak acids (OH group) and basic (NH_2 group) functionalities, and nucleophilic parts are effective active sites for enhancing copolymerization of CO_2 with epoxides mainly because they can

promote concerted electron-proton transfers. Numerous studies on mesoporous silica supports have established amine-nucleophilic group (*e.g.*, Br^-, I^-) interactions as the most useful bifunctional catalysts for the cooperatively catalyzing CO_2 cycloaddition.[44,45] Jadhav *et al.*[46] investigated the effect of various anions such as Cl^-, Br^-, BF_4^-, PF_6^-, and NTf_2^- on polymer-supported ionic liquids (PSILs). It was shown that PSIL-NTf_2 was the most efficient catalyst exhibiting 100% conversion and 91% yield of the respective cyclic carbonate under 100 ^oC reaction temperature and 8 bar pressure in 8 h reaction time. Repo and co-workers [47] synthesized bifunctional Schiff base iron (III) complex and evaluated as an intramolecular catalyst for cyclic carbonates synthesis from CO_2 and epoxides. It was found that Lewis acidic iron center and Lewis basic imidazoles can activate the coupling reaction of propylene oxide (PO) and CO_2 without an additional co-catalyst eventhough the iron compound acts as a monomolecular catalyst. In another study, the cooperative action of Mg^{II} and Br^- in bifunctional Mg (II) Porphyrin catalyst was shown to promote the cyclic carbonate formation from epoxides and CO_2.[40] Gao *et al.*[48] developed and used phosphonate-based Zr-MOF as a heterogeneous bifunctional catalyst (combined Lewis acid and Brønsted acid sites) for coupling reaction of epoxide and CO_2.

Despite significant progress in development of cooperative catalysts, most of the developed materials still suffer from low activity and stability in CO_2 cycloaddition reaction and cannot be used in continuous flow system. Moreover, a relatively simple and convenient method for permanent immobilization of various types of catalyst within porous polymers that addresses stability, reactivity, and recyclability of the produced heterogeneous materials in copolymerization of CO_2 with epoxides has not been established so far. Recently, we demonstrated the concept of cooperative organocatalysis

based on polymer hollow fiber support and its utilization for chemical transformation.[49,50] Building from the research conducted on both homogeneous and heterogeneous catalysts, we have hypothesized that porous polymeric hollow fibers can provide new design elements that are challenging to employ with homogeneous catalysts. Porous polymeric hollow fibers are pseudo monolithic materials that have great potential to make the reaction more efficient and attractive by providing a high surface area to volume ratio, increase in flow pattern reliability for scale-up, and the ability to tune mass transfer resistances. This type of porous hollow fiber is readily available and inexpensive which makes such a catalyst highly attractive in the context of green chemistry and in view of potential large-scale applications. This study aims at creating solvent-resistant porous Zr-PAI hollow fibers (Zr-PAIHFs) by crosslinking with 3-aminopropyltrimethoxysilane (APS) followed by alkylation with 1,2-dibromoethane for formation of cooperative Lewis acid/base functionality and nucleophilic parts that are suitable for application as heterogeneous catalysts in production of styrene carbonate (SC) from CO_2 and styrene oxide (SO).

2. EXPERIMENTAL SECTION

2.1. CHEMICAL

The following chemicals were used for polymer dope preparation and formation of the composite hollow fiber catalysts: zirconia with an average particle size of 100 nm (Sigma-Aldrich), Torlon PAI (polyamide-imide) 4000T-HV which is a commercially available polyamide-imide (PAI) (Solvay Advanced Polymers, Alpharetta, GA), N-

Methyl-2-pyrrolidone (NMP) (Reagent Plus, 99%, Sigma-Aldrich, Milwaukee, WI), polyvinylpyrrolidone (PVP; average Mw.1300 K, Sigma- Aldrich), N,N-dimethylformamide (DMF) (99%) (ACS Reagent, >99.8%, VWR), methanol (ACS grade, VWR), and hexane (ACS Reagent, >98.5%, VWR). In addition, 3-aminopropyltrimethoxysilane (APS) (95%), styrene oxide (SO) (97%), acetonitrile (ACN) (99.8%), dimethylformamide (DMF) (99.8%), and 1,2-dibromopropane (97%) were purchased from Sigma-Aldrich. Ultra-high pressure (UHP) N_2 and CO_2 gasses were purchased from Airgas.

2.2. BROMIDE -IMMOBILIZED Zr-PAI HOLLOW FIBER FORMATION

The polymer dope composition and ZrO_2- polyamide-imide (PAI) hollow fiber formation and aminosilane crosslinking approaches have been described in in detail Supporting Information (see Section S1 and Table S1, Supporting Information). Briefly, after formation of Zr-PAIHFs, they were crosslinked with APS and before bromide-immobilization could be achieved, the APS/Zr-PAIHFs were washed with water to remove uncrosslinked aminosilane. The APS/Zr-PAIHFs were post-synthetically modified by reaction with 1,2-dibromopropane in dry toluene at 80 ^{o}C for 4-6 h to give the ammonium bromide derivatives. Then, solvent exchange with toluene was performed to remove the excess alkyl halide and allowed to dry at room temperature in the hood overnight. Finally, the fibers were exposed to a vacuum (30 mTorr) at 85 °C to remove the residual solvent from the pores, yielding the Br-immobilized APS-grafted Zr-PAIHFs (Br/APS/Zr-PAIHFs).

2.3. BROMIDE -IMMOBILIZED Zr-PAI HOLLOW FIBER FORMATION AND REACTION PRODUCT CHARATERIZATION

A high-resolution scanning electron microscope (Hitachi S-4700 FE-SEM) was used to assess the morphology of the hollow fibers before and after post-treatment. All bare and post-treated fibers were characterized by Fourier transform infrared spectroscopy (FTIR) at room temperature over a scanning range of 400-4000 cm^{-1} with a resolution of 4.0 cm^{-1}, using Bruker Tenser spectrophotometer. Bulk elemental analysis (ICP-MS) and CHN analyses (PerkinElmer Series II, 2400) were carried out to determine ZrO_2 nanoparticles content, and amine and bromine loadings of the hollow fibers. The corresponding results are provided in Table 1. Nitrogen physisoprtion isotherms were measured using a Micromeritics 3Flex surface characterization analyzer apparatus at 77 K. The hollow fibers were degassed at 110 °C under vacuum for 2 h prior to analysis. Surface area and pore volume were calculated from the isotherm data using the Brunauer-Emmett-Teller (BET) and Barrett-Joyner-Halenda (BJH) methods, respectively. To probe the efficacy of fibers for CO_2 adsorption, gravimetric sorption capacity measurements were performed using a Q500 thermogravimetric analyzer (TA Instruments) at 1 bar using 10% CO_2 in N_2. A typical adsorption experiment consisted of pretreating the material for 3 h at 110 °C in flowing N_2 to remove pre-adsorbed CO_2 and moisture or volatile solvents from the fibers. The temperature was then decreased to 35 °C and the gas feed was switched to 10% CO_2 in N_2. The sample started to adsorb CO_2 and the experimental run was continued until the fiber weight stabilized to an apparent equilibrium (for all runs, the adsorption time was set to 2 h).

2.4. CYCLOADDITION REACTION

In a typical catalytic reaction, 30 mmol of SO, 50 mL of ACN or DMF (as a solvent), and 300 mg of activated catalyst were delivered into a high-pressure laboratory autoclave (Parr, USA) that was equipped with a magnetic stirrer and jacket heater. After being sealed, the reactor was carefully flushed three times with CO2. After flushing, 5-40 bar of CO2 was pressurized in the reactor and heated and stirred. After having reached the working temperature of 80-160 oC, the reaction was allowed to proceed for 6-10 h. After the reaction was completed, the autoclave continued to cool down at room temperature and the excess CO_2 was vented by opening the outlet valve. This decompression was carried out slowly for 30 min to minimize the loss of the reaction mixture and allow the liquid phase to degas properly. After depressurization, the autoclave was opened slowly, and the reaction mixture was separated by filtration (Whatman, diameter 55 mm). The mixture was analyzed by gas chromatography (Varian 3800) equipped with an Elite Wax capillary column (DB-5) and a flame ionization detector (FID). The reaction mixture was analyzed using mass spectrometry GC-MS (Hewlett Packard 5890E Series II Plus Gas Chromatograph) with a mass selective detector (Hewlett Packard/HP 5972 GC/MSD System).

3. RESULTS AND DISCUSSION

3.1. Br/APS/Zr-PAIHFs FORMATION AND CHARACTERIZATION

We used the PAI porous polymer as catalyst support due to its good chemical and thermal stability, excellent processability, and mechanical robustness.[51–54] The

asymmetric ZrO_2-PAIHFs (Zr-PAIHFs) were fabricated via a dry-jet/wet-quench spinning process, as illustrated in Figure S1 supporting information. The optimized PAI polymer dope compositions and fiber formation conditions are also presented in Table S1. A solution mixture of water/N-methyl-2-pyrrolidone (NMP) (50:50 wt%) was used as alternate sheath fluid to eliminate the fibers skin layer to facilitate formation of an extremely open surface on the outside of the fiber with a lacey structure, for subsequent surface modification (see Supporting information for detailed synthetic procedure). One of the key challenges faced in developing porous polymers such as polymeric/supported ionic liquids [37,55] or POP [33,34] as heterogeneous catalysts lies in ensuring their excellent stability in organic solvents, preventing active sites release, achieving acceptable reactant diffusivity (e.g. CO_2 and epoxide), and carbonate separation. To improve the Zr-PAIHFs stability in polar aprotic solvents such as DMF and ACN, the porous Zr-PAIHF substrates were exposed to APS in toluene solution at 60 °C for 2 h followed by washing with hexane to remove un-crosslinked APS molecules and finally crosslinking under vacuum at 60 °C for 2 h (see Supporting information for detailed crosslinking procedure). As shown in Scheme 1, hydrolysis and condensation reactions between APS molecules follow Si-O-Si linkages formation occurred by nucleophilic attack of the oxygen contained in water which is facilitated in the presence of homogenizing agents such as toluene.[51–53,56] The Zr-PAIHFs were crosslinked by forming amine-tethered networks and siloxane-bonded oligomers within the substrates. The resultant APS-grafted PAIHFs were solvent-stable and showed higher hydrophilicity and good mechanical stability.

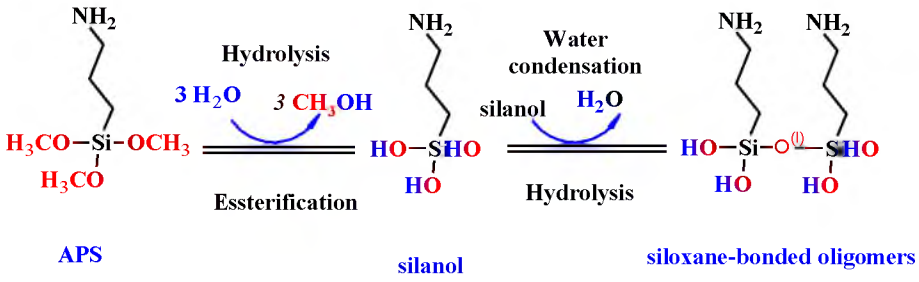

Scheme 1. Hydrolysis and condensation of APS molecules and formation of siloxane-bonded oligomers within porous Zr-PAIHFs.

The textural properties of bare Zr-PAIHFs, ASP/Zr-PAIHFs, and Br/APS/Zr-PAIHFs were characterized by N_2 physorption and the corresponding results are shown in Table 1.The BET surface area and pore volume of Br/APS/Zr-PAIHFs decreased by approximately 50% after post-treatment processes which could be due to successful APS crosslinking and bromide-immobilization into Zr-PAIHFs. This could be related to amine grafting and filling of the smaller pores in the fiber substructure (fiber shell) and also on the fiber surface during the grafting process. As shown in Figure S2 supporting information, the N_2 physisorption isotherms of all fibers are type-IV isotherms with H_1 type hysteresis, indicating a typical mesoporous structure according to IUPAC classification.[57] Moreover, the textural properties of Br/APS/Zr-PAIHFs were very similar before and after CO_2-epoxide cycloaddition reaction. In this study, one of the key techniques is to immobilize both aminosilane and nucleophile species into the highly interconnected pore cell walls (typically, less than 1 μm of thickness) within the fibers for an effective CO_2 adsorption system. The CO_2 adsorption capacity of the fibers were measured at 35 °C in 10% CO_2 concentration (balanced with N_2) using TGA, and the corresponding experimental results are shown in the Table 1. It was observed that the CO_2

capacity uptake increases with APS-grafting and bromide-immobilizing. The obtained capacity values at 35 °C were determined to be 0.02, 1.30, 1.40 and 1.38 $mmol.g^{-1}_{fiber}$ over bare Zr/PAIHFs, APS/Zr-PAIHFs, Br/APS/Zr-PAIHFs (before reaction) and Br/APS/Zr-PAIHFs (after reaction), respectively. The fact that CO_2 capacity was retained after reaction indicates the stability of functional groups during the reaction.

The ICP-MS analyses were employed to obtain the ZrO_2, nitrogen (amine), and bromine loadings in the fiber bulk before and after *postmodification* and *reaction*. As shown in Table 1, no noticeable difference was observed in ZrO_2 and nitrogen contents before and after reaction, implying that the chemical state of fibers remained unchanged after reaction. However, the amount of bromide in the Br/APS/Zr-PAIHF was found to decrease slightly after reaction. These results demonstrate that negligible fraction (~0.5%) of immobilized bromide ions leached from the fibers to the product stream.

Table 1. Textural properties, CO_2 capacity, and ZrO_2, amine, and bromide loading of the bare Zr-PAIHFs and postmodified Br/APS/Zr-PAIHF, before and after reaction.

Materials	S_{BET}[a]	V_{Pore}[b]	CO_2 capacity[c]	ZrO_2 loading[d]	N loading[d]	Br loading[d]
	$[m^2.g^{-1}]$	$[cm^3.g^{-1}]$	$[mmol.g^{-1}_{fiber}]$	[wt%]	$[mmol.g^{-1}_{fiber}]$	$[mmol.g^{-1}_{fiber}]$
Bare Zr-PAIHF	56	0.26	0.02	10.0	-	-
APS/Zr-PAIHF	21	0.15	1.30	9.6	4.02	-
Br/APS/Zr-PAIHF (before reaction)	14	0.08	1.40	9.6	3.46	0.100
Br/APS/Zr-PAIHF (after three runs)	12	0.07	1.38	9.5	3.33	0.095

[a]Determined by nitrogen physisorption experiments at 77 K.

[b]Determined by BJH method.

[c]Measured by TGA at 35 °C.

[d]Determined by elemental analysis.

Figure 1a-b shows SEM images of the cross-section and surface of bare Zr-PAIHFs. The SEM images of the surface of APS-grafted and Br-immobilized Zr-PAIHFs are shown in Figure 1c-d. The post-treatment of fibers may swell the polymer chains, thereby resulting in a smaller pore size towards the surface. The pore cells were found to be generally smaller for Br/APS/Zr-PAIHFs (Figure 1d) than for APS/Zr-PAIHFs (Figure 1c), which resulted in a smaller surface area and pore volume. Moreover, the longer post-treatment time and higher concentration of either APS and 1,2-dibromoethane solutions adversely affected the surface area and porosity. With this in mind, both concentration and post-treatment time parameters were adjusted to improve both CO_2 adsorption and conversion over Br/APS/Zr-PAIHFs. In addition, as can be clearly seen from Figure 1e, the fiber surface displayed moderate porosity after reaction in ACN solvent, confirming a strong bonding between the nucleophile and the polymer matrix as well as swelling resistance of APS-grafted PAI hollow fibers. These micrographs qualitatively confirm that the fiber outer pore morphology collapsed during posttreatment processing, in agreement with the fibers textural properties, as discussed earlier.

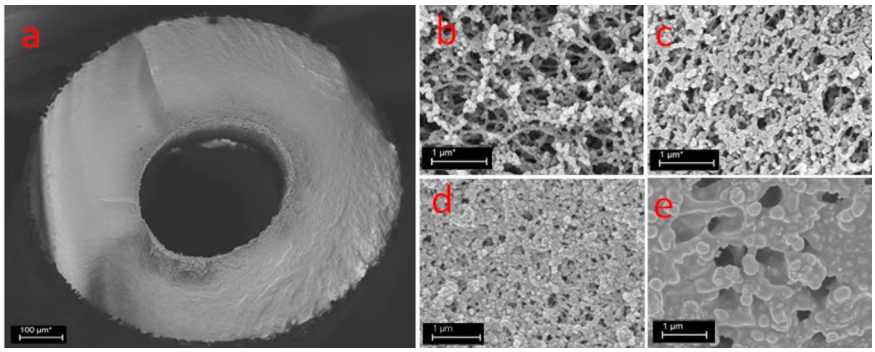

Figure 1. SEM images of (a) the cross section of bare Zr/PAIHF; (b) surface of bare Zr-PAIHF; (c) surface of APS/Zr-PAIHF; (d) surface of Br/APS/Zr-PAIHF (before reaction); and (e) surface of Br/APS/Zr-PAIHF (after reaction).

To further confirm the chemical bonding of aminosilane and bromine ions with the imine functional groups on PAI hollow fibers surface, the FTIR analysis was carried out over fresh and used Br/APS/Zr-PAIHF catalyst. The FTIR spectrua of bare Zr-PAIHF, APS/Zr-PAIHF and Br/APS/Zr-PAIHF are shown in Figure S3, Supporting Information. The functionalized fibers showed a broad vibration band in the range of 3000-3500 cm^{-1} which is attributed to the O-H of hydrogen bonds in SiO-H, while the N-H vibration band was appeared at 3468-3416 cm^{-1}.[53] The bands around 954 cm^{-1} and 1093 cm^{-1} correspond to the symmetric stretching vibration of Si-OH and the vibration frequency of the Si-O-Si bond asymmetric stretching, respectively.[51,53] Further, the band at around 503 cm^{-1} resulted from the existence of both tetragonal and monoclinic zirconia, whereas, the Zr–O bond gave rise to a peak at 730 cm^{-1}.[51] The band at 1619 cm^{-1} has been reported in the literature[44] and is attributed to conjugated C=N vibration of the cyclic system (imidazole).[51,52] The vibration band at 597 cm^{-1} demonstrated the fuctionalization of APS/Zr-PAIHF with 1,2-dibromoethane. The FTIR spectrum of the Br/APS/Zr-PAIHF confirmed the successful APS-grafting and Br-immobilization on the surface of bare Zr-PAIHF.

As Figure S3 illustrates, the FTIR spectra displayed distinct changes in the bare PAI hollow fiber chemical structure after APS-grafting and Br-immobilizing treatments. These results indicate that the original imide rings in PAI-HFs were opened during APS functionalization reaction, as it was confirmed in our previous studies.[51,53]

Having established a viable method to create highly stable APS-grafted Zr-PAIHFs, the fibers were exposed to 1,2-diboromoethane solution for alkylation and permanent immobilization of bromide as a nucleophile part. On the basis of these results,

the proposed schematic of APS grafting and bromide alkylation of Zr-PAIHFs is depicted in Scheme 2.

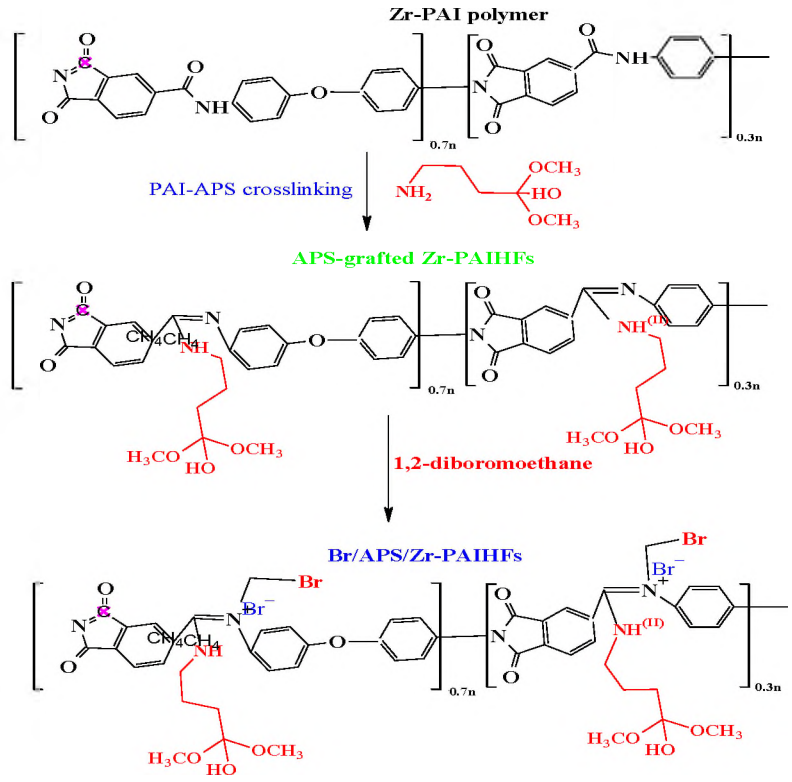

Scheme 2. Schematic representation of Zr-PAIHFs crosslinking followed by alkylation of APS-grafted PAI hollow fibers with 1,2-dibromoethane in dry toluene.

3.2. CO_2 CYCLOADDITION REACTION OVER Br/APS/Zr-PAI-HF CATALYST

The degree of epoxide conversion and the cyclic carbonate selectivity of the CO_2 cycloaddition to epoxide are greatly influenced by the nature of catalytic system, reaction conditions, and nature of the epoxide. Pressure is one of the most crucial parameters affecting the CO_2 cycloaddition reaction since CO_2 can act as both reactant and solvent under different pressure and its diffusion can affect the reaction kinetics.[44] The optimum

pressure condition was determined by testing 300 mg Br/APS/Zr-PAIHF catalyst at various pressures (*e.g.*, 5, 10, 20, 40 bar) at 160 °C for 8 h. The CO_2 pressure was varied to determine the pressure that gives rise the highest SC yield. The liquid phase products were analyzed by GC-MS and GC-FID, which allowed for identification and quantification of all main components. The corresponding SC yields at various CO_2 pressures are presented in Figure 2. Clearly, lower SC yield was obtained for Br/APS/Zr-PAIHF catalyst tested at both lower and higher pressures than 20 bar. The epoxide becomes increasingly soluble in the compressed and supercritical CO_2, thus, the Br/APS/Zr-PAIHF catalyst exhibited SC yield of 100% at 20 bar and 160 °C for 8 h. Consistent with earlier works,[44,58] the extremely high CO_2 pressure reduced SC yield due to lower SO concentration in the liquid phase, because CO_2 is considered as a dense gas and acts as an solvent for the system. Two by-products namely, benzaldehyde (BA) and phenylacetaldehyde (PA) were obtained at 40 bar CO_2 pressure. The same behavior was reported over different heterogeneous and bifunctional catalysts at higher CO_2 pressure.[59,60] A pressure of 20 bar, a reaction temperature of 160 °C, and reaction duration of 8 h yielded the optimum condition for CO_2 conversion and selectivity to SC. It should be mentioned here that in order to gain insight into the potential bromine leaching from the Br/APS/Zr-PAIHF catalyst, we performed catalytic runs using recycled catalyst (dried in vacuum oven for 2 h at 80 °C) under selected reaction conditions, as stated above. Very similar SO conversion and selectivity to SC were observed after two runs over recycled Br/APS/Zr-PAIHF catalysts, suggesting that bromine did not leach significantly under these reaction conditions, in accordance with the results of ICP analysis (Table 1).

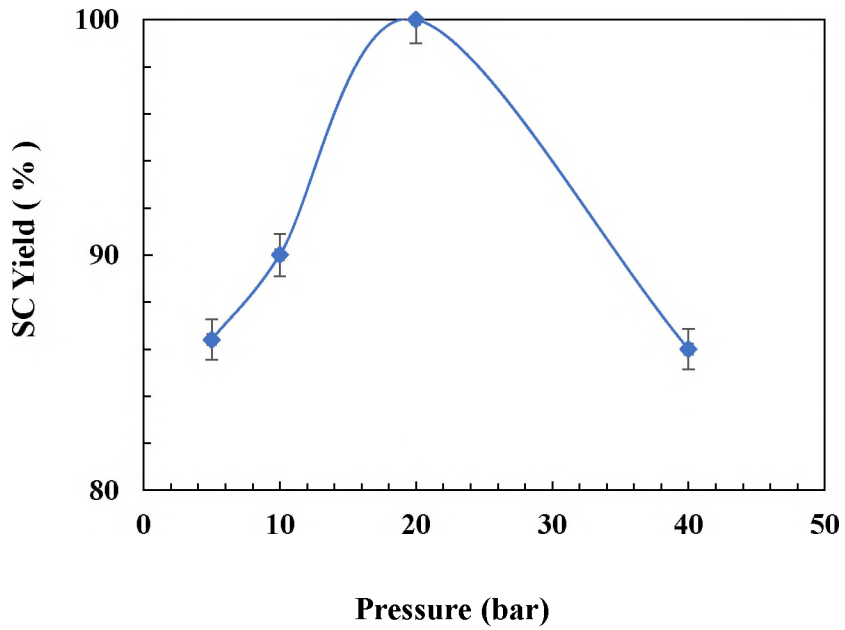

Figure 2. Effect of CO_2 pressure on SC yield. Reaction conditions: catalyst mass = 0.3 g; reaction temperature = 160 ^oC; reaction time = 8 h.

Notably, the control reactions performed with the bare Zr-PAIHFs (i.e., no amines grafted) and APS/Zr-PAIHFs led to no observable CO_2 cycloaddition. One interesting observation made from our control experiments was that the aminosliane grafting of Zr-PAIHFs was crucial for preventing fibers swelling since bare Zr-PAIHFs were dissolved in DMF and ACN solvents during the reaction. However, such enhancement in the fiber stability did not improve its activity for CO_2 cycloaddition. Srivastava *et al.* [41,62] used various aliphatic and aromatic amines-immobilized SBA-15 and Ti(Al)-SBA-15 as bifunctional catalysts for CO_2 cycloaddition and the carbamate synthesis. The synergistic effects of the coexistence of Ti sites (Lewis acid), hydroxyl group (weak Brønsted acid), and amine group (base site) were observed for the CO_2 cycloaddition reaction. Thus, the synergistic effects of the immobilization on inorganic materials having surface hydroxyl groups are common. The surprising enhancement of the activity by immobilizing Br^- on

APS/Zr-PAIHFs was ascribed to the cooperative activation of the epoxide ring by Lewis acidic Zr center and basic bromide anion and NH_2 Lewis basic sites which can polarize the CO_2 molecule to facilitate CO_2 insertion. This also supports the cooperative activation mechanism shown in Scheme 2. The enhancement of the activity by the immobilization was also observed with Lewis/Bronsted acid species and imidazolium halides, as a cooperative system.[63] Babu *et al.* [63] applied this strategy for synthesizing Zn-MOF-NH_2 and confirmed the cooperative acid-base characteristics in the cycloaddition reaction of CO_2 with propylene oxide. Miralda *et al.*[64] tested bare and amine-functionalized ZIF-8 and observed that both yield and selectivity to the carbonate improved with amine; however, the catalytic properties of both catalysts were unstable. Moreover, Pescarmona *et al.* [65] reported that the addition of a Lewis base co-catalyst improves atom-efficient reaction of CO_2 with different epoxides by employing iron pyridylamino-bis(phenolate) and MIL-100(Cr) bifunctional catalysts.

Table 2. Influence of reaction temperature on the cycloaddition reaction of CO_2 with SO.

Catalysts	Reaction Temperature (^oC)	SO Conversion (%)	Selectivity (%)		
			SC	PA	BA
.Bare Zr-PAIHF	80	-	-	-	-
APS/Zr-PAIHF	80	-	-	-	-
Br/APS/Zr-PAIHF	80	93	26	15	59
	120	98	99	1	-
	160	100	98	2	-

Reaction conditions: catalyst =300 mg; styrene oxide = 3.5 mL; acetonitrile (solvent) = 50 mL; CO_2 pressure = 20 bar; reaction time = 8 h.

The formation of SC was also confirmed by ^{1}H NMR. Furthermore, the influence of reaction temperature on SO conversion was investigated by varying the temperature from 80 to 160 °C. As shown in Table 2, the SO conversion and SC selectivity were both enhanced by increasing the reaction temperature. The CO_2 epoxidation of SO gave rise to a product mixture of SC, PA, and BA. Almost 100% selectivity toward SC was obtained at higher reaction temperatures (i.e., 160 °C). This observation is consistent with published reports using heterogeneous systems.[39,44,61] The superior catalytic performance of Br/APS/Zr-PAIHF could be attributed to the combination of excellent CO_2 sorption ability and the cooperation catalytic activity between acid-base bifunctional sites and bromide ions (Scheme 2).

The effect of polar aprotic solvents (i.e., ACN and DMF) on SO conversion and SC selectivity was also evaluated in this study. Table 3 shows the effect of reaction time on the SC selectivity over Br/APS/Zr-PAIHF in ACN and DMF solvents. As shown in Table 3, longer reaction times resulted in dramatic decrease in chemo-selectivity of the process with higher amounts of BA and phenylacetaldehyde (PA) being formed. This agrees with previous observation, [66–68] which confirmed that the BA can be formed upon oxidative cleavage (which should arise from diol precursors that can originate from water-induced ring opening of an epoxide or carbonate hydrolysis), while PA is produced from Meinwald rearrangement. Notably, both SO conversion and SC selectivity in ACN solvent were higher than in DMF at various reaction times (ranging from 6 to 10 h), which could be due to the high polarity of ACN that helps CO_2 to dissolve, activate, and produce corresponding cyclic carbonate. Although ACN was used as the reaction solvent, it can act as a

dehydrating agent to absorb the water formed during the reaction and enhance the yield of SC.[69]

Table 3. Influence of reaction time on the cycloaddition reaction of CO_2 with SO over Br/APS/Zr-PAIHF in ACN and DMF solvents.

Solvents	Reaction time (h)	Conversion (%)	Selectivity (%)		
			SC	BA	PA
ACN	6	100	100	-	-
	8	100	98	-	2
	10	81	97	-	3
DMF	6	100	98	2	-
	8	98	87	-	13
	10	90	59	-	41

Reaction conditions: 30 mmol of SO; 50 mL of ACN or DMF; catalyst = 300 mg; CO_2 pressure = 20 bar; reaction temperature = 160 °C.

Previous studies have shown that the combination of Lewis/Bronsted acid species and a nucleophile can induce activation of epoxides for ring opening and polarize CO_2 molecule to facilitate CO_2-epoxide cycloaddition.[63,70] The Lewis acid (ZrO_2) has the role of activating the epoxide towards ring opening by the bromide, followed by the insertion of CO_2 into the activated intermediate. In Br/APS/Zr-PAIHFs, the O^- ion of SO interacts with Zr Lewis acid sites followed by attacking the Br^- of ammonium salt (PAI backbone structure) to the least hindered carbon atom, resulting in the epoxide ring opening (a, in Scheme 3). Subsequently, CO_2 is polarized by primary amine groups of APS-grafted

Zr-PAIHFs. This interaction is facilitated further by the possibilities of rotating the $–NH_2$ groups present in the crosslinked APS/Zr-PAIHFs structure. This disorder has been confirmed by our control experiment (Table 2) and also by using single crystal X-ray diffraction of UMCM-1-NH_2 by other researchers.[71] The obtained carbonate intermediate (b, in Scheme 3) can undergo a ring-closure reaction leading to formation of the cyclic carbonate. Therefore, in the succeeding step, the O^- ion of the polarized CO_2 molecule attacks the β-carbon of the opened ring in epoxide, forming an intermediate with the elimination of Br^- (c, in Scheme 3). In the next step, the carbamate anion attacks the $–CH_2–$ and the bromide anion is liberated from SO for further reaction. Finally, the ring closure takes place to generate SC and the regenerated Br/APS/Zr-PAIHFs moves to the next cycle of cycloaddition by coordinating the next epoxide molecule. The Zr-PAIHFs offer high surface area and uniform and open porous framework structure for this reaction, thus rendering them as suitable materials for catalytic applications. The co-presence of the Lewis acidic Zr center and the N basic moieties in APS-grafted Zr-PAIHFs would make Br/APS/Zr-PAIHFs a promising candidate for the CO_2 cycloaddition reaction. As a consequence, the oxygen anion from SO attacks the carbamate carbon, which turns into the corresponding cyclic carbonate as demonstrated through cycloaddition with regeneration of the catalyst. From the plausible proposed mechanism shown in Scheme 3, the presence of bromide anion and tertiary amine has positive synergistic effect that promotes the performance of the catalyst. This finding and mechanism is in agreement with previous works showing synergistic effect of amine and bromide ion in the catalyst for high conversion and selectivity towards styrene carbonate.[24,44]

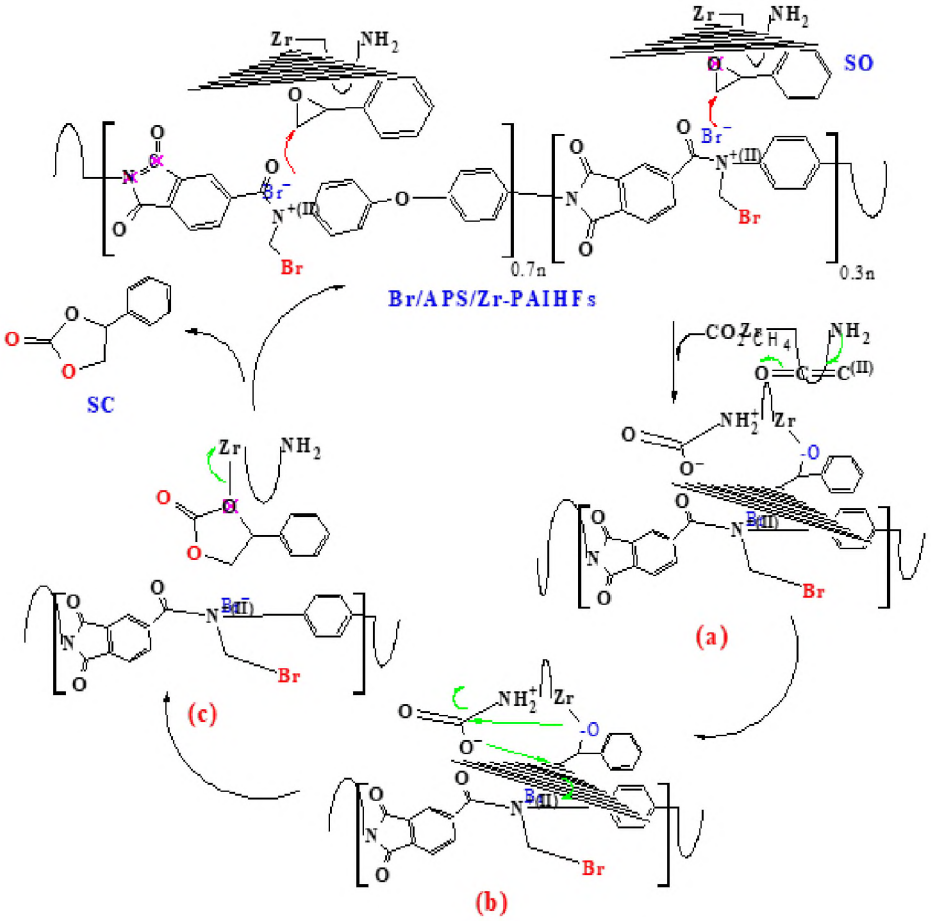

Scheme 3. The proposed reaction mechanism for cycloaddition of epoxide and CO_2 catalyzed by Br/APS/Zr-PAIHFs catalyst.

3.3. SWELLING PROPERTIES OF Br/APS/Zr-PAI-HF CATALYST

To evaluate the swelling properties of hollow fibers, the length of bare Zr/PAIHF, APS/Zr-PAIHF and Br/APS/Zr-PAIHF were measured before and after immersion in ACN solvent. The bare Zr-PAIHFs showed 6% increase in length after immersion for 5 h and no noticeable change was observed after that. In contrast, the APS/Zr-PAIHF and Br/APS/Zr-PAIHF showed improved swelling resistance such that the length of fibers increased only 2-3% and ~1% after immersion, respectively. These results indicate that some swelling

effects were still present in Br/APS/Zr-PAIHF although the degree of swelling was significantly reduced compared to the bare Zr-PAIHFs. Crosslinking of PAI hollow fibers resulted in the formation of amine-tethered inorganic networks in the fiber structure, thus leading to improved stability and hydrophobicity of the fibers in aggressive solvents.

4. CONCLUSION

This work is a proof-of-concept study demonstrating that bromine ions can be immobilized permanently on microstructured APS/Zr-PAI hollow fibers for utilization as bifunctional catalysts for the transformation of CO_2 to valuable chemicals. The anchoring of catalytically active Br^- ions within porous Zr-PAIHFs offered powerful catalytic system that enhanced the performance of bifunctional catalyst without significant ZrO_2, amine, or bromine leaching. Successful fabrication of the Br/APS/Zr-PAIHF catalyst was accomplished with a range of microstructural properties composed of a large number of interconnected cells or channels and high surface/volume ratios, which provide excellent mass transfer properties and low resistance to flow (and therefore low pressure drop) during flow reaction. Under reaction conditions investigated, a 100% SO conversion and 98% SC selectivity were obtained. Furthermore, our results indicated that a 100% improvement in catalyst activity could be realized after functionalization with APS and immobilization with Br ions. In addition, characterization of fibers after the reaction confirmed that the Br/APS/Zr-PAIHFs retained their chemical and physical structure and less degree of Br leaching was obtained. Such novel bifunctional catalyst can serve as a basis extending the use of hollow fibers as a support for other catalysts such as MOFs and as microfluidic

reactors for continuous-flow reaction at mild conditions. This experimental study provides a unifying basis for implementing a novel environmentally friendly method for production of styrene carbonate from CO_2 and SO under various reaction conditions with the purpose of achieving high activity and improved reusability.

ACKNOWLEDGMENTS

The authors would like to thank the University of Missouri Research Board (UMRB) for supporting this work. The authors also acknowledge Professor William J. Koros from the School of Chemical and Biomolecular Engineering at the Georgia Institute of Technology for giving access to his fiber spinning facilities. Professor Shubhender Kapila is also acknowledged for giving us access to his lab facilities.

REFERENCES

[1] S. Saeidi, N.A.S. Amin, M.R. Rahimpour, J. CO2 Util. 5 (2014) 66–81.

[2] G. Centi, M. de Falco, G. Iaquaniello, S. Perathoner, CO2: A Valuable Source of Carbon, Springer London, London, 2013.

[3] J. Langanke, A. Wolf, J. Hofmann, K. Böhm, M.A. Subhani, T.E. Müller, W. Leitner, C. Gürtler, Green Chem. 16 (2014) 1865.

[4] Y. Qin, X. Sheng, S. Liu, G. Ren, X. Wang, F. Wang, J. CO2 Util. 11 (2014) 3–9.

[5] B. Hu, C. Guild, S.L. Suib, J. CO2 Util. 1 (2013) 18–27.

[6] A. Al-Mamoori, A. Krishnamurthy, A.A. Rownaghi, F. Rezaei, Energy Technol. 5 (2017) 1–17.

[7] F. Rezaei, A. A. Rownaghi, S. Monjezi, R.P. Lively, C.W. Jones, Energy & Fuels 29 (2015) 5467–5486.

[8] K. Sun, Z. Fan, J. Ye, J. Yan, Q. Ge, Y. Li, W. He, W. Yang, C.J. Liu, J. CO2 Util. 12 (2015) 1–6.

[9] M. A. Atanga, F. Rezaei, M. Fitch, A. A. Rownaghi, Applied Catalysis B: Env.

(2017) doi.org/10.1016/j.apcatb.2017.08.052.

[11] Y. Liu, M. Wang, W.-M. Ren, K.-K. He, Y.-C. Xu, J. Liu, X.-B. Lu, Macromolecules 47 (2014) 1269–1276.

[12] B.J. Knurr, J.M. Weber, J. Am. Chem. Soc. 134 (2012) 18804–8.

[13] M. Aresta, A. Dibenedetto, A. Angelini, J. CO2 Util. 3–4 (2013) 65–73.

[14] C.J. Price, B.J.E. Reich, S. a. Miller, Macromolecules 39 (2006) 2751–2756.

[15] S.A. Miller, Polym. Chem. 5 (2014) 3117.

[16] D.J. Darensbourg, F.-T. Tsai, Macromolecules 47 (2014) 3806–3813.

[17] G.W. Coates, D.R. Moore, Angew. Chem. Int. Ed. Engl. 43 (2004) 6618–39.

[18] R. Nakano, S. Ito, K. Nozaki, Nat. Chem. 6 (2014) 325–31.

[19] J. Sebastian, D. Srinivas, Appl. Catal. A Gen. 482 (2014) 300–308.

[20] H. Yang, Y. Li, K. Huang, S. Long, R. Huang, Gaofenzi Cailiao Kexue Yu Gongcheng/Polymeric Mater. Sci. Eng. 30 (2014) 24–28.

[21] Z. He, J. Tu, S. Song, J. Qiu, J. Chen, Huagong Xuebao/Journal Chem. Ind. Eng. 59 (2008) 1541–1544.

[22] C. Li, X. Yuan, K. Fujimoto, Appl. Catal. A Gen. 469 (2014) 306–311.

[23] T. Iijima, T. Yamaguchi, Appl. Catal. A Gen. 345 (2008) 12–17.

[24] M. Taherimehr, S.M. Al-Amsyar, C.J. Whiteoak, A.W. Kleij, P.P. Pescarmona, Green Chem. 15 (2013) 3083.

[25] B. Song, L. Guo, R. Zhang, X. Zhao, H. Gan, C. Chen, J. Chen, W. Zhu, Z. Hou, J. CO2 Util. 6 (2014) 62–68.

[26] S. Zhong, L. Liang, B. Liu, J. Sun, J. CO2 Util. 6 (2014) 75–79.

[27] D.J. Darensbourg, M.S. Zimmer, Macromolecules 32 (1999) 2137–2140.

[28] Y. Inoue, Y. Sasaki, H. Hashimoto, J. Chem. Soc. Chem. Commun. (1975) 718.

[29] N. Yoshioka, Y. Inoue, T. Watanabe, T. Oritate, K. Yoshikawa, Y. Sasaki, Radiat. Med. - Med. Imaging Radiat. Oncol. 14 (1996) 339–342.

[30] Y. Sasaki, Y. Inoue, H. Hashimoto, J. Chem. Soc. Chem. Commun. (1976) 605–606.

[31] B.M. Bhanage, S. Fujita, Y. Ikushima, M. Arai, Appl. Catal. A Gen. 219 (2001) 259–266.

[32] A.I. Adeleye, S. Kellici, T. Heil, D. Morgan, M. Vickers, B. Saha, Catal. Today 256 (2015) 347–357.

[33] Z. Dai, Q. Sun, X. Liu, C. Bian, Q. Wu, S. Pan, L. Wang, X. Meng, F. Deng, F.S. Xiao, J. Catal. 338 (2016) 202–209.

[34] R.R. Haikal, A.B. Soliman, M. Amin, S.G. Karakalos, Y.S. Hassan, A.M. Elmansi, I.H. Hafez, M.R. Berber, A. Hassanien, M.H. Alkordi, Appl. Catal. B Environ. 207 (2017) 347–357.

[35] Z. Xue, J. Jiang, M.-G. Ma, M.-F. Li, T. Mu, ACS Sustain. Chem. Eng. (2017) acssuschemeng.6b02972.

[36] L.-G. Ding, B.-J. Yao, W.-L. Jiang, J.-T. Li, Q.-J. Fu, Y.-A. Li, Z.-H. Liu, J.-P. Ma, Y.-B. Dong, Inorg. Chem. 4 (2017) 2337–2344.

[37] Z.-Z. Yang, Y. Zhao, G. Ji, H. Zhang, B. Yu, X. Gao, Z. Liu, Green Chem. 16 (2014) 3724–3728.

[38] M. Liu, B. Liu, L. Liang, F. Wang, L. Shi, J. Sun, J. Mol. Catal. A Chem. 418–419 (2016) 78–85.

[39] T. Lescouet, C. Chizallet, D. Farrusseng, ChemCatChem 4 (2012) 1725–1728.

[40] T. Ema, Y. Miyazaki, J. Shimonishi, C. Maeda, J.-Y. Hasegawa, J. Am. Chem. Soc. 136 (2014) 15270–9.

[41] R. Srivastava, D. Srinivas, P. Ratnasamy, Microporous Mesoporous Mater. 90 (2006) 314–326.

[42] T. Sakai, Y. Tsutsumi, T. Ema, Green Chem. 10 (2008) 337.

[43] T. Takahashi, T. Watahiki, S. Kitazume, H. Yasuda, T. Sakakura, Chem. Commun. (2006) 1664–6.

[44] J.N. Appaturi, F. Adam, Appl. Catal. B Environ. 136–137 (2013) 150–159.

[45] V.B. Saptal, T. Sasaki, K. Harada, D. Nishio-Hamane, B.M. Bhanage, ChemSusChem 9 (2016) 644 – 650.

[46] A.H. Jadhav, G.M. Thorat, K. Lee, A.C. Lim, H. Kang, J.G. Seo, Catal. Today 265 (2016) 56–67.

[47] F.M. Al-Qaisi, M. Nieger, M.L. Kemell, T.J. Repo, ChemistrySelect 1 (2016) 545–548.

[48] C. Gao, J. Ai, H.-R. Tian, D. Wu, Z.-M. Sun, Chem. Commun. 53 (2016) 1293–1296.

[49] Y. He, A. Jawad, X. Li, M. Atanga, F. Rezaei, A.A. Rownaghi, J. Catal. 341 (2016) 149–159.

[50] Y. He, F. Rezaei, S. Kapila, A.A. Rownaghi, ACS Appl. Mater. Interfaces 9 (2017) 16288−16295.

[51] A.A. Rownaghi, A. Kant, X. Li, H. Thakkar, A. Hajari, Y. He, P.J. Brennan, H. Hosseini, W.J. Koros, F. Rezaei, ChemSusChem 9 (2016) 1166–1177.

[52] P.J. Brennan, H. Thakkar, X. Li, A.A. Rownaghi, W.J. Koros, F. Rezaei, Energy Technol. 5 (2017) 327–337.

[53] A.A. Rownaghi, F. Rezaei, Y. Labreche, P.J. Brennan, J.R. Johnson, S. Li, W.J. Koros, ChemSusChem 8 (2015) 3439–3450.

[54] A.A. Rownaghi, D. Bhandari, S.K. Burgess, D.S. Mikkilineni, J. Appl. Polym. Sci. 134 (2017) DOI: 10.1002/APP.45418.

[55] M. Liu, X. Lu, L. Shi, F. Wang, J. Sun, ChemSusChem 2 (2016) 1110–1119.

[56] C.J. Brinker, J. Non. Cryst. Solids 100 (1988) 31–50.

[57] K.S.W. Sing, D.H. Everett, R.A.W. Haul, L. Moscou, R.A. Pierotti, J. Rouquero, T. Siemieniewska, Pure Appl.Chem. 57 (1985) 603–619.

[58] W. Cheng, X. Chen, J. Sun, J. Wang, S. Zhang, Catal. Today 200 (2013) 117–124.

[59] Y.S. Son, S.W. Park, D.W. Park, K.J. Oh, S.S. Kim, Korean J. Chem. Eng. 26 (2009) 1359–1364.

[60] C.A. Montoya, A.B. Paninho, P.M. Felix, M.E. Zakrzewska, J. Vital, V. Najdanovic-Visak, A.V.M. Nunes, J. Supercrit. Fluids 100 (2015) 155–159.

[61] W. Wang, C. Li, L. Yan, Y. Wang, M. Jiang, Y. Ding, ACS Catal. 6 (2016) 6091–6100.

[62] R. Srivastava, D. Srinivas, P. Ratnasamy, J. Catal. 233 (2005) 1–15.

[63] R. Babu, A.C. Kathalikkattil, R. Roshan, J. Tharun, D.-W. Kim, D.-W. Park, Green Chem. 18 (2016) 232–242.

[64] C.M. Miralda, E.E. MacIas, M. Zhu, P. Ratnasamy, M.A. Carreon, ACS Catal. 2 (2012) 180–183.

[65] M. Taherimehr, J.P.C.C. Sertã, A.W. Kleij, C.J. Whiteoak, P.P. Pescarmona, ChemSusChem 8 (2015) 1034–1042.

[66] E. Ju, B. Wucher, F. Rominger, K.W. To, D. Kunz, Chem. Commun. 51 (2015) 1897–1900.

[67] C.J. Whiteoak, A.H. Henseler, C. Ayats, A.W. Kleij, M.A. Pericàs, Green Chem. 16 (2014) 1552.

[68] M.W.C. Robinson, A.M. Davies, R. Buckle, I. Mabbett, S.H. Taylor, A.E. Graham, Org. Biomol. Chem. 7 (2009) 2559–2564.

[69] M. North, R. Pasquale, C. Young, M. North, Green Chem. 12 (2010) 1514–1539.

[70] A. Kant, Y. He, A. Jawad, X. Li, F. Rezaei, J.D. Smith, A.A. Rownaghi, Chem. Eng. J. 317 (2017) 1–8.

[71] Z. Wang, K.K. Tanabe, S.M. Cohen, Inorg. Chem. 48 (2009) 296–306.

SUPPORTING INFORMATION

POROUS POLYMERIC HOLLOW FIBERS AS BIFUNCTIONAL CATALYSTS FOR CO_2 CONVERSION TO CYCLIC CARBONATES

Abbas Jawad, Fateme Rezaei, Ali A. Rownaghi*

Department of Chemical & Biochemical Engineering, Missouri University of Science and Technology, Rolla, MO 65409-1230 USA

Section S1: The porous hollow fiber composites comprising catalyst nanoparticles (i.e., zirconia, titania, and silica) involved into a porous polymer matrix (i.e., PAI) were emphasized in this study. Commercial metal oxides including zirconia, titinia, and silica (average particle size 100 nm, Sigma-Aldrich) were employed as the amine supports. Torlon 4000T-HV, a commercially available polyamide-imide (PAI) (Solvay Advanced Polymers, Alpharetta, GA), and polyvinylpyrrolidone (PVP) (average Mw≈ 1300 K, Sigma-Aldrich) were used for the correspondence of the composite hollow fiber catalysts.

The PVP was dried at 80 °C for 24 h under vacuum to release pre-sorbed water vapor. After that, Torlon was dried at 110 °C for 24 h proceed using De-ionized (DI) water (18MU, Model: D4521, Barnstead International, Dubuque, IA) that was added as a nonsolvent into the fiber dope. N-Methyl-2-pyrrolidone (NMP) was embedded as the solvent to form the spinning dope, which could attribute to its strong solvent power, low volatility, and good water miscibility. Therefore, all solvents and nonsolvents were used as-received with no purification or modification. Methanol and hexane were used for solvent exchange after fiber catalyst spinning. Besides, the methanol was used to remove excess water from the fibers. Namely, spinning dope to create a 20/80 (weight ratio) catalyst/Torlon sorbent contains the polymer PAI, sorbent particles, NMP (solvent), water (nonsolvent), and additives (PVP). The optimized polymer dope compositions and spinning conditions are tabulated in Table S1.

Table S.1. Optimized spinning conditions for corresponding of ZrO_2-polyamide-imide hollow fibers.

Dope composition (ZrO_2/PAI/PVP/NMP/H_2O) (wt %)	**10/19/6/60.5/4.5**
Dope flow rate	600 mL/hr
Sheat fluid (NMP/H_2O)	50/50 wt%
Sheat flow rate	100 mL/hr
Bore fluid (NMP/H_2O)	88/12 wt%
Bore fluid flow rate	200 mL/hr
Air gap	5 cm
Take up rate	8.5 m/min
Operating temperature	55 °C
Quench bath temperature	55 °C

Figure S1 is a schematic representation of the hollow fiber creation process. A standard bore fluid involved in this work consists of NMP and water with the weight ratio of 88:12.[1] An appropriate Torlon core dope composition (determined by cloud point method and rheology measurements) was fed to the middle spinneret compartment.

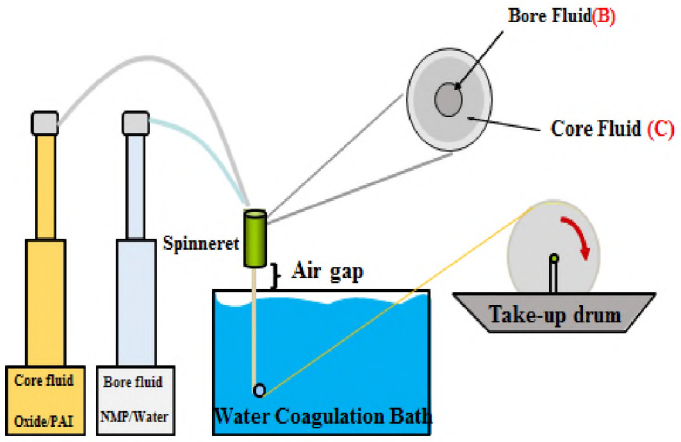

Figure S.1. Schematic diagram of fiber spinning apparatus.

Section S2: Post spinning infusion and amine grafting of ZrO_2-polyamide-imide hollow fibers The 3-Aminopropyltriethoxysilane (APS) was used as the grafting agents for grafting zirconia-Torlon fiber catalysts.[2–4] The amine grafting was performed in a mixture of a non-polar solvent (toluene) and a polar protic solvent (water). The water content of the mixture was kept within the range 0.01- 1.00 wt%. Additionally, water has played a vital role for protonating APS and hydrolyzing methoxy groups in dry liquid. As shown, exposure of APS to moisture obstructs strong hydrogen bonds leads to the formation of polysiloxane. It was clearly that a water content of 1.00 wt% caused the rise to highest amine loading. As a mentioned above, after the ZrO_2-PAIHFs composites were

formed, they were subjected to a methanol solvent exchange process demonstrated by exposure to different APS/toluene/water (ratio 10:89:1 wt%) solution mixtures with varying immersion times, from 1 to 6 h. As a result, the ZrO_2-PAIHFs catalysts were removed from the amine solution and rinsed with hexane for 30 min at ambient temperature to wash away the ungrafted APS deposited onto the fiber surface. Finally, APS-grafted ZrO2-PAIHF catalysts were placed in a preheated vacuum oven and cured for 1 h at 60 °C. The APS aminosilane can form a durable bond with the ZrO2-PAIHFs in this post-spinning immersion step. The optimum infusion condition was determined by soaking 0.15 g of ZrO2-PAIHF catalysts in a 100 g solution of different concentrations of APS in toluene/water mixture (i.e., 5, 10, 15, and 20 wt% APS) at room temperature for 1-8 h. For 10 wt% APS/toluene/water solution and an infusion time of 2 h, the fibers exhibited an optimum amount of amine loading

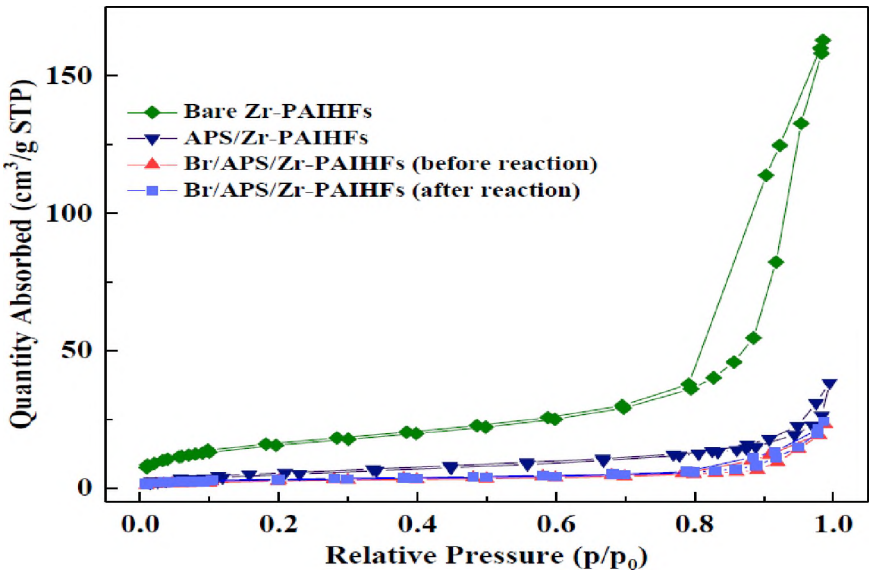

Figure S.2. Nitrogen adsorption/desorption isotherms of bare Zr-PAIHFs, APS/Zr-PAIHFs, Br/APS/Zr-PAIHFs (before reaction) and Br/APS/Zr-PAIHFs (after reaction) at 77 K.

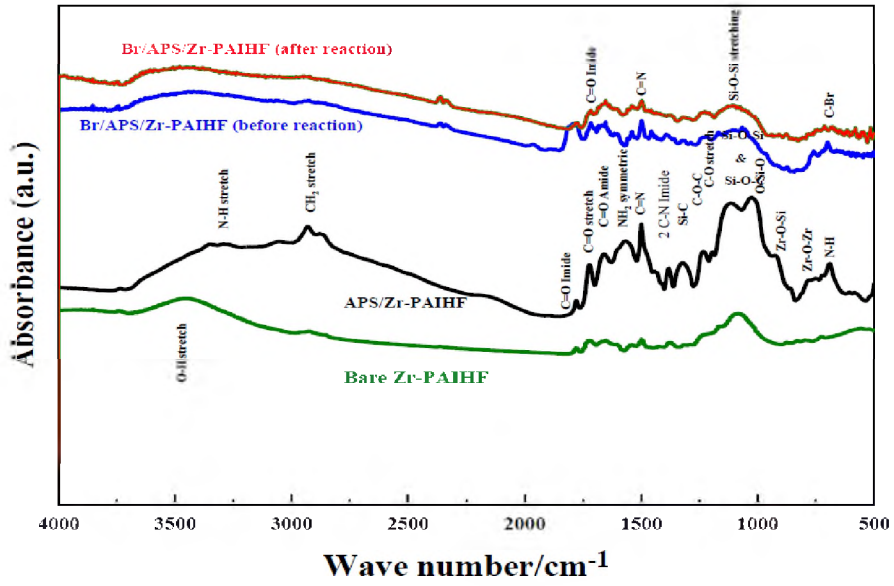

Figure S.3. The FT-IR spectra of bare Zr-PAIHF, APS/Zr-PAIHF and Br/APS/Zr-PAIHF catalyst before (a) and after (b) reaction.

REFERENCES

[1] A.A. Rownaghi, D. Bhandari, S.K. Burgess, D.S. Mikkilineni, J. Appl. Polym. Sci. (2017) DOI: 10.1002/APP.45418.

[2] A.A. Rownaghi, A. Kant, X. Li, H. Thakkar, A. Hajari, Y. He, P.J. Brennan, H. Hosseini, W.J. Koros, F. Rezaei, ChemSusChem 9 (2016) 1166–1177.

[3] Y. He, A. Jawad, X. Li, M. Atanga, F. Rezaei, A.A. Rownaghi, J. Catal. 341 (2016) 149–159.

[4] Y. He, F. Rezaei, S. Kapila, A.A. Rownaghi, ACS Appl. Mater. Interfaces 9 (2017) 16288−16295.

II. HIGHLY EFFICIENT Pt/Mo-Fe/Ni-BASED Al_2O_3-CeO_2 CATALYSTS FOR DRY REFORMING OF METHANE

Abbas Jawad, Fateme Rezaei, Ali A. Rownaghi*

Department of Chemical & Biochemical Engineering, Missouri University of Science and Technology, 1101 N. State Street, Rolla, Missouri 65409, United States

ABSTRACT

Herein, the activity and stability of Ni-based Al_2O_3-CeO_2 supported monometallic Mo, bimetallic Fe-Mo and Pt-Mo, and trimetallic Pt-Fe-Mo complex catalysts were evaluated in the carbon dioxide dry reforming of methane. The catalysts were prepared by incipient wetness impregnation method using various amounts of Ni, Fe, Mo and Pt, and were characterized by BET, XRD, XRF, H_2-TPR, CO_2-TPD, and FTIR-Pyridine techniques. The catalytic performance of the as-synthesized Ni-based Al_2O_3-CeO_2 complex catalysts were investigated in a fixed-bed continuous-flow reactor at various reaction temepratures (550-700 °C), space velocity of 12,000 $ml g_{cat}^{-1}$ h^{-1} and different feedstocks (pure CH_4 or 50% CH_4/CO_2 mixture) under atmospheric pressure for 10 h time-on-stream. The co-doped Ni/Al_2O_3-CeO_2 catalyst with Mo and Fe was found to significantly enhance the catalyst performance (more than 80% methane and 86% CO_2 conversions). Further, our results indicated that the addition of 0.005 wt% Pt to the FeMo/Ni/Al_2O_3-CeO_2 complex catalyst leads to an excellent catalytic performance at 700 °C during the dry reforming reaction. Pt/FeMo/Ni/Al_2O_3-CeO_3 demonstrated good activity/selectivity with very low carbon deposition.

Keywords: Composite catalyst, Dry reforming of methane, Ni-based Al_2O_3-CeO_3, CH_4 conversion, H_2/CO ratio.

1. INTRODUCTION

Dry reforming of methane (DRM) with carbon dioxide is a well-studied reaction for production of syngas ($CO+H_2$) that could be utilized to produce a wide range of products such as higher alkanes and oxygenates by means of Fischer-Tropsch synthesis [1,2]. DRM was first demonstrated by Fischer and Tropsch over Ni and Co catalysts in 1928 [3]. They observed severe deactivation due to carbon deposition that was later addressed for the more general case of steam/CO_2 reforming of hydrocarbons by Reitmeier et al. [4]. Industrially, syngas is mainly produced by steam reforming of methane (SRM). However, SRM generally produces CO_2 along with CO and H_2 that necessitates further CO_2 capture process [5]. Moreover, the H_2/CO ratio of 3:1 obtained from SRM is too high to be used for chemical synthesis [6–8]. DRM on the other hand, utilizes two abundantly available greenhouse gases to produce high purity syngas containing little CO_2, with H_2/CO ratio of 1, albeit it is highly endothermic [9,10]. DRM is inevitably accompanied by deactivation due to carbon deposition [1,11].

Nickel-based catalysts have been utilized for reforming reactions as they are relatively cheap and possess high activity [12,13]. Nevertheless, due to the high-temperature reaction of the reforming process, the nickel catalysts deactivate quickly due to sintering of the active metal phase and coke deposition. It is well-definition that noble metals inhibit coke deposition, and the carbon obtained differs in nature from that formed

over Ni catalysts. Moreover, it has been reported that a small amount of noble metals can promote the reducibility of the base metal, such as Ni, and stabilize its degree of reduction during the catalytic process [14]. It is well definition, that the structure and surface properties of the support exert a significant impact on the catalytic performance of supported catalyst. Therefore, the investigation of new catalysts supported on suitable carrier is still a research priority. It is known that impart metal-support interactions has been extensively studied due to plays a synergistic role in the activity and stability of nickel catalysts. Mainly, it also has been suggested that carbon deposition can be attenuated or even suppressed as the active metal is supported on a carrier with strong Lewis basicity [15]. Increasing the concentration of Lewis basicity of the support enhances the chemisorption of CO_2 in the DRM reaction. Hence, the alkali metal oxides (such as K_2O, Cs_2O, etc.) and alkaline earth metal oxides (such as MgO, CaO, BaO) or rare earth oxides (such as CeO_2) [16,17] are commonly chosen as basic supports or modifiers [18]. On one hand, the presence of the basic modifiers promotes the process of eliminating the coke through the course that CO_2 reacts with the C to form CO, thereby improving the stability of the catalyst. On the other hand, the chemisorption of the CO_2 activates the CO_2 molecule and augments the concentration of CO_2 on the surface of the catalyst, which is beneficial to boost the catalytic activity of the catalyst [9,19]. The presence of rare earth oxides such as ceria that possess high oxygen storage capacity can enhance the reversible oxygen adsorption/release capability of the catalyst [20] and therefore, it has been intensely investigated as a promising route for developing efficient methane reforming catalysts. In addition, improving the catalytic performance by increasing metal dispersion has been

suggested as another promising approach to overcome the limitation of the current materials [21].

One of most fascinating approaches for enhancing activity and stability in methane-reforming reactions is to use bimetallic/trimetallic catalysts. There has recently been a resurgence of research into Fe-modified Ni catalysts because the addition of Fe provides redox functionality to the catalyst, giving it the ability to restrain carbon formation as well as to o improve the metal-support interaction thus, leading to high dispersion [22,23]. Theofanidis et al.[24] studied various dry reforming of methane conditions over a Ni-based catalyst supported on $MgFexAl_{2-x}O_4$. The authors emphasized on the existence of a strong metal support interaction, which contributed to the elimination of sintering and thus resulted in stable catalytic activity and a good resistance carbon deposition. Huang et al.[25], studied Ni-Mo incorporated SBA-15 as a dry reforming catalyst and compared to monometallic Ni/SBA-15. They observed that the catalyst exhibits stable performance with less carbon deposition despite a lower initial activity. The superior reactivity of the bimetallic Ni-Mo/SBA-15 was assigned to strong metal support interactions, strong basicity and small metal particle size. Consequently, the presence of Mo on the catalyst resulted the formation of molybdenum carbides, which has been suggested to have a high coking resistance [26].

In the present paper, the DRM reaction was investigated on a series of Ni-based CeO_2-Al_2O_3 catalysts, as one of the most effective catalysts for this reaction. Incipient impregnation method was used to prepare the catalysts and their chemical, structural and physical properties were investigated by various characterization tools. In evaluating the catalytic efficiency of the materials in DRM reaction, great attention was paid to the

influence of various promoters (Pt, Fe, and Mo) as bi/trimetallic on the properties of Ni-based CeO_2-Al_2O_3 catalysts.

2. EXPERIMENTAL SECTION

2.1. CATALYST SYNTHESIS

The CeO_2-Al_2O_3 support with CeO_2 contents of 50 wt% on Al_2O_3 were prepared by impregnation $Ce(NO_3)_3.6H_2O$ with $Al(NO_3)_3.9H_2O$ provided by Sigma-Aldrich. The obtained sample was dried overnight at 100 °C and subsequently calcined at 500 °C for 5 h. Ni-based Al_2O_3-CeO_2 supported monometallic Mo, bimetallic Fe-Mo and Pt-Mo, and trimetallic Pt-Fe-Mo complex catalysts were prepared by incipient wetness impregnation technique, dried overnight at 110 °C and then calcined in a muffle furnace at 550 °C for 4 h. A necessary amount of each metal precursor (*i.e.* $Ni(NO_3)_2.6H_2O$, Mo $(NO_3)_2.5H_2O$, $Fe(NO_3)_3 \cdot 9H_2O$ and $Pt(NH_3)_4.(NO_3)_2$ from Sigma-Aldrich) was dissolved in deionized water and then mixed with the catalyst support in the adequate molar ratio. The metal loadings were set at 4 wt% nickel for Ni/CeO_2-Al_2O_3; 2 wt% nickel, 2 wt% iron for Fe/Ni/CeO_2-Al_2O_3; 2 wt% nickel, 2 wt% iron, and 0.5 for molybdenum for Mo-Fe/Ni/CeO_2-Al_2O_3; 2 wt% nickel, 2 wt% iron, 0.5 for molybdenum, and 0.005 wt% platinum for Pt/Mo-Fe/Ni/CeO_2-Al_2O_3.

2.2. CATALYST CHARACTERIZATION

The X-ray diffraction (XRD) patterns of the catalysts were obtained by a diffractometer (PANalytical) operated at 30 kV and 15 mA with Cu Kα1 monochromatized

radiation (λ = 0.154178 nm). XRD patterns were measured at a scan rate of 0.026°/s. N_2 physisorption isotherm measurements were carried out in Micromeritics 3Flex surface characterization analyzer at -196 °C. Textural properties such as surface area, total pore volume, micropore volume, and average pore width were determined using Brunauer-Emmett-Teller (BET), Barrett-Joyner-Halenda (BJH), and t-plot methods, respectively. Prior to the measurements, samples were degassed under vacuum at 250 °C for 6 h in a Micromeritics PreVac. H_2-temperature programmed reduction (TPR) measurements were carried out in a U-shaped quartz cell using a 5% vol H_2/He gas flowing at 50 cm^3/min with a heating rate of 10 °C/min up to 900 °C using the Micromeritics 3Flex analyzer. Hydrogen consumption was followed by on-line mass spectroscopy (BELMass) and quantitative analysis was done by comparison of reduction signal with hydrogen consumption of a CuO reference. Temperature-programmed desorption of CO_2 (CO_2-TPD) was performed on the same Micromeritics 3Flex analyzer. Prior to adsorption measurement, all samples were initially reduced at a temperature of 200 °C in a 5% H_2 in He gas mixture and held at the reduction temperature for 1 h, then cooled down to 50 °C under He. After the temperature stabilized, the sample was exposed to 10% CO_2 in He for 30 min. To remove physically bound CO_2 from the surface, a flow of He (50 cm^3/min) for 30 min at 50 °C was used. The desorption of CO_2 was measured from 50 to 600 °C at a constant heating rate of 10 °C min^{-1}. To determine the nature of surface acid sites, Fourier-transform infrared spectroscopy (FTIR) of pyridine adsorbed samples using a Bruker Tensor spectrophotometer that was employed to determine the types of acid sites present in the samples. All samples were activated at 450 °C for 4 h to release the moisture before the adsorption of pyridine and cooled down to 60 °C for adsorption pyridine until saturation. All of the measured spectra

were recalculated to a "normalized" wafer of 10 mg. For quantitative characterization of acid sites, the bands at 1450 and 1550 cm^{-1} correspond to Lewis and Brønsted sites respectively. The chemical composition of materials was determined by X-ray fluorescence (XRF) analysis using X-Supreme8000 to estimate weight percent loading of the metals.

2.3. CATALYTIC TESTS

The catalytic performance of the catalysts for dry reforming coupling of methane with CO_2 were investigated at various reaction temperatures using a stainless-steel micro-reactor (ID = 12.7 mm, h = 300 mm). The feed gase used consisted of either pure CH_4 or 50% CH_4/CO_2 and its flow rate to the reactor was controlled and regulated by a digital mass flow controller (Brooks Instrument). The reactor was placed vertically inside an electric furnace to control the reaction temperature. The catalyst was diluted with sand (particle size 0.5 μm) with the ratio of 1:6 and loaded into the reactor. Sufficient amount of quartz wool was embedded into the reactor on the top and bottom of catalyst to keep the catalyst stable. The weight of the catalyst load was 300 mg (particle size 0.5 μm) while the gas flow rate was set at 60 mL/min based on the desired space velocity (12,000 mL g_{cat}^{-1} h^{-1}). A type-K thermocouple was embedded inside the center of the reactor and the reactions were carried out isothermally for 10 h. The exit gas mixture was analyzed by on-line (SRI 8610C) gas chromatography (GC) every 30 min. The flame ionization detector (FID) was employed to analyze the hydrocarbons (C_1-C_6) and thermal conductivity detector (TCD) was used to analyze CO, H_2, and CO_2 as well as other hydrocarbons. Before reaction, the catalysts were treated with N_2 at 500 °C and flow rate of 40 mL/min for 30 min to remove water. In addition, prior to each catalytic measurement, the catalyst was reduced *in-situ* in

a flow of 10% H_2/He (total flow rate of 60 mL min^{-1}). The temperature was increased to 700 °C for 1 h followed by purging the bed with flowing N_2 (60 mL min^{-1}) for 40 min to remove physically adsorbed hydrogen on the surface of the catalyst.

3. RESULTS AND DISCUSSION

3.1. CATALYST CHARACTERIZATION

XRD was used for the characterization of bulk phase feature of the composite catalysts. Figure 1 show the XRD patterns of Ni-based Al_2O_3-CeO_2 composite catalysts. The diffraction peaks recorded at 2θ =28, 33, 48, 57, 69, 77, 79, and 89° indicate the presence of cubic crystal structure of CeO_2 support. In addition, it can be observed that all samples present diffraction peaks at 2θ = 38, 46, and 67°, attributed to the γ-Al_2O_3 support. However, the absence of any other additional crystalline phases related to MoO, Fe_2O_3, and Pt species in the diffractogram points indicated they may be either in low quantity and/or all these promoters were highly dispersed as very small particles on the support, resulting in successful incorporation of, molybdenum, iron, and platinum cations into Al_2O_3-CeO_2 [27]. Furthermore, the XRD spectra did not show any diffraction peaks related to NiO or $NiAl_2O_4$ spinel phase, which could likely indicate that Ni was highly dispersed on the catalyst support and hence could not be obviously detected by XRD [28]. Notably, the characteristic peaks of Al_2O_3-CeO_2 in the catalysts containing rare-earth elements shifted toward lower 2θ values, illustrating the formation of new spinel-like phase or defects with spinel structure [29,30]. The crystallite sizes of the samples were also quantified by applying the Debye-Scherrer equation and the size of the Ni particles were

determined to be less than 50 nm, as listed in Table 1. The results reveal that the average crystal size was in nanometers scale and that the addition of Pt nanoparticles slightly decreased the crystallite size. These findings are in good agreement with previous literature [31].

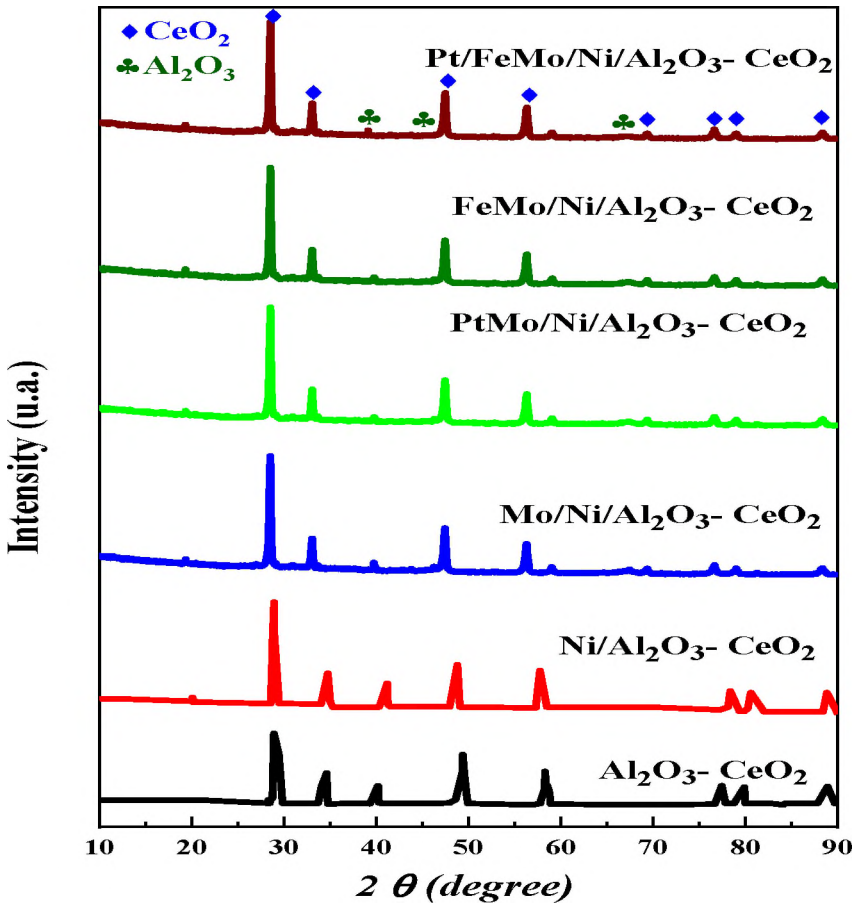

Figure 1. XRD patterns of Ni-based Al_2O_3-CeO_2 composite catalysts.

The nickel crystal size Ni-based Al_2O_3-CeO_2 composite catalysts was found to be inversely proportional to the added second and third elements [27]. The Ni crystal size reduced from 36 to 24 and 25 nm in the presence of Pt-Fe and Pt-Fe-Mo, respectively. This phenomenon could be linked to the effects of platinum, iron, molybdenum, and nickel that

remained on the surface of the sample that inhibited the growth of Ni crystals, as confirmed by XRF elemental analysis. The XRF results in Table 1 reveal that the Ni, Mo, Fe, and Pt loading was slightly higher than the estimated theoretical value as a result of incomplete precipitation of aluminum and cerium metal precursors during the process of impregnation, resulting in a higher Ni, Mo, Fe, and Pt content in the catalysts [32]. The active metal surface area (ASA) was calculated from Eq. (1) in which D represents the average diameter of Ni crystal that is estimated by XRD, L is the weight fraction metal loading, α is the shape correction factor ($\alpha = 1$ for a sphere), f indicates the particle shape correction factor ($f = 6$ for a sphere), and Z indicates the density of the metal [33]. Furthermore, Ni^0 dispersion (D_{Ni}) was calculated from the Eq.(2), where FW indicates the formula weight of the supported metal, and N is Avogadro's number, and A is the metal surface area per atom (for Ni, A = 6.494 $Å^2$/atom) [33]. Based on the Ni particle size, the Ni dispersion was calculated to be 27–42%, indicating the formation of highly dispersed Ni metal particles. The high dispersion of the Ni nanoparticles is considered to be resulted from the homogeneous distribution of Ni^{2+} species in the (MNiAlCe)O, M = (Fe, Mo, and Pt) calcined product as well as the strong interaction between Ni and Fe, Mo, and Pt. This has been confirmed by XRD profiles, as discussed earlier (Figure 2).

$$ASA\ (m^2/g) = \frac{L \times f \times \alpha}{(100 \times D \times Z)} \tag{1}$$

$$D_{Ni}(\%) = \frac{ASA \times FW}{(N \times A \times L)} \tag{2}$$

Table 1. XRD and XRF analysis results of Ni-based Al_2O_3-CeO_2 composite catalysts.

Catalysts	Metal loading (wt%) [a]						D (nm)[b]	ASA[c]	D_{Ni}[d]
	Al	Ce	Ni	Fe	Mg	Pt			
Al_2O_3-CeO_2	45	42	-	-	-	-	-	-	-
Ni/Al_2O_3-CeO_2	43	41	4.721	-	-	-	36	0.088	27.98
Mo/Ni/Al_2O_3-CeO_2	45	39	4.612	-	0.573	-	30	0.104	33.84
PtMo/Ni/Al_2O_3-CeO_2	41	37	4.558	-	0.545	0.004	24	0.128	33.84
FeMo/Ni/Al_2O_3-CeO_2	44	38	4.395	2.312	0.548	-	31	0.096	32.93
Pt/FeMo/Ni/Al_2O_3-CeO_2	40	38	4.117	2.258	0.546	0.003	25	0.111	40.45

[a]Estimated by XRF analysis.
[b]Estimated by Debye-Scherrer equation for NiO (200) of XRD.
[c]Calculated from equation 1.
[d]Calculated from equation 2.

Furthermore, the size of Ni^0 in metal-doped Ni/Al_2-O_3-CeO_2 catalysts was significantly smaller than those in bare Ni/Al_2-O_3-CeO_2, as estimated by the Scherrer equation ($D = K\lambda/(\beta \cos \theta)$), and as confirmed by the XRD patterns. This indicates that the doping of metal oxides greatly promoted the dispersion of Ni particles within the catalyst matrix.

H_2-TPR analysis was performed to investigate the reducibility of the catalysts and to analyze the interactions between metal species and the support. The H_2-TPR profiles of Ni-based Al_2O_3-CeO_2 composite catalysts are presented in Figure 2. For all catalysts, the H_2-TPR curves can be deconvoluted into three to five peaks, as demonstrated in this figure. It can be clearly seen that the addition of promoters increased the intensity of reduction peaks, highlighting the increase in reducibility of NiO species in promoted catalysts. Figure 2 shows that Al_2O_3-CeO_2 catalyst was readily reducible in the range of 589-708 °C which is associated with the bulk reduction of Ce^{4+} to Ce^{3+} [29]. The Ni-based Al_2O_3-CeO_2

catalyst displayed two well-defined reduction peaks at 611-641 and 727-790 °C. The low-temperature reduction is associated to surface Ni species which are easily reducible, whereas the high-temperature peak is correlated with reduction of NiO species that lead to a strong interaction with the Al_2O_3-CeO_2 support to produce metallic Ni and reduce $NiAl_2O_4$ spinel phase [34]. Generally, the TPR profiles of bi/trimetallic catalysts are different from those of monometallic catalysts, suggesting that the formation of bi/trimetallic bonds greatly affects the reduction kinetics. Ni-modified molybdenum and iron bi/trimetallic catalysts enhanced the reduction process and caused decay of the peak connected with unbounded NiO [35].

Regarding Mo-containing catalysts, it is well known that bulk MoO_3 is reduced only at very high temperatures following a two-stage process: a first stage corresponding to the reduction of MoO_3 to MoO_2 in the 750-800 °C range, and a second stage occurring at 950-1000 °C, resulting from the reduction of MoO_2 to metallic Mo [36]. Moreover, after Ni/Al_2O_3-CeO_2 modification with MoO_3, three reduction peaks were observed at around 307-408, 774-819, and 886 °C. The first peak, with maximum intensity at 408 °C, is assigned to the reduction of Ni^{2+} to Ni^0. According to the literature, this peak can be attributed to the concomitant reduction of nickel oxide species (Ni^{2+} to Ni^0) and highly dispersed octahedral Mo^{6+} species (from Mo^{6+} to Mo^{4+}) [37].

Considering that the partial reduction of amorphous multilayered Mo oxides in octahedral coordination proceeds at a lower temperature (< 600 °C) [38], the TPR profile of the Mo/Ni/Al_2O_3-CeO_2 sample suggests a low ratio of this Mo structure. The second peak at 774 °C could be attributed to the reduction of $NiMoO_4$ to Ni and MoO_3, and MoO_2 to MoO at 819 °C. Finally, the highest peak observed at 886 °C indicates the reduction of

MoO to metallic Mo and metal aluminates. The presence of high-temperature peaks indicates a strong interaction of NiO with the Al_2O_3-CeO_2 support [39]. Moreover, the presence of these species increases considerably the reduction temperature and the magnitude of the NiO peak. The increase in the reduction temperature could be attributed to the presence of Mo oxo-species that favor NiO with respect to Ni^0 [40], resulting in the formation of well-dispersed NiO phase which is further transformed into well-dispersed Ni^0 upon reduction, in full agreement with the XRD results.

The addition of Fe_2O_3 lowered the reduction temperature of ceria. Wimmers et al. [41] studied the reduction of Fe_2O_3 and proposed a reduction in two steps $Fe_2O_3 \rightarrow Fe_3O_4 \rightarrow Fe$, with no formation of FeO. For the same oxide, other authors proposed a three-step reduction process which considered FeO formation dealing with: $Fe_2O_3 \rightarrow Fe_3O_4$ at about 400 °C, $Fe_3O_4 \rightarrow FeO$ at about 600 °C and finally $FeO \rightarrow Fe$ at higher temperatures [42]. Furthermore, during the second and third reduction steps, the Ni and part of the Fe are reduced to metals and form a Ni-Fe alloy. Irrespective of the number of reduction steps of the Fe_2O_3, the separation of its reduction from that of the CeO_2 overlapping reduction zones is difficult to obtain. However, the Ni-based Al_2O_3-CeO_2 composite catalysts without any platinum content were reduced at much higher temperatures than catalysts with platinum.

The addition of platinum helped further decrease the reduction temperature significantly. Therefore, the PtMo/Ni/Al_2O_3-CeO_2 and Pt/FeMo/Ni/Al_2O_3-CeO_2 catalysts allow reduction in the selectivity toward carbon (hence lower coke formation) and reach values closer to equilibrium at lower reaction temperatures. Moreover, this implies that the platinum interaction with the support has a significant effect on increasing the reducibility of the support [43]. The presence of Pt facilitates the dissociation of molecular hydrogen

adsorption. Hydrogen has been identified to adsorb and dissociate on the surface of the platinum whereby it spills over to the entire surface of the support [44]. On the metallic surface, hydrogen molecules dissociate to hydrogen atoms which diffuse toward Ni^{2+} and can react with NiO, thus leading to a higher dispersion of active metal nanoparticles. Nevertheless, the rate of reduction of NiO depends not only on its chemical nature but also on nucleation process by which metallic nuclei are generated [45]. Compared with $Mo/Ni/Al_2O_3$-CeO_2 and $FeMo/Ni/Al_2O_3$-CeO_2 catalysts, it can be assumed that NiO is highly dispersed in $Pt/MoNi/Al_2O_3$-CeO_2 and $Pt/FeMo/Ni/Al_2O_3$-CeO_2. The $Pt/FeMo/Ni/Al_2O_3$-CeO_2 could be more easily reduced by hydrogen atoms from spillover effect due to the unique interaction among Ni and Pt species and served as metallic nuclei to facilitate reduction of Fe^{+2} and Ni^{2+}.

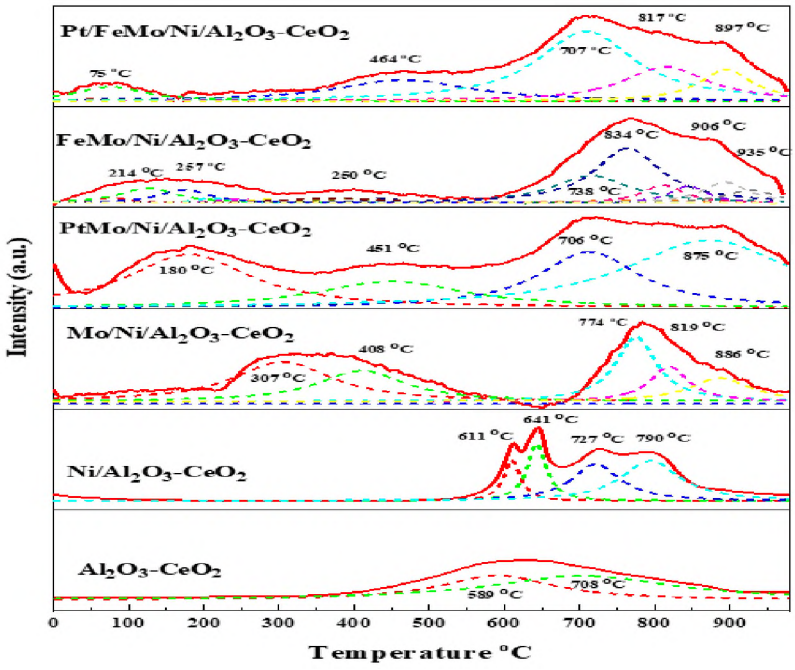

Figure 2. H_2-TPR profiles Ni-based Al_2O_3-CeO_2 composite catalysts.

The Al_2O_3-CeO_2 support plays a key role in the active sites dispersion, activity and stability. To improve reducibility, enhance the oxygen mobility and metal dispersion, γ-Al_2O_3 material was modified by adding CeO_2 to form Al_2O_3-CeO_2 support. Further addition of metal oxide promoters improves reducibility and chemisorption capacity of Ni-based Al_2O_3-CeO_2 catalyst due to a better dispersion of bi/trimetallic on the Al_2O_3-CeO_2 support. Finally, the catalysts promoted with molybdenum, iron, and platinum are less reducible than the monometallic Ni-based catalyst mainly due to the increase in metal-support interaction and a better nickel dispersion. On the basis of these results, it can be concluded that metal oxides species reduce the Ni particles size and improve the interaction between the Ni species and the support [46].

The basicity of the reduced Ni-based Al_2O_3-CeO_2 composite catalysts was investigated by CO_2-TPD measurements and the corresponding results are presented in Figure 3 and Table 2. The profiles shown in Figure 3 are generally composed of wide CO_2-desorption peaks that can be deconvoluted into three main types of contributions [47]: (i) weak basic sites at CO_2-desorption temperature of 60–200 °C, associated with weak Brønsted basic sites that lead to bicarbonates formation on weakly basic OH groups, (ii) intermediate strength basic sites associated with Lewis acid-base and formed bidentate carbonates on metal-oxygen pairs at CO_2-desorption temperature of 200–400 °C, and (iii) high temperature CO_2-desorption (400–800 °C), related to adsorption on low coordination oxygen anions and formation of unidentate carbonates on strongly basic surface O^{2-} anions acting as strong basic sites.

The catalysts promoted with MO_x possess weak, middle and strong basic sites, as opposed to other DRM catalysts that only contain weak and middle basic sites. These

results indicate that Mo addition can improve CO_2 chemisorption and dissociation, which would supply enough oxygen species for gasification of intermediate carbons, hence dramatically promoting the lifetime of the catalysts.

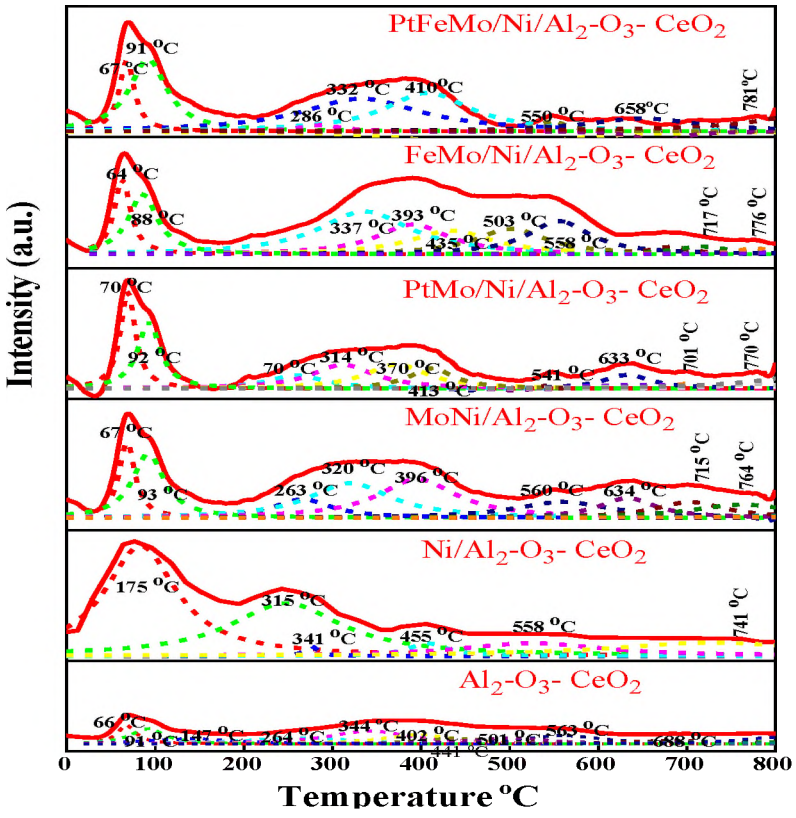

Figure 3. CO_2-TPD profiles of Ni-based Al_2O_3-CeO_2 composite catalysts.

Additionally, the CO_2-TPD results showed that trimetallic Fe-containing catalysts exhibit high Lewis basicity compared with their bi/monometallic catalyst analogues, which in turn enhances the ability of the catalysts to chemisorb CO_2 [10]. Similar results were reported by Yao et al. [48] for magnesia-zirconia oxides. Furthermore, it was observed that upon Pt addition, the basicity of the Ni/Al_2O_3-CeO_2 increases, resulting in the enhancement

of the rate of activation of mildly acidic CO_2, which will in turn assist in oxidation of surface carbon and promoting the catalyst resistance to deactivation [1]. The results of integration peaks and deconvolution of the CO_2-TPD profiles along with the total basicity of the catalysts can be found in Table 2. Moreover, the results indicated that upon Fe doping, the total basicity of the catalyst increases dramatically, especially in terms of intermediate and strong basic sites.

Table 2. Summary of CO_2-TPD of Ni-based Al_2O_3-CeO_2 composite catalysts.

Catalysts	CO_2-TPD ($mmolg^{-1}$)			
	Medium base peak (60-200 °C)	Medium base peak (200-400 °C)	Strong base peak (400-800 °C)	Total
Al_2O_3-CeO_2	0.11	0.15	0.09	0.35
Ni/Al_2O_3-CeO_2	-	0.34	0.11	0.45
Mo/Ni/Al_2O_3-CeO_2	0.10	0.16	0.40	0.76
PtMo/Ni/Al_2O_3-CeO_2	0.29	0.11	0.92	1.32
FeMo/Ni/Al_2O_3-CeO_2	0.07	0.25	0.50	0.98
Pt/FeMo/Ni/Al_2O_3-CeO_2	0.21	0.57	0.73	1.51

[a] Total basic site amount, and weak, medium, and strong basic peak centers were estimated from CO_2-TPD profiles.

To investigate the existence of Lewis and Brønsted acid sites in the composite catalysts, the Fourier-transform infrared spectroscopy (FTIR) analysis was conducted on a Bruker Tensor spectrophotometer using pyridine as a base probe molecule [49,50]. The spectra were taken on protonated samples after pyridine desorption at 150 °C for 2 h and

cooling down to the room temperature. It is well established that the vibration modes of the ring breathing υ(CCN) (υ_{8a}, υ_{8b}, υ_{9a}, and υ_{9b}) that appear in the frequency range between1650 and 1400 cm^{-1} are sensitive to pyridine adsorption. Pyridine can be interacted with the surface in three ways: (i) the nitrogen lone pair can be linked to the hydrogen (H-bond) of weakly acidic hydroxyl groups causing a very weak perturbation in the adsorbed molecule (the interaction is symbolically assigned [H-Py]); (ii) if the Brønsted acidity of a surface hydroxyl group is sufficiently high, a proton can be extracted to yield pyridinium ion formation (the interaction is symbolically assigned [Py-H^+ or B-Py]); and (iii) the pair of electrons of nitrogen can be interacted by charge donation to the unsaturated cation coordinated to the surface (the interaction is symbolically assigned [L-Py]). The IR frequencies of the various forms of adsorbed pyridine are listed in Table 3. While the intensity of the lower frequency L-Py band is used to calculate the amount of Lewis acid sites, evaluation of their strength can be made based on the positions of the higher frequency band, this implies that the wave number grows with the site strength.

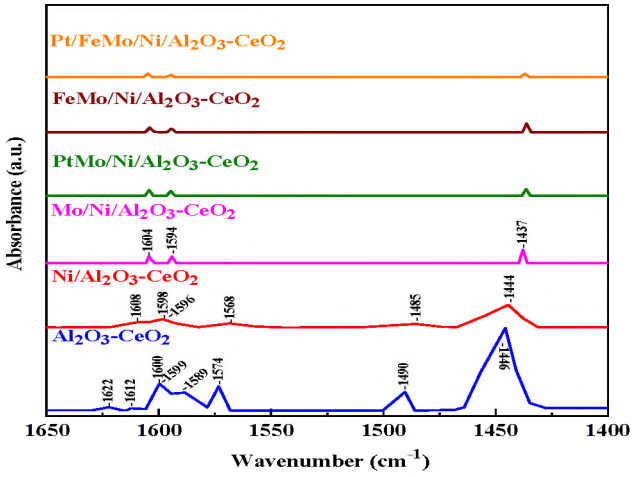

Figure 4. IR υCCN spectra of adsorbed Pyridine on Ni-based Al_2O_3-CeO_2 composite catalysts.

Figure 4 depicts the bands at 1438, 1446, 1574, 1588, and 1590-1596 cm^{-1} which are assigned to the formation of H-bonded Py molecules (H-Py species). The bands at 1444, 1485, 1490, 1598, and 1600-1622 cm^{-1} are related to pyridine adsorbed on Lewis acid sites (L-Py species), whereas the bands at 1485 and 1568 cm^{-1} are assigned to pyridine associated with both Lewis and Brønsted acid sites [51]. Notably, the spectra of pyridine adsorbed on the Ni/Al_2O_3-CeO_2 displayed two bands at 1596 and 1598 cm^{-1} which could be assigned to three types of species bond to the isolated Al^{3+} sites in tetrahedral sites (1609 cm^{-1}) with low frequency shoulders. The same shoulders, but better defined, were detected with the Al_2O_3-CeO_2 and attributed to the υ_{8a} vibration modes of pyridine coordinated to octahedral Al^{3+} Lewis acid sites and two of tetrahedral sites (1622 and 1612 cm^{-1}). The addition of NiO to Al_2O_3-CeO_2 resulted in a decline of its Lewis acidity. Moreover, after pyridine adsorption, the intensity of the band assigned to pyridine coordinated to tetrahedral Al^{3+}sites located near cation vacancy (1622 cm^{-1}) declined while the intensity of other band associated with pyridine coordinated to tetrahedral Al^{3+}cations increased and shifted to 1608 cm^{-1}. Moreover, the intensity of Ni/Al_2O_3-CeO_2 peaks reduced by half as compared with that of Al_2O_3-CeO_2 support.

In full agreement with the X-ray diffraction results, shift of the diffraction lines indicated an initial stage of formation of nickel aluminate with spinel-type structure. This structure is known as an inverse spinel where Ni^{2+} cations occupy the half of the octahedral positions in the structure of the spinel [52]. Furthermore, the IR bands of adsorbed pyridine on the Ni-based catalysts after metal oxides addition (Mo, Fe, and Pt) seem to be less intense than those of the corresponding Ni/Al_2O_3-CeO_2 and Al_2O_3-CeO_2 catalysts. This suggests an additional decrease of the moderate acidity and correspondingly increase in

weak acidity amount. It is likely that the ratio between Brønsted and Lewis acid sites concentration changes due to the formation of weak surface acid sites (associated with the transition metal cations) and the cancellation of Brønsted sites at bands 1540 cm^{-1} which is the result of supplementary filling of the cationic vacancies with Mo^{3+} cations occurred [51].

Table 3. IR frequencies of vibration modes of surface pyridine species.

Vibration modes	IR frequencies, cm^{-1}			
υCCN	Ppy	Hpy	Lpy	Bpy
υ_{8a}	1585	1600-1580	1633-1600	1640-1630
υ_{8b}	1577	1577 and 1574	1585-1575	1613-1600
υ_{19a}	1483	1490-1480	1490-1478	1490-1478
υ_{19b}	1445 and 1435	1447-1440	1460-1445	1540-1500

In order to investigate the BET surface area and pore distribution, N_2 physisorption measurements were conducted on the calcined samples and the isotherms are shown in Figure 5. It can be found that all the calcined catalysts display IV type isotherms with H4 shaped hysteresis loops [53], highlighting that the mesoporous structures of the calcined supports were still preserved after Ni-nitrate and metal oxides impregnation, and after calcination at 550 °C 5 h. Furthermore, their pore size distributions are also very similar to those of the calcined supports, and the position of peaks is in the range of 2.1-7 nm. Therefore, the mesoporous structures of the calcined supports are successfully maintained after Ni-nitrate and metal oxides impregnation, and high temperature calcination. A narrow and uniform pore size distribution could be realized for the catalysts from the sharpness of

the initial step (at P/P_0 = 0.05-0.30) whereas a broad pore size distribution could be observed in the mesoporous region with a primary pore width of 5.6 nm [53].

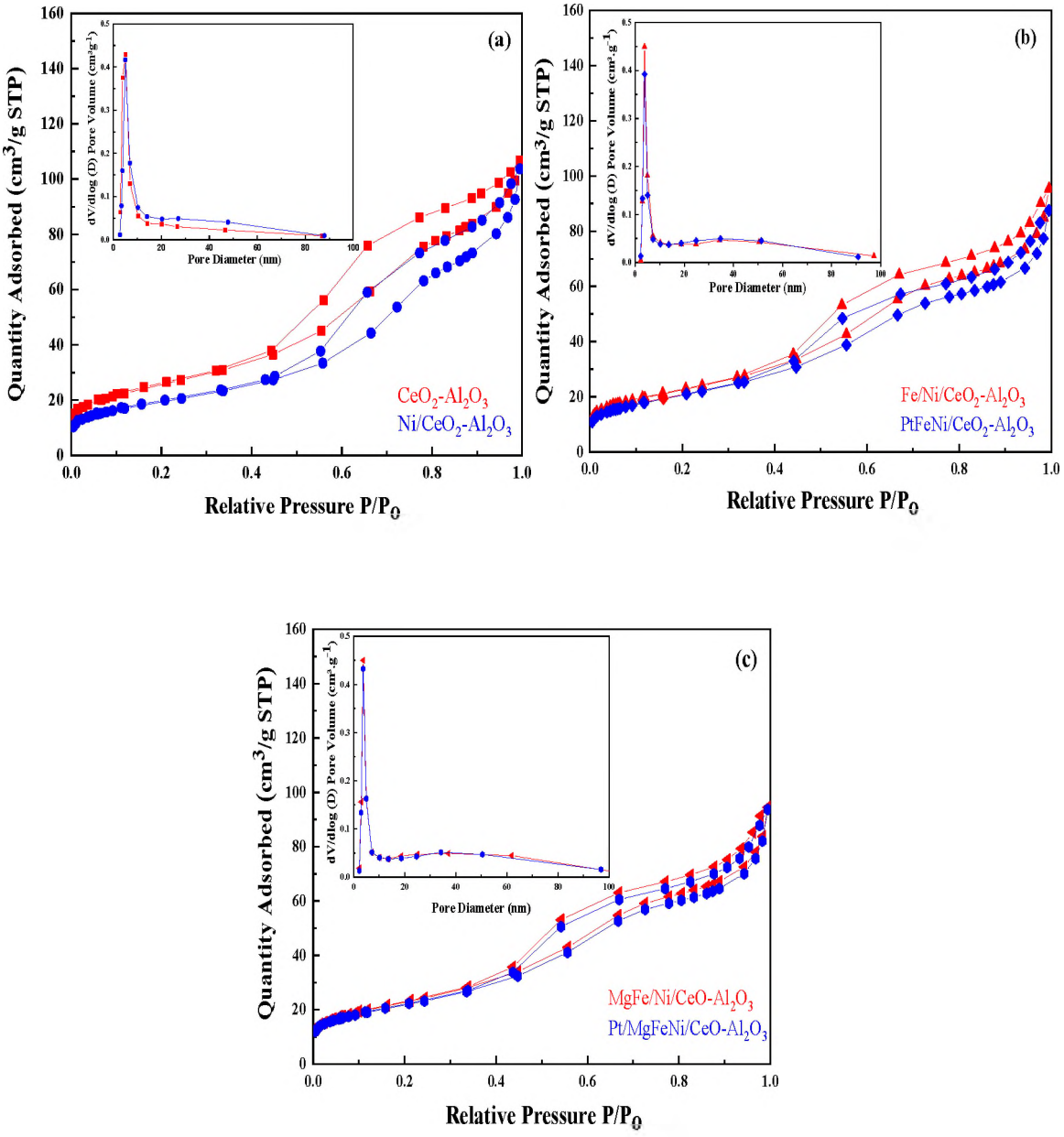

Figure 5. N_2 adsorption-desorption isotherms of calcined Ni-based Al_2O_3-CeO_2 composite catalysts.

The corresponding textural properties of the catalysts are also summarized in Table 4. Compared with the calcined supports, the calcined bi/trimetallic catalysts display relatively smaller specific surface areas. This phenomenon might be caused by partial blockage/clog of pores of the Al_2O_3-CeO_2 support and sintering [53]. Furthermore, compared with the Al_2O_3-CeO_2, the attenuates in BET surface areas of the bi/trimetallic catalysts are relatively small which could be ascribed to strong interactions between Ni species and metal oxides or Ce-doped supports and the excellent dispersion of Ni species onto the modified supports [9].

Table 4. Textural properties of calcined of Ni-based Al_2O_3-CeO_2 composite catalysts estimated from N_2 adsorption-desorption isotherms.

Catalysts	S_{BET} (m^2/g) [a]	S_{mico} (m^2/g) [b]	S_{ext} (m^2/g)	V_{tot} (cm^3/g) [c]	V_{mico} (cm^3/g) [d]	V_{meso} (cm^3/g) [e]	Pore size (nm) [f]
Al_2O_3-CeO_2	92	3	89	0.04	-	0.04	5.59
Ni/Al_2O_3-CeO_2	86	3	66	0.03	-	0.03	5.56
Mo/Ni/Al_2O_3-CeO_2	84	1	88	0.03	-	0.03	5.38
PtMo/Ni/Al_2O_3-CeO_2	79	1	78	0.02	-	0.20	5.59
FeMo/Ni/Al_2O_3-CeO_2	79	1	78	0.03	-	0.03	5.64
Pt/FeMo/Ni /Al_2O_3-CeO_2	77	1	76	0.02	-	0.02	5.59

[a] Estimated by the Brunauer-Emmett-Teller (BET) at the p/p_o in the range of 0.05-0.30.
[b] Micropore area and micropore volumes were determined using the t-plot method.
[c] Estimated by BJH at the adsorbed amount at the p/p_o=0.99 single point.
[d] Estimated by the t-plot method.
[e] Estimated by subtracting V_{micro} from the total volume at P/P_0 = 0.99.
[f] Estimated by BJH desorption average pore diameter.

3.2. CATALYTIC PERFORMANCE

The activity of the various Ni-based Al_2O_3-CeO_2 composite catalysts was investigated in DRM reaction under various reaction temperatures and feed compositions. Both pure CH_4 and CH_4/CO_2 mixture (50:50) were used as reactants. The DRM reaction

at 550-700 °C was also carried out over Al_2O_3-CeO_2 support (Figure 6a-b) as a control experiment to evaluate the potential impact of Al_2O_3-CeO_2. As shown in Figure 6B1,2, Ni-based Al_2O_3-CeO_2 catalyst depicts almost two-fold CH_4 and CO_2 conversions than the bare Al_2O_3-CeO_2 support under the same reaction conditions. During reforming of methane to syngas, CH_4 molecules are decomposed on nickel surface to reactive species CH_x (x = 0–3), whereas CO_2 molecules are chemisorbed and dissociated on metal surface or form carbonate-like species on support surface [54]. The gasification of adsorbed carbon from CH_4 fragments is thought to process on nickel surface as well as at the boundary of nickel-support. Nagaoka et al. [55] postulated that the reactivity on metal-support boundary is higher than that on metal surface. Some isolated carbon atoms, which were not gasified immediately, will diffuse either on nickel surface or through the bulk to reach the nickel-support interface. The active oxygen or carbonate from CO_2 on support will oxidize the carbon atoms to form CO. However, if the carbon atom at nickel-support interface has not been gasified immediately, the nucleation and growth of graphene layers will occur, assisted by a dynamic formation and restructuring of mono-atomic step edges at nickel-support boundary, which are considered more active sites than terrace sites in carbon nucleation [56]. Most notably, Ce/AlO_3 with the ability of capturing the CO_2 to form active surface oxygen can be oxidized to CeO_2 due to its reducibility. Furthermore, it is reported that the surface basicity of CeO_2 is higher than that of Al_2O_3 and the interaction of CeO_2 and CO_2 would yield considerable carbonate species which can react with CH_x species. Two overall reactions [57] can be rationally proposed here as: $2CeAlO_3 + CO_2 \rightarrow Al_2O_3 + 2CeO_2 + CO$ and $Al_2O_3 + 2CeO_2 + CH_x \rightarrow CO + 2CeAlO_3 + (x/2)H_2$.

The catalytic activity of Ni/Al_2O_3-CeO_2 (Figure 6c-d) was further increased significantly by doping with Mo and Mo+Pt. Both CH_4 and CO_2 conversions increased from 20 to 72% and 50 to 78%, respectively at 700 °C. Influence of Mo-doping on the CH_4 and CO_2 conversions towards syngas was also investigated and as shown in (Figure 6e-f), $Mo/Ni/Al_2O_3$-CeO_2 showed much higher CH_4 and CO_2 conversions than Ni/Al_2O_3-CeO_2 catalyst. This is an indication of the transfer of electrons from MoO_x species to Ni, leading to an increase in the electron density of metallic Ni. The subsequent addition of Mo leads to dilution of the number of Ni atoms required to generate the surface species, thereby a decline in the rate of reactive deposition of surface carbon and, consequently, the total amount of carbon deposited. In line with this dilution effect, the number of Ni crystals whose size is greater than 5 nm would also decline, thereby bringing about a diminish in the rate of formation of whisker-type carbon. Furthermore, low levels of Mo combined with small amount of Ni improves the stability of the catalyst, which forms less carbon than catalyst without molybdenum. This finding is an agreement with Borowiecki et al.[58] who observed that incorporation of small amounts of molybdenum considerably reduces the detrimental effect of carbo-deposit formation and increases the activity of methane steam reforming. Thus, the addition of a small amount of Mo seems to have a positive effect on the water gas shift reaction (WGS), favoring the formation of CO_2. It is noticed the formation of CO is higher for all Mo-doped catalysts, which inhibits accumulated carbon deposition on nearby Ni atoms and enhances the catalytic activity for non-oxidative methane dehydrogenation and DRM [59].

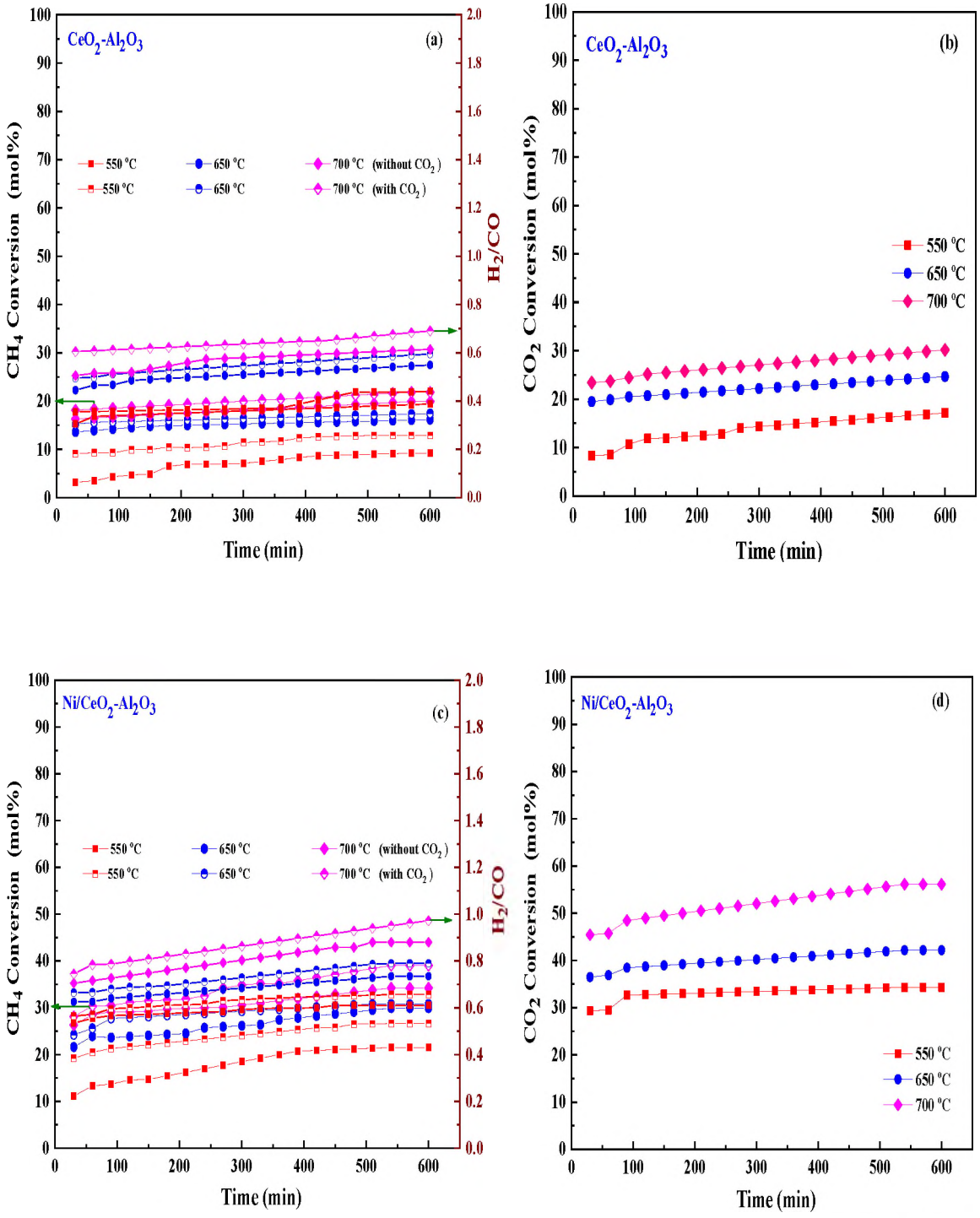

Figure 6. Catalytic performance of the (a-b) Al_2O_3-CeO_2, (c-d) Ni/Al_2O_3-CeO_2, and (e-f) Mo/Ni/Al_2O_3-CeO_2. Reaction conditions: temperature 550-700 °C, P = 1 bar; feed gas pure CH_4 and CH_4/CO_2 = 50/50, flow rate = 60 mL min^{-1}, WHSV = 12,000 mL g_{cat}^{-1} h^{-1} .

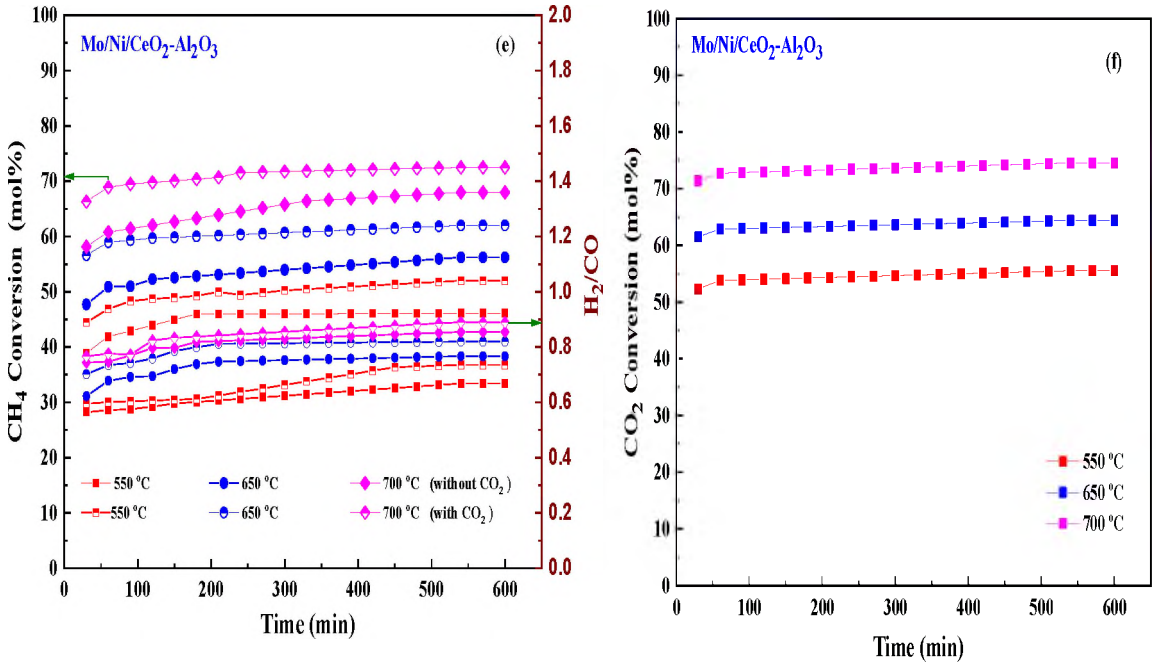

Figure 6. Catalytic performance of the (a-b) Al_2O_3-CeO_2, (c-d) Ni/Al_2O_3-CeO_2, and (e-f) Mo/Ni/Al_2O_3-CeO_2. Reaction conditions: temperature 550-700 °C, P = 1 bar; feed gas pure CH_4 and CH_4/CO_2 = 50/50, flow rate = 60 mL min^{-1}, WHSV = 12,000 mL g_{cat}^{-1} h^{-1} (cont.).

As shown in Figure 7a-b, the addition of third metal, i.e. noble metal (0.005 wt% Pt) improved the catalytic activity of the studied Ni-based Al_2O_3-CeO_2 catalysts. Pt enhances the transport of hydrogen and/or oxygen between active sites and support by spillover and thus influences on activation of methane and the mechanism of coke formation, likely by initial dissociation of methane ($CH_4 \rightarrow CH_3 + H$). The existence of Pt sites can also initiate the reduction of NiO by rapid dissociation of H_2 and then migration of atomic H towards the NiO surface by hydrogen spillover process. PtMo/Ni/Al_2O_3-CeO_2 catalyst exhibited higher selectivity towards H_2/CO molar ratio and lower carbon deposits than the Ni/Al_2O_3-CeO_2 and MoNi/Al_2O_3-CeO_2 analogues. Pervious study by Gould et al. [59] confirmed that no whiskers-type of carbon deposits were formed over Pt-Ni/Al_2O_3

which was prepared by atomic layer deposition method. Presence of Pt on the edges of Ni crystallites inhibits carbon diffusion and thus results in higher resistance toward coking. As illustrated in Table 5, these observations was confirmed by calculating the deactivation factor which are in good agreement with literature data [24]. Although a linear relationship between reactants conversion and reaction temperature was observed, the conversion of CO_2 was found to be higher than that of CH_4, indicating simultaneous occurrence of the reverse water gas shift (RWGS) reaction ($CO_2 + H_2 \rightarrow CO + H_2O$) and DRM [24]. Furthermore, the H_2/CO ratios were increased as the reaction temperature increased mainly because the RWGS reaction would gradually be prevented at elevated temperatures and completely be suppressed at around 820 ^oC due to thermodynamic effects [24].

The impact of Fe doping on the catalytic performance of Mo/Ni/Al_2O_3-CeO_2 was also examined, as illustrated in Figure 7c-d. The excellent catalytic activity and long-term catalytic stability was observed over FeMo/Ni/Al_2O_3-CeO_2 catalyst. As evident from FTIR results, Fe doping enhanced the amount of Lewis basicity, which is in favor of the chemisorption of CO_2 [24] that would accelerate the procedure: $CO_2 + C = 2CO$, thus inhabiting the carbon deposition. Consequently, we observed that Pt-doped FeMo/Ni/Al_2O_3-CeO_2 catalyst (Figure 7e-f) is more active than others under dry reforming conditions, which could be described by the Mars-van Krevelen mechanism, where Fe is oxidized partially by CO_2 to FeO, leading to partial dealloying and formation of a Ni-rich NiFe alloy. Fe migration leads to the formation of FeO preferentially at the surface where it reacts with carbon deposits via a redox mechanism to form CO, thereby the reduced Fe restores the original Ni-Fe alloy. Owing to the high activity of the material and the absence of any XRD signature of FeO, it is very likely that FeO is formed as small domains of a

few atom layer thickness covering a fraction of the surface of the Ni-rich particles, ensuring a close proximity of the carbon removal (FeO) and methane activation (Ni) sites [22]. Moreover, carbon formed on Ni particles originates mainly from the methane decomposition reaction. The FeO_x islands, that are formed under dry reforming conditions, actively participate in the reaction scheme by oxidizing the carbon deposited, through lattice oxygen, producing CO. In addition, the support provides lattice oxygen to the carbon species that have diffused towards the interface between support and active particle. Lattice oxygen which is consumed, is then regenerated by the oxidizing gas (CO_2, H_2O) producing CO. Direct interaction of CO_2 with carbon has not been previously observed [24]. Typically, the dispersion of supported metal decisive depends on oxidative pretreatment of catalyst precursor thus, resulting in high basicity of the support surface and favorable nickel-support interactions.

As shown in Table 1, a higher value of dispersion of Ni signifies a better distribution of smaller particles on the surface of the support which could assist in the reduction of carbon deposition and particles sintering, while is beneficial to the catalytic performance in terms of activity and stability. It should also be noted that H_2/CO ratio values were found to be lower than one for all catalysts, indicating the occurrence of the RWGS reaction, which converts hydrogen molecules into water ($CO_2 + H_2 \rightarrow CO + H_2O$) [9]. As evident from Table 5, the turnover frequency (TOF) values of CH_4 and CO_2 increased with reaction temperature, as expected [1,43], and that the TOF of CO_2 was higher than that of CH_4 [9].

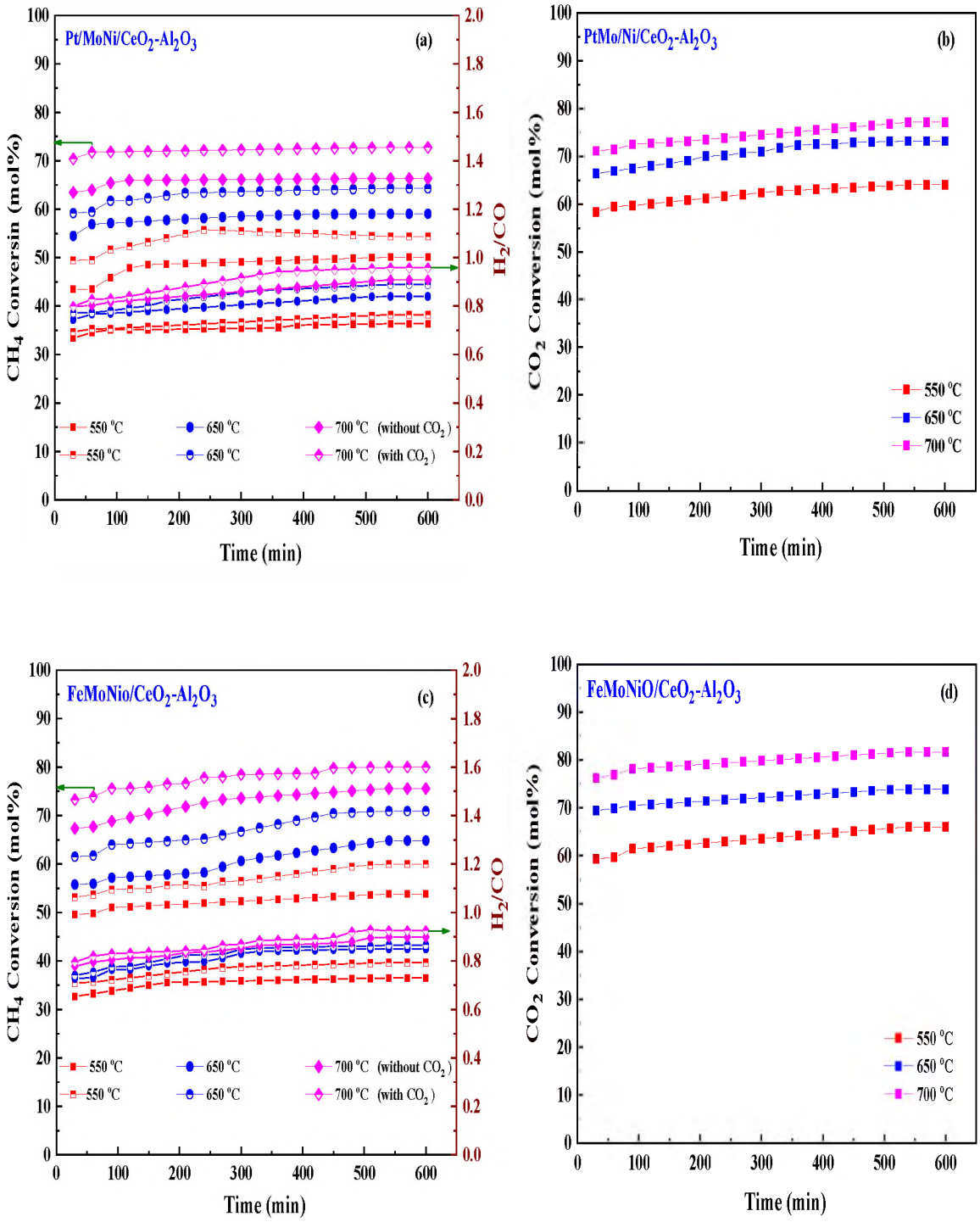

Figure 7. Catalytic performance of the (a-b) PtMo/Ni/Al_2O_3-CeO_2, (c-d) FeMo/Ni/Al_2O_3-CeO_2, and (e-f) Pt/FeMo/Ni/Al_2O_3-CeO_2. Reaction conditions: temperature 550-700 °C, P = 1 bar, feed gas pure CH_4 and CH_4/CO_2 = 50/50, flow rate = 60 mL min^{-1}, WHSV = 12,000 mL g_{cat}^{-1} h^{-1}.

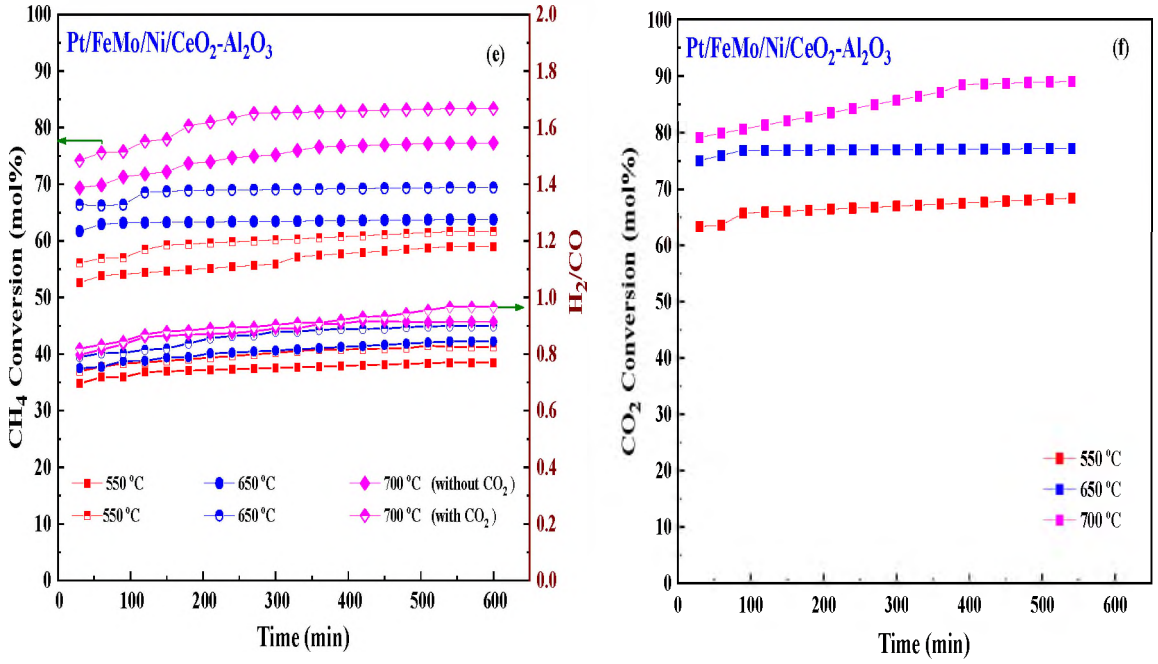

Figure 7. Catalytic performance of the (a-b) PtMo/Ni/Al_2O_3-CeO_2, (c-d) FeMo/Ni/Al_2O_3-CeO_2, and (e-f) Pt/FeMo/Ni/Al_2O_3-CeO_2. Reaction conditions: temperature 550-700 °C, P = 1 bar, feed gas pure CH_4 and CH_4/CO_2 = 50/50, flow rate = 60 mL min^{-1}, WHSV = 12,000 mL g_{cat}^{-1} h^{-1} (cont.).

It has been shown that oxygen vacancy and redox properties are crucial for improving the catalytic performance of DRM catalysts [9]. Due to the coexistence of redox pairs, the Ce or MO_x modified catalysts exhibited enhanced redox properties and abundant oxygen vacancies among the Ni-based composite catalysts. The abundant oxygen vacancies can provide supplement active oxygen and more active sites for the activation of CO_2 and CH_4. Moreover, the MO_x additives are well-dispersed in the Ni-based catalysts and lead to strong interaction between active components and Al_2O_3-CeO_2 support as, which further enhanced the vacancy oxygen contents of all catalysts compared with bare Ni/Al_2O_3-CeO_2 and Al_2O_3-CeO_2. Additionally, Ni nanoparticles could be formed and anchored in the porous framework during the reduction process and limit the sintering of

Ni species. The combination of these factors led our MO_x/Ni/Al_2O_3-CeO_2 to exhibit excellent performance in the DRM reaction. It should be noted that traces of water are produced in all reactions, implying the simultaneous occurrence of the RWGS and DRM reactions. This may explain why the conversion of CO_2 is generally higher than that of CH_4. Furthermore, the existence of Pt can initiate the NiO reduction process by rapid dissociation of H_2 and migration of atomic H to the NiO surface by hydrogen spillover phenomenon, which can retrain Ni in the metallic state under DRM conditions.

Table 5. Summary of catalytic test results for Ni-based Al_2O_3-CeO_2 composite catalysts.

Catalysts	Temperature (°C)	Conversion (mol%)		Selectivity (mol%)			DF[a] (%)	TOF_{CH4} (s^{-1})	TOF_{CO2} (s^{-1})
		CH_4	CO_2	H_2	CO	H_2/CO			
Al_2O_3-CeO_2	550	11	33	48	77	0.58	-132	1.21	1.42
	650	16	40	55	86	0.63	-99	1.49	1.55
	700	20	50	64	88	0.73	-114	1.54	1.77
Ni/Al_2O_3-CeO_2	550	24	33	48	77	0.62	-120	1.93	2.59
	650	29	40	55	86	0.64	-103	1.98	2.69
	700	34	50	64	88	0.73	-111	2.13	2.86
Mo/Ni/Al_2O_3-CeO_2	550	50	55	55	82	0.66	-72	2.28	2.68
	650	60	65	64	84	0.75	-58	2.35	2.80
	700	71	75	72	86	0.85	-46	2.69	2.95
PtMo/Ni/Al_2O_3-CeO_2	550	54	62	65	88	0.73	-60	2.53	2.79
	650	63	71	72	90	0.80	-55	2.65	2.95
	700	72	78	87	92	0.87	-42	2.81	3.18
FeMo/Ni/Al_2O_3-CeO_2	550	57	64	71	90	0.76	-59	2.71	2.81
	650	67	72	79	95	0.87	-50	2.89	3.02
	700	78	81	86	96	0.89	-40	2.93	3.23
Pt/FeMo/Ni/Al_2O_3-CeO_2	550	60	67	74	93	0.79	-54	2.82	2.97
	650	69	77	82	95	0.89	-46	2.95	3.23
	700	81	86	86	96	0.91	-37	3.17	3.53

Reaction conditions: CH_4/CO_2 =50/50, flow rate = 60 mL min^{-1}, catalyst weight = 0.3 g, P = 1bar for 10 h.

[a]Deactivation Factor (DF) = [(final CH_4 conversion - initial conversion CH_4)/initial conversion of CH_4] × 100.

4. CONCLUSION

In this investigation, a series of Ni-based Al_2O_3-CeO_2 composite catalysts were prepared and evaluated for DRM reaction. Our resulted showed that the catalytic performance of Ni/Al_2O_3-CeO_2 catalyst can be dramatically promoted by the addition of different metal particles such as Pt, Fe, and Mo. Moreover, higher metal dispersion and catalyst reducibility were noted by doping the third metal within the bimetallic Ni-based Al_2O_3-CeO_2 catalyst. Catalytic activity results revealed the impact of trimetallic promoters on Ni-based Al_2O_3-CeO_2 catalyst and the highest methane (>80%) and CO_2 (~85%) conversions and high selectivity towards H_2/CO ratio were obtained over Pt/FeMo/Ni/Al_2O_3-CeO_2 composite catalyst. This catalyst also showed the highest stability and resistance against coke deposition because of improved nickel dispersion and metal-support interactions. The good catalytic performance of Pt/FeMo/Ni/Al_2O_3-CeO_2 could be attributed to an electronic enrichment of the surface Ni atoms as a result of FeO_x/Ni and MoO_x/Ni interactions. Moreover, the reactants conversions increased with reaction temperature from 550 to 700 °C, due to the endothermic nature of the DRM reaction. The order of activity of the catalysts based on the turnover frequencies was in the order Pt/FeMo/Ni/Al_2O_3-CeO_2 > FeMo/Ni/Al_2O_3-CeO_2 > PtMo/Ni/Al_2O_3-CeO_2 > Mo/Ni/Al_2O_3-CeO_2 > Ni/Al_2O_3- CeO_2.

ACKNOWLEDGMENTS

We thank the University of Missouri Research Board (UMRB) and Materials Research Center (MRC) of Missouri S&T for financially supporting this work.

REFERENCES

[1] D. Pakhare, J. Spivey, Chem. Soc. Rev. 43 (2014) 7813–7837.

[2] W. Taifan, J. Baltrusaitis, Appl. Catal. B Environ. 198 (2016) 525–547.

[3] H. Fischer, F.; Tropscii, Brennstoff-Chemie 9 (1928) 39–46.

[4] R.E. Reitmeier, K. Atwood, H.A. Bennet, H.M. Baugh, Ind. Eng. Chem. 40 40 (1948) 620–626.

[5] A. Al-Mamoori, A. Krishnamurthy, A.A. Rownaghi, F. Rezaei, Energy Technol. 5 (2017) 834–849.

[6] and J.L.G.F. R. M. Navarro, M. A. Pen˜a, Chem. Rev. 107 (2007) 3952–3991.

[7] J.G. Seo, M.H. Youn, I. Nam, S. Hwang, J.S. Chung, K. Song, Catal Lett 130 (2009) 410–416.

[8] S.A. Theofanidis, V. V. Galvita, H. Poelman, R. Batchu, L.C. Buelens, C. Detavernier, G.B. Marin, Appl. Catal. B Environ. 239 (2018) 502–512.

[9] M.A. Atanga, F. Rezaei, A. Jawad, M. Fitch, A.A. Rownaghi, Appl. Catal. B Environ. 220 (2018) 429–445.

[10] A. Al-Mamoori, A.A. Rownaghi, F. Rezaei, ACS Sustain. Chem. Eng. 6 (2018) 13551–13561.

[11] S. Yokota, K. Okumura, M. Niwa, Appl. Catal. A Gen. 310 (2006) 122–126.

[12] S. Damyanova, B. Pawelec, K. Arishtirova, M.V.M. Huerta, J.L.G. Fierro, Appl. Catal. B Environ. J 89 (2009) 149–159.

[13] F. Magzoub, X. Li, J. Al-Darwish, F. Rezaei, A.A. Rownaghi, Appl. Catal. B Environ. 245 (2019) 486–495.

[14] L.S.F. Feio, C.E. Hori, S. Damyanova, F.B. Noronha, W.H. Cassinelli, Appl. Catal. A Gen. 316 (2007) 107–116.

[15] S. Liu, L. Guan, J. Li, N. Zhao, W. Wei, Y. Sun, Fuel 87 (2008) 2477–2481.

[16] A. Al-Mamoori, S. Lawson, A.A. Rownaghi, F. Rezaei, Energy & Fuels 33 (2019) 1404–1413.

[17] X. Li, F. Rezaei, A.A. Rownaghi, React. Chem. Eng. 3 (2018) 733–746.

[18] T. Osaki, T. Mori, J. Catal. 97 (2001) 89–97.

[19] A. Jawad, F. Rezaei, A.A. Rownaghi, J. CO2 Util. 21 (2017) 589–596.

[20] Y.Y.Y.F.Y. Yao H C, Catalysis 265 (1984) 254–265.

[21] L. Xu, H. Song, L. Chou, Appl. Catal. B Environ. 109 (2011) 177–190.

[22] S.M. Kim, P.M. Abdala, T. Margossian, D. Hosseini, L. Foppa, A. Armutlulu, W. Van Beek, A. Comas-vives, C. Cope, C. Mu, J. Am. Chem. Soc. 139 (2017) 1937−1949.

[23] S. Lawson, A.A. Rownaghi, F. Rezaei, Energy Technol. 6 (2018) 694–701.

[24] S.A. Theofanidis, V. V. Galvita, H. Poelman, G.B. Marin, ACS Catal. 5 (2015) 3028–3039.

[25] T. Huang, W. Huang, J. Huang, P. Ji, Fuel Process. Technol. 92 (2011) 1868–1875.

[26] J.B. Claridge, A.P.E. York, A.J. Brungs, C. Marquez-alvarez, J. Sloan, S.C. Tsang, M.L.H. Green, Catalysis 100 (1998) 85–100.

[27] T.G. Radosław D, ebek, Monika Motak, Maria Elena Galvezb, P. Da Costa, Appl. Catal. B Environ. J 223 (2018) 36–46.

[28] Z. Alipour, M. Rezaei, F. Meshkani, J. Ind. Eng. Chem. 20 (2014) 2858–2863.

[29] A.A. Rownaghi, Y.H. Taufiq-Yap, F. Rezaei, Catal. Letters 130 (2009) 504–516.

[30] A.A. Rownaghi, Y.H. Taufiq-Yap, F. Rezaei, Chem. Eng. J. 155 (2009) 514–522.

[31] H. Wu, G. Pantaleo, V. La, A.M. Venezia, X. Collard, C. Aprile, L.F. Liotta, "Applied Catal. B, Environ. 156–157 (2014) 350–361.

[32] X. Chen, J. Jiang, S. Tian, K. Li, Catal. Sci. Technol. 5 (2015) 860–868.

[33] T.D. Gould, A.M. Lubers, B.T. Neltner, J. V. Carrier, A.W. Weimer, J.L. Falconer, J. Will Medlin, J. Catal. 303 (2013) 9–15.

[34] C.B.A.D. K. T. JACOB, Solid State Chem. 20 (1977) 79–88.

[35] N. Rinaldi, Usman, K. Al-Dalama, T. Kubota, Y. Okamoto, Appl. Catal. A Gen. 360 (2009) 130–136.

[36] J.T. Richardson, M. Lei, B. Turk, K. Forster, V. Martyn, 110 (1994) 217–237.

[37] D. Valencia, T. Klimova, Catal. Today 166 (2011) 91–101.

[38] B.C. Miranda, R.J. Chimentão, J.B.O. Santos, F. Gispert-guirado, J. Llorca, F. Medina, F.L. Bonillo, J.E. Sueiras, "Applied Catal. B, Environ. 147 (2014) 464–480.

[39] D.E.-Q. E. Rodrı´guez-Castello´n , A. Jime´nez-Lo´pez, Fuel 87 (2008) 1195–1206.

[40] E. Kordouli, B. Pawelec, K. Bourikas, C. Kordulis, J. Luis, G. Fierro, A. Lycourghiotis, Appl. Catal. B Environ. 229 (2018) 139–154.

[41] N. Achtergracht, J. Phys. Chem. 632 (1986) 1331–1337.

[42] S. Paldey, S. Gedevanishvili, W. Zhang, F. Rasouli, Appl. Catal. B Environ. 56 (2005) 241–250.

[43] N.H. Elsayed, N.R.M. Roberts, B. Joseph, J.N. Kuhn, "Applied Catal. B, Environ. 179 (2015) 213–219.

[44] E. Rogemond, R. Fréty, V. Perrichon, M. Primet, S. Salasc, M. Chevrier, C. Gauthier, F. Mathis, J. Catal. 169 (1997) 120–131.

[45] Y.W.C. C. Li, Thermochim. Acta 256 (1995) 457–465.

[46] P. Turlier, H. Praliaud, P. Moral, G.A. Martin, J.A. Dalmon, Appl. Catal. 19 (1985) 287–300.

[47] C.R.A. J. I. Di Cosimo, V. K. D´ıez, M. Xu,† E. Iglesia, 178 (1998) 499–510.

[48] L. Yao, M.E. Galvez, C. Hu, P. Da Costa, Int. J. Hydrogen Energy 42 (2017) 23500–23507.

[49] X. Li, A. Alwakwak, F. Rezaei, A.A. Rownaghi, ACS Appl. Energy Mater. 1 (2018) 2740–2748.

[50] X. Li, W. Li, F. Rezaei, A. Rownaghi, Chem. Eng. J. 333 (2018) 545–553.

[51] J.A.O. Anna Penkova, Luis F. Bobadilla1, Francisca Romero-Sarria, Miguel A. Centeno, Appl. Surf. Sci. Jou 317 (2014) 241–251.

[52] I. Chimica, U. Roma, F.S. Stone, R.G. Turner, Solid State Chem. 11 (1974) 135–147.

[53] K.S.W. Sing, D.H. Everett, R.A.W. Haul, L. Moscou, R.S. Pierotti, J. Rouquerol, T. Siemieniewska, Pure Appl. Chem. 57 (1985) 603–619.

[54] M.C.J. Bradford, M.A. Vannice, Catal. Rev. 41 (2007) 1–42 (1999).

[55] K. Nagaoka, K. Seshan, K. Aika, J.A. Lercher, Catalysis 197 (2001) 34–42.

[56] J. Sehested, P.L. Hansen, S. Helveg, C. Lo, B.S. Clausen, J.R. Rostrup-nielsen, F. Abild-pedersen, Nature 427 (2004) 426–429.

[57] S. Wang, G.. (Max) Lu, Appl. Catal. B Environ. 19 (1998) 267–277.

[58] T. Borowiecki, A. Gotebiowski, B. Stasifiska, Appl. Catal. A Gen. 153 (1997) 141–156.

[59] T.D. Gould, M.M. Montemore, A.M. Lubers, L.D. Ellis, A.W. Weimer, J.L. Falconer, J.W. Medlin, Appl. Catal. A Gen. 492 (2015) 107–116.

III. IMPROVEMENT Ni STABILIZED ON Al_2O_3-CeO_2 CATALYSTS FOR DRY REFORMING OF METHANE: EFFECT OF Fe, Mg AND Pt DOPING

Abbas Jawad, Xin Li, Fateme Rezaei, Ali A. Rownaghi*

Department of Chemical & Biochemical Engineering, Missouri University of Science and Technology, 1101 N. State Street, Rolla, Missouri 65409, United States

ABSTRACT

Herein, the promotional effects of Fe, Mg, and Pt on Ni-based catalyst supported on Al_2O_3-CeO_2 (Ni/Al_2O_3-CeO_2) have been investigated in dry reforming of methane (DRM) reaction. To elucidate the influence of metal promoters on the performance of Ni/Al_2O_3-CeO_2 materials, the catalytic reaction was conducted in a continuous fixed-bed flow reactor at various reaction temepratures (550-700 °C), space velocity of 12,000 $ml g_{cat}^{-1}$ h^{-1} and different feedstocks (pure CH_4 or 50% CH_4/CO_2 mixture) under atmospheric pressure for 10 h time-on-stream. The co-doped Ni/Al_2O_3-CeO_2 catalysts with Mg and Fe significantly enhanced the activity (more than 80% methane and 84% CO_2 conversion), selectivity to syngas (~90%). Further, our results indicated that the addition of 0.005 wt% Pt to the Mg-Fe/Ni/Al_2O_3-CeO_2 composite catalyst leads to significant suppress coke formation, higher methane (84%) and CO_2 (89%) conversion and maintained H_2/CO ratio about 0.97 at 700 °C.

Keywords: Carbon dioxide, Dry reforming, Coke-resistant Nickel catalyst, Syngas

1. INTRODUCTION

Dry reforming of methane (DRM) with CO_2 has attracted attention because of utilization of two major greenhouse gases (CH_4 and CO_2) as feedstocks, and provides a route to convert them into the low H_2/CO ratio syngas, which can be directly used as fuel or to produce chemicals and fuels by the methanol synthesis and Fischer-Tropsch (FT) processes.[1–4] DRM is an endothermic reaction and is usually conducted at very high operation temperature (>800 °C) to ensure high methane conversion and minimize carbon deposition thermodynamically.[5,6]

The majority of the catalysts investigated for DRM are generally made up of Group VIII transition metals such as Ni due to their high activity.[4,7] Promoting nickel-based catalysts with various metals such as Mg, Fe, Zr, Cr, Ce, V, Mo, Rh, Pt, Pd and Ru is the most widely practiced approach for modifying DRM catalysts.[2–4,8–10] In particular Pt, Rh and Ru are highly active towards DRM which enhance stability against coke deposition as compared to the other non-promoted nickel-based catalysts.[11–13]

The catalyst performance has been found to be dependent on the Ni/metal ratio and the nature of the support.[7,14,15] Both promoters and support play important roles in metal electron transfer, cluster stabilization, and reducibility.[3] In particular, it has been shown that Ni catalyst is highly reducible in presence of noble metals which enables both methane combustion and reforming to occur simultaneously, thereby resulting in higher energy efficiency and improved catalytic activity.[5] Although noble metals have been found to be much more resistant to carbon deposition than other metal-based catalysts, they are generally uneconomical. On the contrary, developing bimetallic catalysts via

combining nickel with other metals is an alternative route to develop highly coke-resistant Ni-based catalysts for DRM reaction.[16] A number of studies have been dedicated to improve the Ni-based CeO_2-Al_2O_3 performance and stability through addition of second metal promoters such as Co, Pd, Pt. It has been confirmed that adding a trace of transition metals can modify Ni surface properties by promoting the reducibility of Ni and thus increasing the number of active sites to achieve better catalytic performance.[9,17] For example, several bimetallic catalysts such as Ni-Co, Ni-Pd and Ni-Pt with different supports (e.g., SiO_2, Al_2O_3, CeO_2, MgO, TiO_2, ZrO_2, HZSM-5) exhibited a much higher activity and carbon resistance for Ni-based catalyst than monometallic of Ni catalyst.[10,18,19]

Among various supports investigated, Al_2O_3 and HZSM-5 possess higher surface area which enhances the Ni particles dispersion, nevertheless, their inherent acidity and higher interaction between metal and support lead to rapid deactivation of the catalyst due to severe coke deposition. To address these issues, bimetallic supports such as Al_2O_3-La_2O_3, Al_2O_3-MgO, Al_2O_3-CeO_2 have been investigated and shown potentials for enhanced catalytic performance. [4] In particular, cerium oxide has been widely investigated by a number of researchers as promoter and support for nickel-based catalysts due to its unique redox properties (Ce^{4+}/Ce^{3+}) and remarkable oxygen storage capacities for DRM reaction.[20] Flytzani-stephanopoulos and coworkers used Al_2O_3-CeO_2 as a support and reported higher thermal stability and relatively large surface for Ni dispersion, thereby enhancing catalyst performance.[21] In another investigation, Yang et al.[22] studied Ni-Fe_2O_3/CeO_2-Al_2O_3 and Ni-CrO_3/CeO_2-Al_2O_3 catalysts for CO_2 conversion and found that CeO_2-Al_2O_3 offers an excellent support for achieving high degrees of

CO_2 conversions, whereas FeO_x and CrO_x, which are well-known active components for the forward shift reaction, have opposite effects when used as promoters. We also reported the activity and stability of Ni-based Al_2O_3-CeO_2 in the carbon dioxide dry reforming of methane.[23]

Most of the published work reports improvement in catalytic behavior, however little is known about the nature, structure and performance of Ni-M/CeO_2-Al_2O_3 catalysts where M = Fe, Fe-Mg, and Fe-Mg-Pt. The present work is aimed to improve the performance of Ni-based CeO_2-Al_2O_3 composite catalysts by synthesizing and structurally characterizing a series of monometallic Ni-M (M=Fe), bimetallic Ni-M (M=Fe-Mg and Fe-Pt) and trimetallic Ni-M (M=Fe-Mg-Pt) supported on CeO_2-Al_2O_3 to suppress coke formation and maintain the H_2/CO ration. Furthermore, the role of Pt co-promoter in the bimetallic composite catalysts was studied in DRM reaction to distinguish the catalytic effects of Pt. Among all synthesized Ni-M/CeO_2-Al_2O_3 catalysts, Pt/Fe-Mg/Ni/CeO_2-Al_2O_3 catalyst has shown the best performance, by enhancing the CH_4 and CO_2 conversion and selectivity to syngas as well as extending the catalyst life.

2. EXPERIMENTAL

2.1. CATALYST SYNTHESIS

The CeO_2-Al_2O_3 support with CeO_2 content of 50 wt% on Al_2O_3 (Sigma-Aldrich) was prepared by imregnation with $Ce(NO_3)_3.6H_2O$. The optained sample was dried overnoght at 100 °C and subsequently calcined at 550 °C for 5 h. In the next step, CeO_2-Al_2O_3 supported monometallic and bimetallic nickel-M (M = Mg, Fe) catalysts were

prepared by incipient wetness impregnation technique, dried overnight at 110 °C and then calcined in a muffle furnace (air envirmnment) at 500 °C for 4 h. A necessary amount of each metal precursor (i.e. $Ni(NO_3)_2.6H_2O$, $Fe(NO_3)_3 \cdot 9H_2O$, and $Mg(NO_3)_2.6H_2O$, from Sigma-Aldrich) was dissolved in deionized water and then mixed with the catalyst support in the adequate molar ratio. The metal loadings were set at 4 wt% nickel for Ni/CeO_2-Al_2O_3; 2 wt% nickel, 2 wt% iron for $Fe/Ni/CeO_2$-Al_2O_3; 2 wt% nickel, 2 wt% iron, and 0.5 for magnesium for Mg-$Fe/Ni/CeO_2$-Al_2O_3; 2 wt% nickel, 2 wt% iron, 0.5 for magnesium, and 0.005 wt% platinum for Pt/Mg-$Fe/Ni/CeO_2$-Al_2O_3.

2.2. CATALYST CHARACTERIZATION

X-ray diffraction (XRD) patterns of the catalysts were obtained by a diffractometer (PANalytical) operated at 30 kV and 15 mA with Cu Kα1 monochromatized radiation (λ = 0.154178 nm). XRD patterns were measured at a scan rate of 0.026°/s. N_2 physisorption isotherm measurements were carried out in Micromeritics 3Flex surface characterization analyzer at -196 °C. Textural properties such as surface area, total pore volume, micropore volume, and average pore width were determined using Brunauer-Emmett-Teller (BET), Barrett-Joyner-Halenda (BJH), and t-plot methods, respectively. Prior to the measurements, samples were degassed at 250 °C for 6 h. H_2-TPR measurements were carried out in a U-shaped quartz cell using a 5% vol H_2/He gas with flow rate of 50 cm^3/min at heating rate of 10 °C/min up to 900 °C by using Micromeritics 3Flex analyzer. Hydrogen consumption was followed by on-line mass spectroscopy (BELMass) and quantitative analysis was done by comparison of reduction signal with hydrogen consumption of a CuO reference. Temperature-programmed desorption of CO_2 (CO_2-TPD) was performed on the

same Micromeritics 3Flex analyzer. Prior to adsorption measurement, all samples were initially reduced at a temperature of 200 °C in a 5% H_2 in He gas mixture and held at the reduction temperature for 1 h, then cooled down to 50 °C under He. After the temperature was stabilized, the sample was exposed to 10% CO_2 in He for 30 min. To remove physically bound CO_2 from the surface, the flow to He (50 cm^3/min) for 30 min at 50 °C was used. The desorption of CO_2 was measured from 50 to 600 °C at a constant heating rate of 10 °C min^{-1}. To determine the nature of surface acid sites, Fourier-transform infrared spectroscopy (FTIR) of pyridine using a Bruker Tensor spectrophotometer that was employed to determine the types of acid sites present in the samples. All samples were activated at 450 °C for 4 h to release the moisture before the adsorption of pyridine and cooled down to 60 °C for pyridine adsorption until saturation. All of the measured spectra were recalculated to a "normalized" wafer of 10 mg. For quantitative characterization of acid sites, the bands at 1450 and 1550 cm^{-1} were considered to correspond to Lewis and Brønsted sites, respectively. Furthermore, inductively coupled plasma mass spectrometry (ICP-MS) analyses were used to obtain the chemical composition on surfaces and bulk before reaction.

2.3. CATALYTIC TESTS

Catalyst tests were carried out in a stainless-steel packed-bed reactor with an internal diameter of 10 mm and a length of 300 mm. The feed gas consisted of either pure CH_4 or 50% CH_4/CO_2 and its flow rate was controlled by a digital mass flow controller (MFC, Brocks Instrument) towards the reaction zones. For each run, about 3 g of the sample (particle size 0.5 μm) was diluted with sand (particle size 0.5 μm) at the ratio of 1:6

and placed in the center of the reactor by quartz wool at both ends. Prior to the reaction, the catalyst was activated *in-situ* at 500 °C in H_2 flow for 1 h. Each catalyst was evaluated within a temperature range of 550-700 °C at a constant weight hourly space velocity (WHSV) of 12,000 mL g_{cat}^{-1} h^{-1}. The reaction temperature was controlled by embedding a type-K thermocouple inside the catalyst center. The reactions were carried out isothermally for 10 h time-on-stream. The reaction products were analyzed online every 30 min with a gas chromatography (SRI 8610C) equipped with a flame ionized detector (GC-FID) and thermal conductivity detector (TCD) for H_2, CO_2, CO, H_2O and hydrocarbons. The effluent line of the reactor until GC injector was kept at 110 °C to avoid potential condensation of the hydrocarbons.

3. RESULTS AND DISCUSSION

3.1. CHARACTERIZATION OF THE CATALYST

The powder X-ray diffraction patterns for the thermally calcined Ni-based Al_2O_3-CeO_2 composite catalysts with metal additives are shown in Figure 1. The diffraction peaks observed at 2θ = 28, 33, 48 and 57° indicate the presence of cubic crystal structure of CeO_2 support.[24] In addition, it can be observed that all samples display diffraction peaks at 2θ = 38, 45, 67° which are attributed to the γ-Al_2O_3 support. Barely seen at 2θ=23.5, 35 and 60.5° that can be assigned to the NiO (006), NiO (009) and NiO (110) phases, respectively. XRD signatures of MgO, Fe_2O_3, and Pt are not observed in the Ni-based Al_2O_3-CeO_2 composite catalysts. This could be due to small amount of oxide adding and also the successful incorporation of these metals into the Ni-based Al_2O_3-CeO_2

structure.[25] Furthermore, as listed in Table 1, elemental analysis confirmed the presence of these metals. The average crystalline size of nickel was calculated by using the Debye-Scherrer equation (Table 1). The nickel crystal size was decreased upon addition of the second and third elements into Ni-based Al_2O_3-CeO_2 as a result of Ni crystal growth inhibition by these elements. The Ni crystal size was reduced from 36 to 26 and 27 nm in the presence of Pt-Fe and Pt-Fe-Mg, respectively. This phenomenon could be linked to the effects of platinum and nickel that remained on the surface of the sample and inhibited the growth of Ni crystals. This has been confirmed by ICP elemental analysis results shown in Table 1. From Table 1, the Ni, Mg, and Pt percentages were found to be very close to the theoretical values, which could be due to the incomplete precipitation of the nickel, magnesium and platinum metal precursors used during co-precipitation process.

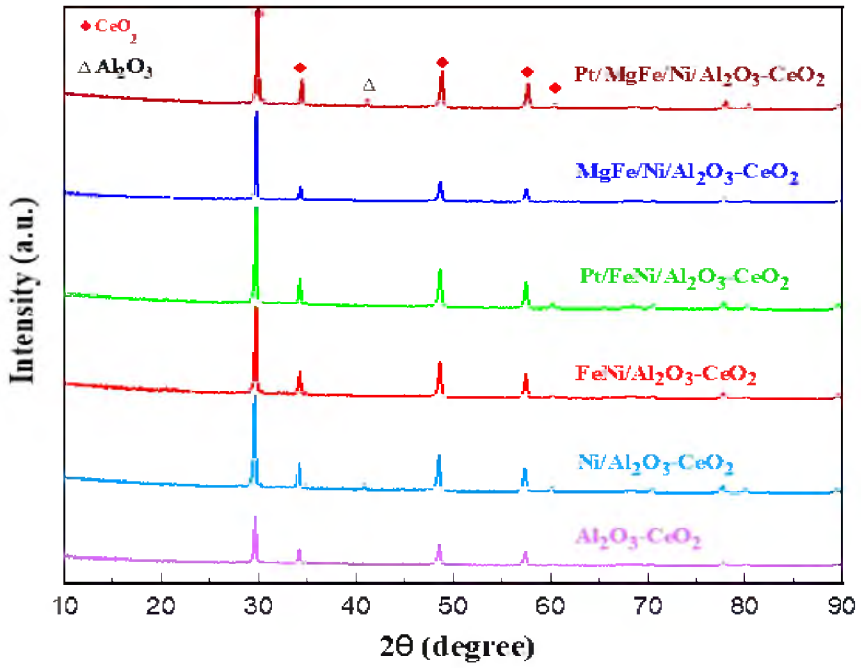

Figure 1. XRD patterns of Ni-based Al_2O_3-CeO_2 composite catalysts.

Table 1. XRD and ICP analysis Ni-based Al_2O_3-CeO_2 composite catalysts.

Catalysts	Metal loading (wt%)[a]						D (nm)[b]
	Al	Ce	Fe	Ni	Mg	Pt	
Al_2O_3-CeO_2	51.2	48.8	-	-	-	-	-
Ni/Al_2O_3-CeO_2	48.1	48.0	-	3.9	-	-	36
FeNi/Al_2O_3-CeO_2	47	46.9	2.1	4.0	-	-	32
Pt/FeNi/Al_2O_3-CeO_2	47.5	46.5	2.0	3.9	-	0.005	26
MgFeNi/Al_2O_3-CeO_2	47.0	46.8	1.9	3.8	0.5	-	33
Pt/MgFeNi/Al_2O_3-CeO_2	47.2	46.4	2.1	3.6	0.6	0.005	27

[d]Determined by ICP analysis.

[b]Estimated by Debye -Scherrer equation for Ni (200) of XRD.

H_2-TPR profiles of the reduced Ni-based Al_2O_3-CeO_2 composite catalysts showed four well-defined reduction peaks in the range 550-850 °C (Figure 2). This reduction peak corresponds to NiO incorporated within the structure of Al_2O_3-CeO_2.[26] The broad pick at 492-793 °C which is associated to the bulk reduction of Ce^{4+} to Ce^{3+}.[27] The low-temperature reduction is associated to surface Ni species which are easily reducible, while the high-temperature peaks is associated with a reduction in the NiO species that led to a strong interaction with the Al_2O_3-CeO_2 support to produce Ni.[27] The addition of Fe and Mg metals into Ni-based Al_2O_3-CeO_2 catalyst modified the reduction process and caused decay of the peak connected with unbounded NiO, whereas the observation was made for

the Fe_2O_3 doped systems. In addition to the decrease of the temperature of the ceria reduction, promoted by the presence of the Fe_2O_3, supplementary reduction of the Fe_2O_3 can be observed as previously shown by Wimmers et al.[28] studied the reduction of Fe_2O_3 and proposed a reduction in two steps $Fe_2O_3 \rightarrow Fe_3O_4 \rightarrow Fe$, with no formation of FeO. For the same oxide, other authors proposed a three-step reduction process which considered FeO formation dealing with: $Fe_2O_3 \rightarrow Fe_3O_4$ at about 400 ◦C, $Fe_3O_4 \rightarrow FeO$ at about 600 ◦C and finally $FeO \rightarrow Fe$ at higher temperatures.[29] Irrespective of the number of reduction steps of the Fe_2O_3, the separation of its reduction from that of the CeO_2 overlapping reduction zones is hard to obtain. However, the Ni-based Al_2O_3-CeO_2 catalyst without any platinum content reduced at a much higher temperature than catalysts with platinum. The addition of platinum helped further decrease the reduction temperature significantly. Therefore, the Pt/FeNi/Al_2O_3-CeO_2 and Pt/MgFe/Ni-basedAl_2O_3-CeO_2 catalysts allow reduction in the selectivity for carbon and reach values closer to equilibrium at lower reaction temperatures. Meanwhile, this implies that the platinum interaction with the support has a significant effect on increasing the reducibility of the support as well.[25,30,31] Platinum helps reduce the oxide phases through its affinity to facilitate dissociative hydrogen adsorption. Hydrogen has been identified to adsorb and dissociate on the surface of the platinum whereby it spills over to the entire surface of the support. [4,17] On the metallic surface, hydrogen molecules dissociate to hydrogen atoms, which are diffused to the $Ni^{2+}$and can react with NiO to uptake the hydrogen. Nevertheless, the rate of reduction of NiO depends not only on its chemical nature but also on nucleation process by which metallic nuclei are generated.[14] Compared with FeNi/Al_2O_3-CeO_2 and MgFeNi/Al_2O_3-CeO_2 catalysts, it can be assumed that the highly dispersed and NiO in

PtFeNi/Al_2O_3-CeO_2 and PtMgFeNi/Al_2O_3-CeO_2 could be more easily reduced by hydrogen atoms from spillover effect due to the unique interaction among Ni, and Pt species and served as metallic nuclei to facilitate reduction of Fe^{+2} and Ni^{2+}. The Al_2O_3-CeO_2 support plays a key role on the active site dispersion, activity and stability. To improve reducibility, enhance the oxygen mobility and metal dispersion, γ-Al_2O_3 material was modify by adding CeO_2 and formation of Al_2O_3-CeO_2 support. Further addition of metal oxide promoters improves reducibility and chemisorption capacity of Ni-based Al_2O_3-CeO_2 catalyst due to a better dispersion of bimetallic on the Al_2O_3-CeO_2 support.

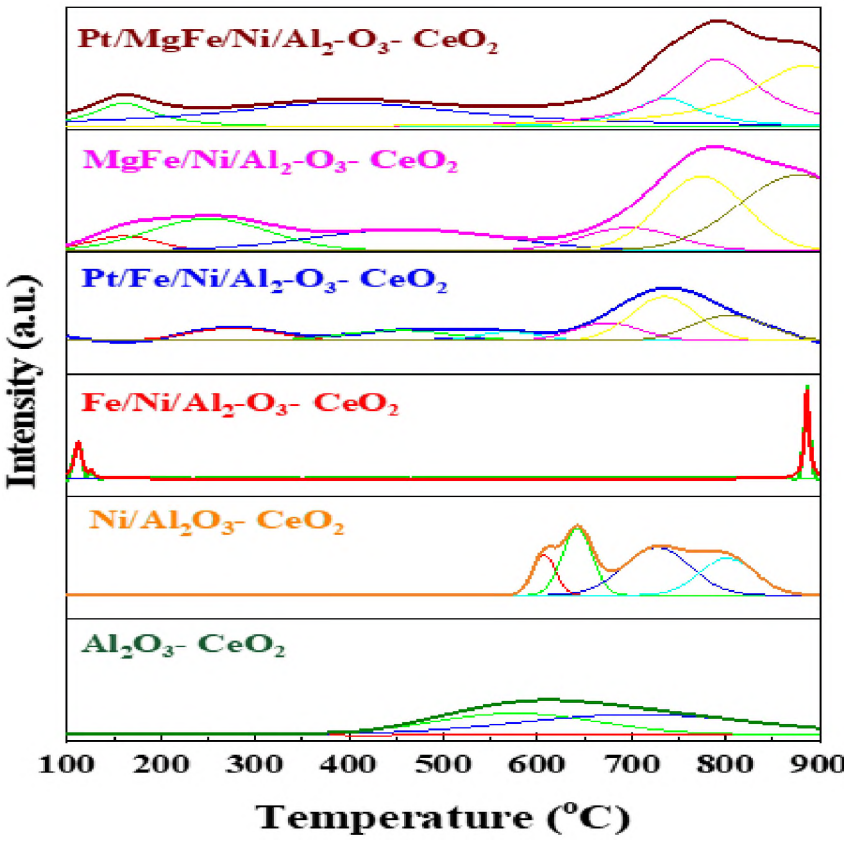

Figure 2. H_2-TPR profiles Ni-based Al_2O_3-CeO_2 composite catalysts.

The CO_2-TPD results are shown in Figure 3 and changes among weak, medium and strong basic sites are presented in Table 2. The CO_2-TPD profile of the samples shows weak basic sites between 60 and 200 °C, medium basic sites between 200 and 400 °C, and strong sites between 400 and 800 °C, respectively. The total amount of CO_2 is estimated from the integration of CO_2-TPD peak area desorbed, which obviously increases with adding of metal oxides compare to Ni-based Al_2O_3-CeO_2. Typically, it is considered that CO_2 adsorbed on weaker basic sites was desorbed at low temperature and that adsorbed on strong basic sites was desorbed at high temperature.[32,33] As a result, the CO_2 desorption peak area is improved significantly at higher temperature, indicating that the amount of adsorbed/desorbed CO_2 was increased at 550 °C, which is in the range of the reaction temperature and favorable for improving the reactivity.

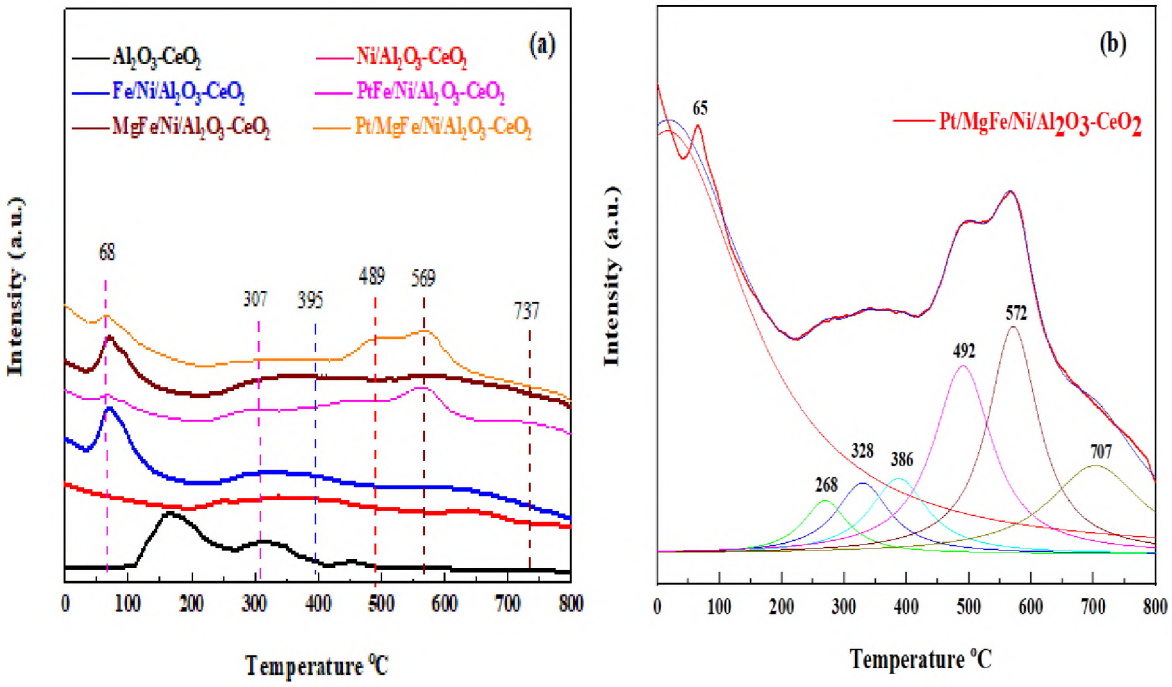

Figure 3. CO_2-TPD profiles of (a) Ni-based Al_2O_3-CeO_2; (b) the fine structure of the Pt/MgFe/Ni/Al_2O_3- CeO_2 composite catalysts.

Koo et al.[34] reported that besides weak basic sites, middle basic sites, and strong basic sites are favorable to depress the coke formation in MgO promoted Ni catalysts. In our study, the catalysts promoted with MO_x have weak, middle and strong basic sites whereas Ni-based Al_2O_3-CeO_2 catalysts have the only weak and middle basic site. Therefore, the intensity of TPD peaks becomes higher indicating the improved CO_2 adsorption capacity. The higher adsorption of acidic CO_2 over the MO_x-promoted catalysts surface confirms that these catalysts are more basic in nature compared to Ni-based Al_2O_3-CeO_2. It is well-established that the basic catalysts could improve the adsorption of CO_2 during the DRM reaction which supplies the surface oxygen to suppress the coke deposition. This finding is in agreement with previous studies.[13,34] It can be concluded that the Mg^{2+}-containing supports have an increased number of basic sites (higher amount of desorbed CO_2) with respect to the support. Notably, Mg-containing zirconias showed higher amount of basic sites compared to Ni/Al_2O_3-CeO_2. Similar results over magnesia-zirconia oxides were reported by Aramendía et al.[35] Moreover, it was observed that PtFe/Ni/Al_2O_3-CeO_2 and Pt/MgFe/Ni/Al_2O_3-CeO_2 catalysts doped with Pt show high basicity compare to Fe/Ni/Al_2O_3-CeO_2 and MgFe/Ni/Al_2O_3-CeO_2. This is attributed to increased basicity of the catalysts which in turn increases the rate of activation of mildly acidic CO_2 and hence assists in oxidation of surface carbon and increases the catalyst resistance to deactivation.[4]

Additionally, three desorption peaks centered around 395, 489, and 569 °C were also observed for all the catalysts in spite of the latter two peaks overlapping. As for the latter two overlapped desorption peaks, their strength was closely related to the addition of

the metal oxides. These three peaks mentioned above might be related to the strongly chemisorbed CO_2.

Table 2. Summary of CO_2-TPD of Ni-based Al_2O_3-CeO_2 composite catalysts.

	CO_2 desorption ($mmolg^{-1}$)[a]			
Catalysts	60–200 °C	200-400 °C	400-800 °C	Total
Al_2O_3-CeO_2	0.11	0.15	0.09	0.35
Ni/Al_2O_3-CeO_2	-	0.34	0.11	0.45
Fe/Ni/Al_2O_3-CeO_2	0.39	0.08	0.58	1.04
PtFe/Ni/Al_2O_3-CeO_2	0.03	0.26	1.25	1.54
MgFe/Ni/Al_2O_3-CeO_2	0.32	0.11	0.71	1.14
Pt/MgFe/Ni/Al_2O_3-CeO_2	0.08	0.30	2.15	2.53

[a]The amount and strong of base site were estimated from CO_2-TPD profiles.

In order to investigate these TPD profiles meticulously, Lorentz mathematical model was used to resolve the overlapped desorption peaks. For example, as shown in Figure 3b, four distinct desorption peaks centered at 65, 268, 328, 386, 492, 572, and 707 °C were observed over Pt/MgFeNi/Al_2O_3-CeO_2 catalyst. This implied that more than one type of basic centers with different intensities existed among the mesoporous framework of the Pt/MgFeNi/Al_2O_3-CeO_2 composite catalyst. Overall, the categories of the basic centers for Ni-based Al_2O_3-CeO_2 catalysts were abundant due to their own structural features as well as the promotion of the metal oxides and it is in agreement with previously reported data.[36]

The Brønsted and Lewis sites were found by *ex-situ* FTIR of pyridine adsorption using a Bruker Tensor spectrophotometer.[37,38] As shown in Figure S1 (supporting

information) absorption bands appeared at 1540-1548 cm^{-1} and 1445-1460 cm^{-1}, which were in accordance with a Brønsted (B) and a Lewis (L) acid sites, respectively.[39]

On the basis of the spectral position, the absorption at 1600 cm^{-1} can be ascribed to the interaction of pyridine with quasi-tetrahedral Al^{3+} sites, sharing a coordination vacancy with an octahedral Al^{3+} ion, and the latter band to the interaction of pyridine with purely octahedral Al^{3+} cus sites.[40] The addition of metal oxides to Al_2O_3-CeO_2 results in a decline of its Lewis acidity. In particular, if we compare the spectra obtained on Al_2O_3-CeO_2, Ni-based Al_2O_3-CeO_2 and doped Ni-based Al_2O_3-CeO_2, it is quite evident that the amount of absorbed pyridine is significantly small in both later cases. Moreover, after pyridine adsorption the band assigned to pyridine coordinated totetrahedral Al^{3+} sites located near to cation vacancy (1600 cm^{-1}) declines. This evidences incorporation of metal oxides cations in Al_2O_3-CeO_2. This finding is in good agreement with the results observed by Penkova et al.[41] Moreover, CeO_2 loading on alumina slightly affects the Lewis acidity since Ce^{n+} cations do not change the structure of the alumina. A band of pyridine coordinated to Ce^{n+} sites (1589 cm^{-1}) was also detected. The IR bands of adsorbed pyridine on the Ni-based catalysts seem to be less intense than those of the corresponding supports. This suggests an additional decrease of the Lewis acidity as a result of the incorporation of Ni^{2+}cations.[41]

N_2 physisorption isotherms of the as-prepared samples are shown in Figure 5 (supporting information), with corresponding pore size distribution shown as inset figures. All isotherms exhibited the combination of type IV isotherm with H_4 type Hysteresis loop, associated with capillary condensation, and indicated the formation of mesoporous structure in all the Ni-based Al_2O_3-CeO_2 composite catalysts. BJH method was used to

estimate the pore size distributions by using the adsorption branch. It is confirmed the formation of narrow size distribution mesopores within all metal doped Ni-based Al_2O_3-CeO_2 composite catalysts.

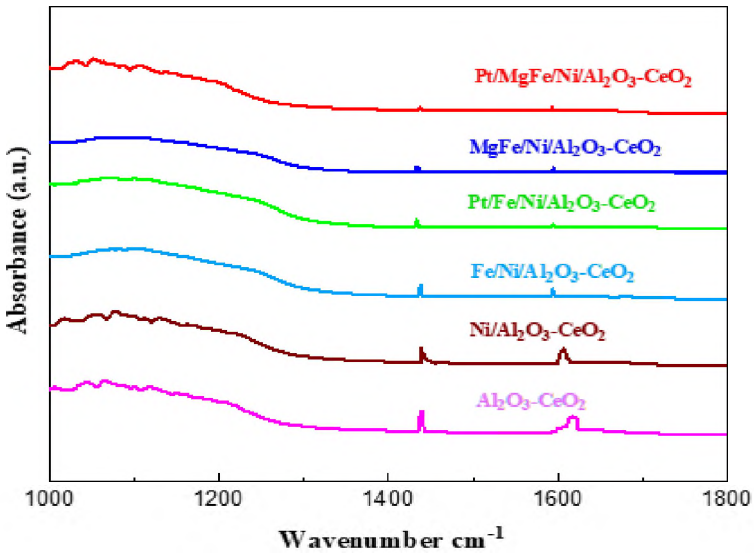

Figure 4 . FTIR spectra of Ni-based Al_2O_3-CeO_2 composite catalysts.

Table 3 summarizes the total surface area, micropore surface area, external surface area, mesopore volume pore size and diameter of Ni-based Al_2O_3-CeO_2 composite catalysts. For comparison, the Al_2O_3-CeO_2 powder was also measured. The surface areas of Al_2O_3-CeO_2, Ni/Al_2O_3-CeO_2 and Pt/MgFeNi/Al_2O_3-CeO_2 were found to be 92, 86 and 76 cm^2g^{-1} respectively, suggesting the addition of metal promoters reduced the total surface area. All the investigated metals influenced the textural properties of the Ni-based Al_2O_3-CeO_2 catalyst, but the extent was varied from metal to metal. This might result from the addition of metals physically blocking the support pores.[42] The results suggest that the

doped metals entered the pores of the Al_2O_3-CeO_2 during doping process, thereby affected the mesoporosity and pore volume of the support.

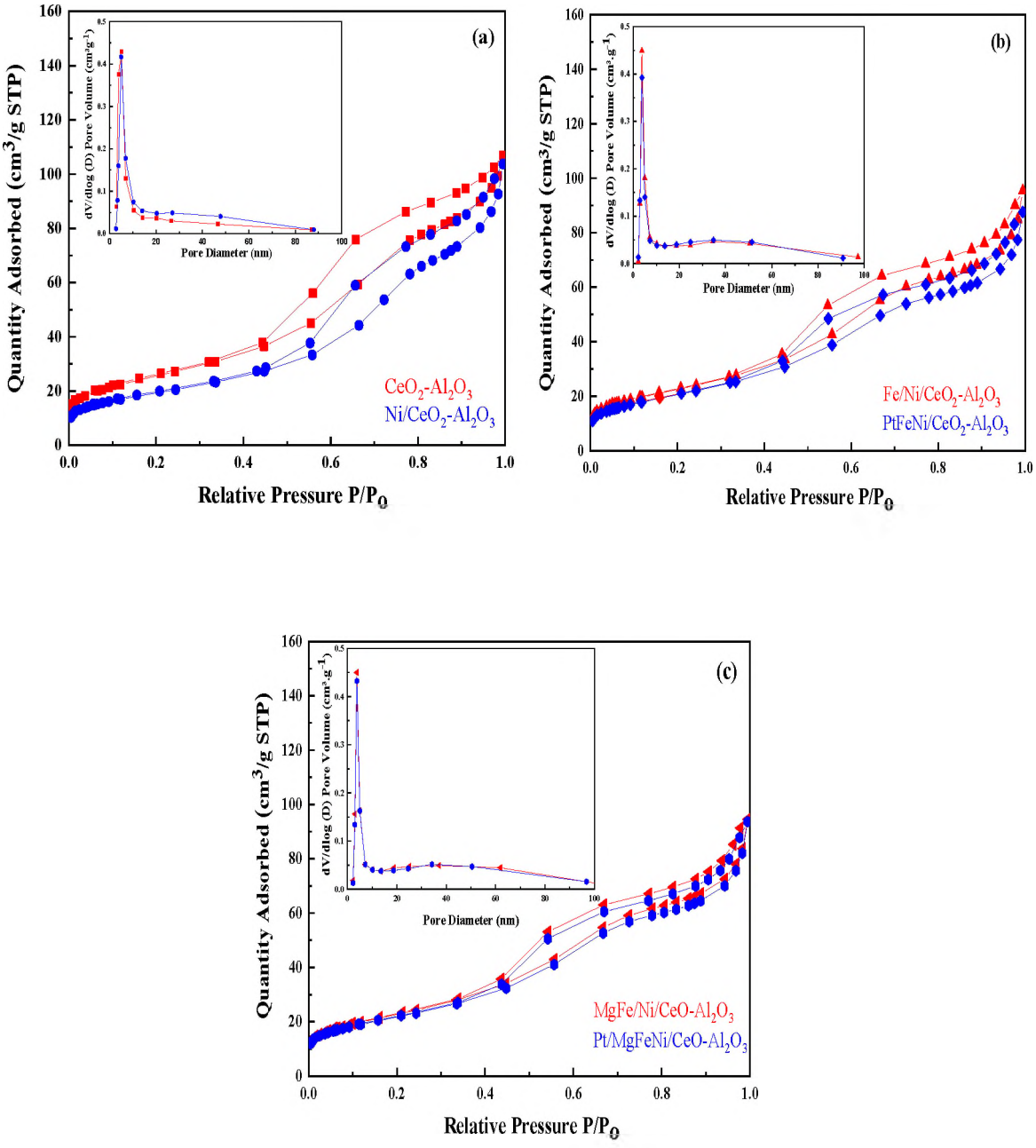

Figure 5. N_2 physisorption isotherms of Ni-based Al_2O_3-CeO_2 composite catalysts.

Table 3. Physical properties of the investigated samples obtained from nitrogen physisorption of Ni-based Al_2O_3-CeO_2 composite catalysts.

Catalysts	S_{BET} (m^2/g)[a]	S_{mico} (m^2/g)[b]	S_{meso} (m^2/g)[c]	V_{tot} (cm^3/g)[d]	Pore size (nm)[e]
Al_2O_3-CeO_2	92	3	89	0.04	5.59
Ni/Al_2O_3-CeO_2	86	3	66	0.03	5.56
Fe/Ni/Al_2O_3-CeO_2	82	1	80	0.03	5.49
PtFe/Ni/Al_2O_3-CeO_2	78	1	76	0.02	5.55
MgFe/Ni/Al_2O_3-CeO_2	80	1	82	0.03	5.48
Pt/MgFe/Ni/Al_2O_3-CeO_2	76	2	76	0.02	5.69

[a]Estimated by the Brunauer-Emmett-Teller (BET) at the p/po in the range of 0.05-0.30.
[b]Micropore area and micropore volumes were determined using the t-plot method.
[c]Estimated by BJH at the adsorbed amount at the p/po=0.99 single point.
[d]Estimated by a t-plot.
[e]Estimated by BJH desorption average pore diameter.

3.2. CATALYTIC PERFORMANCE IN DRM

Figure 6 presents catalytic results of the DRM at 550-700 °C in the presence of pure CH_4 and CH_4/CO_2 mixture (50:50). Furthermore, as shown in Figure S1 (supporting information) and Table 4, catalysts activity and stability as well as H_2/CO product ratio were measured at 550-700 °C for 600 min time-on-stream. For all catalysts, the CO_2 conversion was higher than that of CH_4 also the conversion of both CO_2 and CH_4 were enhanced with increasing reaction temperature, indicating the occurrence of side reactions such as reverse water gas shift reaction ($CO_2 + H_2 \rightarrow CO + H_2O$).[4,25] In the absence of CO_2 feeding (pure CH_4), significant amount of CO was formed over different catalysts due to decomposition of methane ($CH4 \rightarrow C + H_2$) and further oxidative regeneration ($C + O_2 \rightarrow CO_x$) process.[43] Furthermore, the H_2/CO ratios were increased as the reaction temperature increased because the RWGS reaction would gradually be prevented at

elevatied temperature.[36] The presence of CO_2 promotes CH_4 conversion (Figure 6), catalyst stability and H_2/CO ratio (Figure S3) at all reaction temperatures.

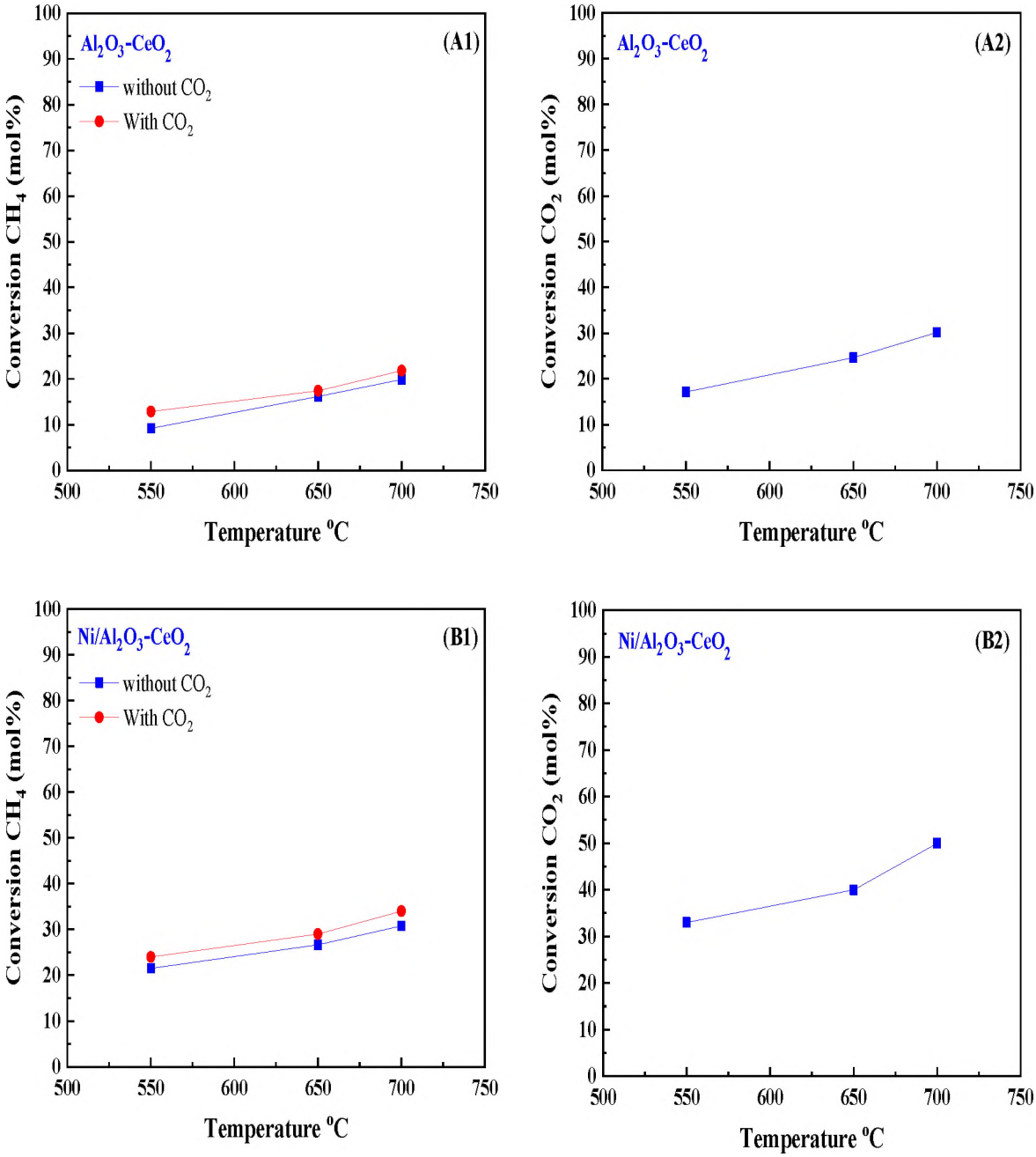

Figure 6. CH_4 and CO_2 conversion vs reaction temperature. Reaction condition ; reaction temperature 550-700 oC ; P = 1 bar; feed gas pure CH_4 (without CO_2) and CH_4/CO_2 = 50/50 (with CO_2), flow rate = 60 mL min-1, WHSV = 12,000 mL g_{cat}^{-1} h^{-1}.

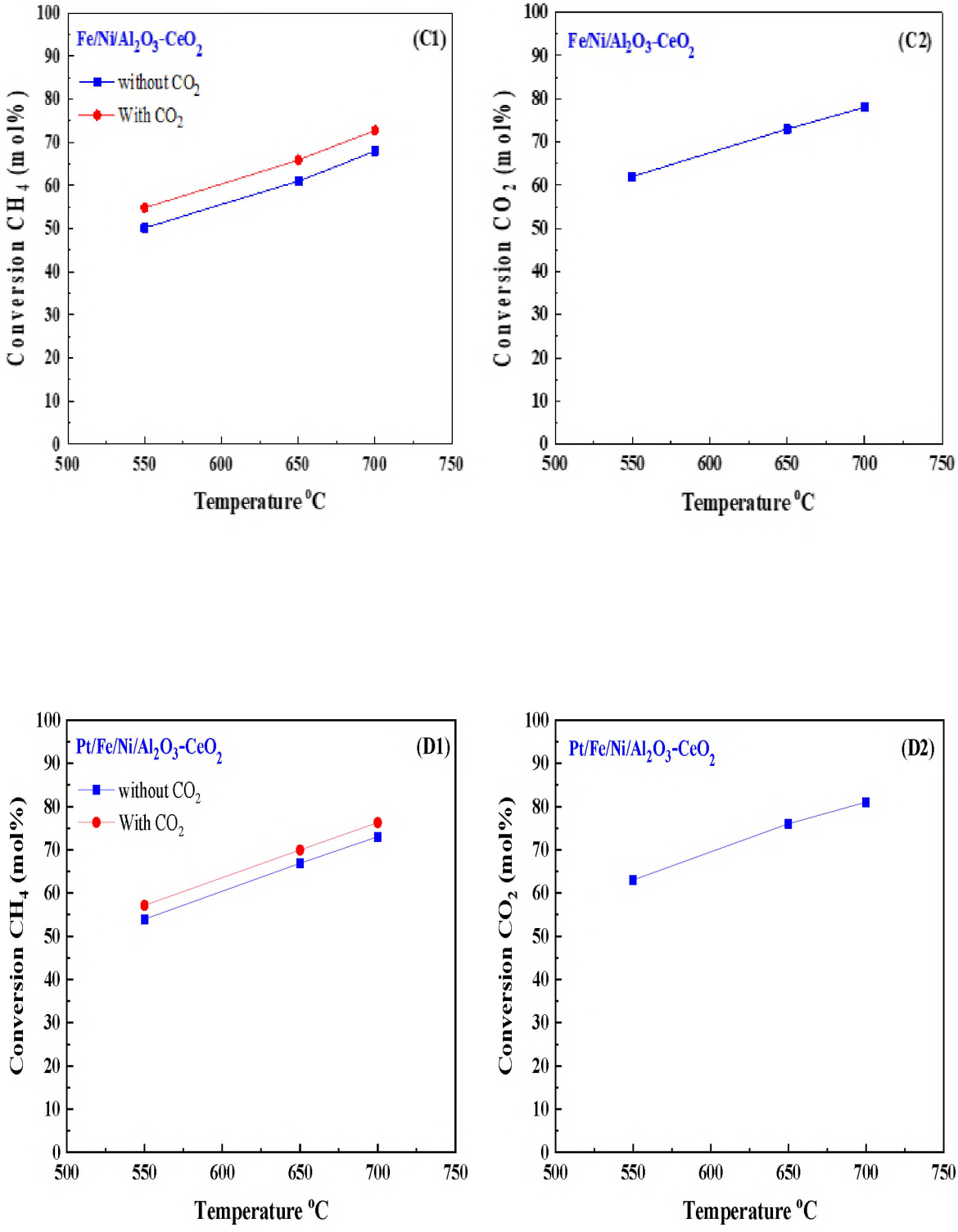

Figure 6. CH_4 and CO_2 conversion vs reaction temperature. Reaction condition ; reaction temperature 550-700 °C ; P = 1 bar; feed gas pure CH_4 (without CO_2) and CH_4/CO_2 = 50/50 (with CO_2), flow rate = 60 mL min^{-1}, WHSV = 12,000 mL g_{cat}^{-1} h^{-1} (cont.).

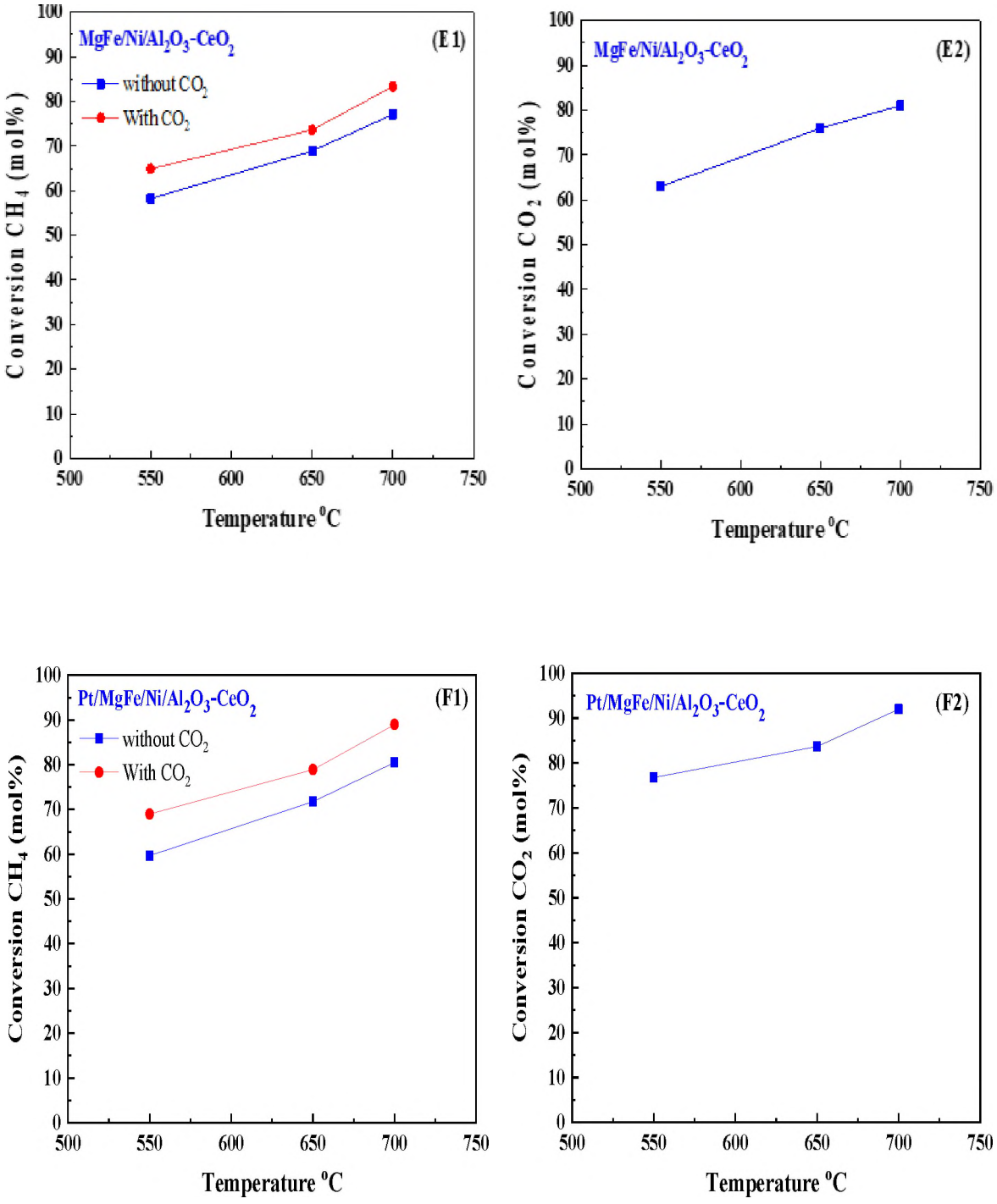

Figure 6. CH_4 and CO_2 conversion vs reaction temperature. Reaction condition ; reaction temperature 550-700 °C ; P = 1 bar; feed gas pure CH_4 (without CO_2) and CH_4/CO_2 = 50/50 (with CO_2), flow rate = 60 mL min^{-1}, WHSV = 12,000 mL g_{cat}^{-1} h^{-1} (cont.).

The DRM reaction was carried out over Al_2O_3-CeO_2 support (Figure 6A1,2) as a control experiment to evaluate the potential impact of Al_2O_3-CeO_2. The H_2/CO ratio was lower than the stoichiometric value for DRM (1 mol/mol) for Al_2O_3-CeO_2, however, it was increased by addition of Ni and other metal promoters. As shown in Figure 6B1,2, Ni-based Al_2O_3-CeO_2 catalysts exhibited almost two-fold CH_4 and CO_2 conversions than the Al_2O_3-CeO_2 support in the temperature range investigated. Both CH_4 and CO_2 conversions increased from 34 to 75 and 50 to 81, respectively at 700 °C. Previous studies have demonstrated that the high metal dispersion led to the large number of the active sites and consequently high activity.[4,25]

At all reaction temperatures, the Ni-based Al_2O_3-CeO_2 catalyst performance was further increased significantly and activity follows the trend: Pt/Mg-Fe>Mg-Fe>Pt-Fe>Fe for both CH_4 and CO_2. Doping of Fe_2O_3 into Ni-based Al_2O_3-CeO_2 catalyst results in an almost two-fold increase on the both CH_4 and CO_2 conversions (Figure 6C1 and C2). Notably, the formation of CO was found to be higher for all Fe-doped catalysts, thereby precluding the accumulated carbon deposition on nearby Ni atoms and enhancing the catalytic activity for non-oxidative methane dehydrogenation and DRM. The redox mechanism is well-definited as the Mars-van Krevelen (MvK), which consists of two reactions, the first reaction is a reduction of catalyst via hydrocarbon (methane), and the second is re-oxidization reaction of the catalyst.[4] Doping Fe/Ni/Al_2O_3-CeO_2 catalyst with 0.005 wt% Pt, further improve catalyst stability and maintained the H_2/CO ratio, probably by initial dissociation of methane ($CH_4 \rightarrow CH_3 + H$). Previous study[11–13] also confirmed that the presence of Pt sites can also initiate the reduction of NiO by rapid dissociation of H_2 and then migration of atomic H to the NiO surface by *phenomenon* of

hydrogen spillover, which produces a higher mobility of hydrogen on the support surface, facilitating the access to Ni particles. Pt/FeNi/Al_2O_3-CeO_2 catalyst showed more resistance against carbon formation than Ni/Al_2O_3-CeO_2 and FeNi/Al_2O_3-CeO_2 catalysts (Figure 6 D1,2). As noted in Table 4, these findings have been confirmed by calculating the deactivation factor and consistent with literature reports.[4] Pervious study by Pawelec et al. [44] has demonstrated that adding 0.005%Pt to the Ni catalyst leads to the generation of nanosized NiO particles, which can be readily reduced. On the basis of their findings, the authors ascribed the enhancement in the performance and coke resistance over the Pt-Ni catalysts to the increase in the nickel metallic dispersion caused by the intimate contact between nickel and platinum.

The effect of Mg doping on the catalytic performance of FeNi/Al_2O_3-CeO_2 catalyst was also examined, as illustrated in Figure 6E1,2. The excellent catalytic activity and long catalytic stability was observed over Mg/FeNi/Al_2O_3-CeO_2 catalyst. As shown in FTIR characterization, Mg doping enhanced the amount of Lewis basicity, which is in favor of the chemisorption of CO_2 that would accelerate the reaction: $CO_2 + C = 2CO$; thus inhabits the carbon deposition.[32]

Pt-doped Mg-Fe/Ni/Al_2O_3-CeO_2 catalyst has the best performance for H_2 selectivity, it is higher than the other five catalysts in the whole process, and reach 0.97 at 650 °C as shown in Figure 6 F1,2, while both Ni/Al_2O_3-CeO_2 and Al_2O_3-CeO_2 catalysts are resulted higher CO selectivity at at 550 °C. The Pt/Mg-Fe/Ni/Al_2O_3-CeO_2 shows the highest CH_4 and CO_2 conversions and H_2/CO value along all the temperatures, which indicate that the cooperative interaction between metals and support could suppress the RWGS reaction, thus Pt/Mg-Fe/Ni/Al_2O_3-CeO_2 is considered as a promising candidate for

DRM reaction in terms of activity, stability and selectivity. Furthermore, as summarized in Table 4, the highest specific activity was obtained for Pt/MgFe/Ni/Al_2O_3-CeO_2, which was followed by MgFe/Ni/Al_2O_3-CeO_2, PtFe/Ni/Al_2O_3-CeO_2, Fe/Ni/Al_2O_3-CeO_2, and Ni/Al_2O_3-CeO_2. Surface basicity, oxygen vacancy and redox property are crucial to enhance the CO_2 adsorption capacity and carbonate species formation.[45] The addition of MO_x and rare earth element (Ce_2O_3) are effectively enhance the surface basicity and redox property of the catalysts that further affect the CO_2 adsorption capacity of Al_2O_3-CeO_2 catalyst. The characterization analyses and catalytic test revealed that the introduction of MO_x species into Ni/Al_2O_3-CeO_2 catalyst generated more coordinate unsaturated Ni atoms, oxygen vacancies, defects and active sites for DRM reaction. The existence of Pt can initiate the NiO reduction process by rapid dissociation of H_2 and migration of atomic H to the NiO surface by hydrogen spillover phenomenon, which can retrain Ni in the metallic state under DRM conditions. Niu et al [25], have demonstrated that the metal with lower electronegativity, enhance CO_2 activation that has positive impact on the surface oxygen concentration and promote oxidation of the surface carbon species, thus reducing the carbon formation and improving the catalysts stability.

In order to better understand the influence of metal promoters on the activities of the Ni-M/Al_2O_3-CeO_2 catalysts for DRM, the turnover frequencies (TOFs), which reflect the intrinsic activity of the active sites, were calculated on the basis of the Ni crystallites from XRD and the initial CH_4 conversions (XCH_4) at 550-700 °C and the results are listed in Table 4. For all catalysts, TOF was improved by increasing the reaction temperature and also secondary and tertiary metal doping which were consistent with the variation of CH_4 conversions. These TOF values of CH_4 over the Pt/MgFe/Ni/Al_2O_3-CeO_2 catalysts were

found to be higher than those of mesoporous alumina-, ceria- and silica-supported Ni-based catalysts available in the literatures.[46]

Table 4. Summary of catalytic test of Ni-based Al_2O_3-CeO_2 composite catalysts.

Catalysts	Reaction Temp. (°C)	Conversion (mol%)		Selectivity (mol%)		H_2/ CO	DF (%)[a]	TOF_{CH4} (S^{-1})	TOF_{CO2} (S^{-1})
		CH_4	CO_2	H_2	CO				
Al_2O_3-CeO_2	550	13	17	48	77	0.58	-132	1.21	1.42
	650	17	25	55	86	0.63	-99	1.49	1.55
	700	22	30	64	88	0.73	-114	1.54	1.77
Ni/Al_2O_3-CeO_2	550	24	33	48	77	0.62	-120	1.93	2.64
	650	29	40	55	86	0.64	-103	1.98	2.77
	700	34	50	64	88	0.73	-111	2.13	2.92
Fe/Ni/Al_2O_3-CeO_2	550	54	62	60	86	0.70	-70	2.43	2.74
	650	65	73	71	90	0.79	-56	2.64	2.83
	700	71	78	80	91	0.87	-49	2.78	2.97
Pt/Fe/Ni/Al_2O_3-CeO_2	550	57	63	70	88	0.78	-65	2.76	2.96
	650	69	76	75	90	0.83	-52	2.98	3.28
	700	75	81	84	92	0.92	-46	3.18	3.52
MgFe/Ni/Al_2O_3-CeO_2	550	65	74	80	96	0.82	-60	2.94	3.37
	650	74	79	85	94	0.90	-43	3.10	3.58
	700	83	84	91	95	0.96	-40	3.46	3.89
Pt/MgFe/Ni/Al_2O_3-CeO_2	550	69	76	85	92	0.92	-56	3.33	3.64
	650	79	83	87	96	0.94	-42	3.63	3.96
	700	89	92	93	96	0.97	-36	3.99	4.46

[a]Deactivation Factor (DF) = [(final CH_4 conversion - initial conversion CH_4)/initial conversion of CH_4] x 100.
Reaction condition: CH_4/CO_2 =50/50, flow rate = 60 ml/min, wt. cat. = 0.3 g, P = 1bar for 10 h.

Thermal analysis (up to 800 °C) of the spent catalysts probed for the lowest mass loss for the Pt/MgFe/Ni/Al_2O_3-CeO_2 catalyst, indicating the relatively significant suppress of coke formation, and thus a better stability compared to the Ni/Al_2O_3-CeO_2 catalyst (Table 5). The highest mass loss was observed for the Al_2O_3-CeO_2 catalyst, which was showing the lowest TOF, H_2/CO ratio in DRM activity.

Table 5. Summary of weight loss of Ni-based Al_2O_3-CeO_2 composite catalysts.

Catalysts	Weight loss%	
	C^a	C^b
Al_2O_3-CeO_2	0.481	0.338
Ni/Al_2O_3-CeO_2	0.401	0.282
Fe/Ni/Al_2O_3-CeO_2	0.294	0.197
PtFe/Ni/Al_2O_3-CeO_2	0.16	0.112
MgFe/Ni/Al_2O_3-CeO_2	0.12	0.079
Pt/MgFe/Ni/Al_2O_3-CeO_2	0.093	0.039

[a] Spent catalyst in the absence of CO_2.

[b] Spent catalyst in the presence of CO_2.

4. CONCLUSION

Through impregnating Pt, Fe, and Mg doped into Ni-based Al_2O_3-CeO_2 composite catalysts was synthesized through impregnation method and evaluated for DRM reaction. All doped Ni-based Al_2O_3-CeO_2 composite catalysts presented significantly higher activity and H_2 selectivity compared to Ni-based Al_2O_3-CeO_2 composite catalysts. Although all metal-doped Ni-based Al_2O_3-CeO_2 catalysts showed slightly lower surface area than the Ni/Al_2O_3-CeO_2 catalyst and Al_2O_3-CeO_2 support, they have presented significantly higher activity and H_2 selectivity compared to Ni-based Al_2O_3-CeO_2 composite catalysts. Catalytic activity results revealed the the impact of secondary and tertiary metal doping on Ni-based Al_2O_3-CeO_2 catalyst and the highest methane (>85%) and CO_2 (~90%) conversions and high selectivity towards H_2/CO ratio (0.97) were obtained over Pt/MgFe/Ni/Al_2O_3-CeO_2 composite catalyst. The order of activity of the catalysts, based

on the turnover frequencies, was $Pt/MgFe/Ni/Al_2O_3$-CeO_2>$MgFe/Ni/Al_2O_3$-CeO_2> $PtFe/Ni/Al_2O_3$-CeO_2> $Fe/Ni/Al_2O_3$-CeO_2>Ni/Al_2O_3-CeO_2. The observed better $Pt/MgFe/Ni/Al_2O_3$-CeO_2 stability could be due to favorable changes in the distribution of surface basic sites, and better Ni dispersion.

REFERENCES

[1] P. Schwach, X. Pan, X. Bao, Direct Conversion of Methane to Value-Added Chemicals over Heterogeneous Catalysts: Challenges and Prospects, Chem. Rev. 117 (2017) 8497–8520. https://doi.org/10.1021/acs.chemrev.6b00715.

[2] A. Al-Mamoori, A. Krishnamurthy, A.A. Rownaghi, F. Rezaei, Carbon Capture and Utilization Update, Energy Technol. 5 (2017) 834–849. https://doi.org/10.1002/ente.201600747.

[3] M.A. Atanga, F. Rezaei, A. Jawad, M. Fitch, A.A. Rownaghi, Oxidative dehydrogenation of propane to propylene with carbon dioxide, Appl. Catal. B Environ. 220 (2018) 429–445. https://doi.org/10.1016/j.apcatb.2017.08.052.

[4] D. Pakhare, J. Spivey, A review of dry (CO2) reforming of methane over noble metal catalysts, Chem. Soc. Rev. 43 (2014) 7813–7837. https://doi.org/10.1039/C3CS60395D.

[5] W.J. Jang, J.O. Shim, H.M. Kim, S.Y. Yoo, H.S. Roh, A review on dry reforming of methane in aspect of catalytic properties, Catal. Today. 324 (2019) 15–26. https://doi.org/10.1016/j.cattod.2018.07.032.

[6] N.J. Gunsalus, A. Koppaka, S.H. Park, S.M. Bischof, B.G. Hashiguchi, R.A. Periana, Homogeneous Functionalization of Methane, Chem. Rev. 117 (2017) 8521–8573. https://doi.org/10.1021/acs.chemrev.6b00739.

[7] Q.L.M. Ha, U. Armbruster, C. Kreyenschulte, H. Atia, H. Lund, H.T. Vuong, S. Wohlrab, Stabilization of low nickel content catalysts with lanthanum and by citric acid assisted preparation to suppress deactivation in dry reforming of methane, Catal. Today. 334 (2019) 203–214. https://doi.org/10.1016/j.cattod.2018.11.021.

[8] S.D. Angeli, F.G. Pilitsis, A.A. Lemonidou, Methane steam reforming at low temperature: Effect of light alkanes' presence on coke formation, Catal. Today. 242 (2015) 119–128. https://doi.org/10.1016/j.cattod.2014.05.043.

[9] J. Al-Darwish, M. Senter, S. Lawson, F. Rezaei, A.A. Rownaghi, Ceria Nanostructured Catalysts for Conversion of Methanol and Carbon Dioxide to Dimethyl Carbonate, Catal. Today. (2019) 0–1. https://doi.org/10.1016/j.cattod.2019.06.013.

[10] M.A. Vasiliades, C.M. Damaskinos, K.K. Kyprianou, M. Kollia, A.M. Efstathiou, The effect of Pt on the carbon pathways in the dry reforming of methane over Ni-Pt/Ce 0.8 Pr 0.2 O 2-δ catalyst, Catal. Today. (2019) 0–1. https://doi.org/10.1016/j.cattod.2019.04.022.

[11] A.A. Rownaghi, R.L. Huhnke, Producing Hydrogen-Rich Gases by Steam Reforming of Syngas Tar over CaO/MgO/NiO Catalysts, ACS Sustain. Chem. Eng. 1 (2013) 80–86.

[12] I. Luisetto, S. Tuti, C. Battocchio, S. Lo Mastro, A. Sodo, Ni/CeO2-Al2O3 catalysts for the dry reforming of methane: The effect of CeAlO3 content and nickel crystallite size on catalytic activity and coke resistance, Appl. Catal. A Gen. 500 (2015) 12–22. https://doi.org/10.1016/j.apcata.2015.05.004.

[13] A. Al-Mamoori, A.A. Rownaghi, F. Rezaei, Combined Capture and Utilization of CO2 for Syngas Production over Dual-Function Materials, ACS Sustain. Chem. Eng. 6 (2018) 13551–13561. https://doi.org/10.1021/acssuschemeng.8b03769.

[14] C.C. Chong, S.N. Bukhari, Y.W. Cheng, H.D. Setiabudi, A.A. Jalil, C. Phalakornkule, Robust Ni/Dendritic fibrous SBA-15 (Ni/DFSBA-15) for methane dry reforming: Effect of Ni loadings, Appl. Catal. A Gen. 584 (2019). https://doi.org/10.1016/j.apcata.2019.117174.

[15] Y.H. Taufiq-Yap, Sudarno, U. Rashid, Z. Zainal, CeO2-SiO2 supported nickel catalysts for dry reforming of methane toward syngas production, Appl. Catal. A Gen. 468 (2013) 359–369. https://doi.org/10.1016/j.apcata.2013.09.020.

[16] W.Y. Kim, J.S. Jang, E.C. Ra, K.Y. Kim, E.H. Kim, J.S. Lee, Reduced perovskite LaNiO3 catalysts modified with Co and Mn for low coke formation in dry reforming of methane, Appl. Catal. A Gen. 575 (2019) 198–203. https://doi.org/10.1016/j.apcata.2019.02.029.

[17] C. Egawa, Methane dry reforming reaction on Ru(0 0 1) surfaces, J. Catal. 358 (2018) 35–42. https://doi.org/10.1016/j.jcat.2017.11.010.

[18] T.D. Gould, M.M. Montemore, A.M. Lubers, L.D. Ellis, A.W. Weimer, J.L. Falconer, J.W. Medlin, Enhanced dry reforming of methane on Ni and Ni-Pt catalysts synthesized by atomic layer deposition, Appl. Catal. A Gen. 492 (2015) 107–116. https://doi.org/10.1016/j.apcata.2014.11.037.

[19] J. Xin, H. Cui, Z. Cheng, Z. Zhou, Bimetallic Ni-Co/SBA-15 catalysts prepared by urea co-precipitation for dry reforming of methane, Appl. Catal. A Gen. 554 (2018) 95–104. https://doi.org/10.1016/j.apcata.2018.01.033.

[20] B. Yan, X. Yang, S. Yao, J. Wan, M.N.Z. Myint, E. Gomez, Z. Xie, S. Kattel, W. Xu, J.G. Chen, Dry Reforming of Ethane and Butane with CO2 over PtNi/CeO2 Bimetallic Catalysts, ACS Catal. 6 (2016) 7283–7292. https://doi.org/10.1021/acscatal.6b02176.

[21] Y. Li, Q. Fu, M. Flytzani-stephanopoulos, Low-temperature water-gas shift reaction over Cu- and Ni-loaded cerium oxide catalysts, Appl. Catal. B Environ. 27 (2000) 179–191.

[22] L. Yang, L. Pastor-pérez, S. Gu, A. Sepúlveda-escribano, T.R. Reina, Highly efficient Ni/CeO2-Al2O3 catalysts for CO2 upgrading via reverse water-gas shift: Effect of selected transition metal promoters, Appl. Catal. B Environ. 232 (2018) 464–471. https://doi.org/10.1016/j.apcatb.2018.03.091.

[23] A. Jawad, F. Rezaei, A.A. Rownaghi, Highly efficient Pt/Mo-Fe/Ni-based Al2O3-CeO2 catalysts for dry reforming of methane, Catal. Today. (2019). https://doi.org/10.1016/j.cattod.2019.06.004.

[24] T. Odedairo, J. Chen, Z. Zhu, Metal-support interface of a novel Ni-CeO2 catalyst for dry reforming of methane, Catal. Commun. 31 (2013) 25–31. https://doi.org/10.1016/j.catcom.2012.11.008.

[25] J. Niu, S.E. Liland, J. Yang, K.R. Rout, J. Ran, D. Chen, Effect of oxide additives on the hydrotalcite derived Ni catalysts for CO2 reforming of methane, Chem. Eng. J. (2019) 0–1. https://doi.org/10.1016/j.cej.2018.08.149.

[26] K. Świrk, M.E. Gálvez, M. Motak, T. Grzybek, M. Rønning, P. Da Costa, Dry reforming of methane over Zr- and Y-modified Ni/Mg/Al double-layered hydroxides, Catal. Commun. 117 (2018) 26–32. https://doi.org/10.1016/j.catcom.2018.08.024.

[27] E. Saché, L. Pastor-pérez, D. Watson, A. Sepúlveda-escribano, T.R. Reina, Ni stabilised on inorganic complex structures : superior catalysts for chemical CO2 recycling via dry reforming of methane, Appl. Catal. B Environ. 236 (2018) 458–465. https://doi.org/10.1016/j.apcatb.2018.05.051.

[28] N. Achtergracht, Determination of the Reduction Mechanism by Temperature-Programmed Reduction : Application to Small Fe203 Particles, J. Phys. Chem. 632 (1986) 1331–1337. https://doi.org/10.1021/j100398a025.

[29] S. Paldey, S. Gedevanishvili, W. Zhang, F. Rasouli, Evaluation of a spinel based pigment system as a CO oxidation catalyst, Appl. Catal. B Environ. 56 (2005) 241–250. https://doi.org/10.1016/j.apcatb.2004.09.013.

[30] T. Kobayashi, T. Furuya, H. Fujitsuka, T. Tago, Synthesis of Birdcage-type zeolite encapsulating ultrafine Pt nanoparticles and its application in dry reforming of methane, Chem. Eng. J. (2018) 0–1. https://doi.org/10.1016/j.cej.2018.10.140.

[31] A.A. Rownaghi, Y.H. Taufiq-Yap, F. Rezaei, Solvothermal synthesis of vanadium phosphate catalysts for n-butane oxidation, Chem. Eng. J. 155 (2009) 514–522. https://doi.org/10.1016/j.cej.2009.07.055.

[32] V.M. Gonzalez-delacruz, F. Ternero, R. Pere, A. Caballero, J.P. Holgado, Study of nanostructured Ni/ CeO2 catalysts prepared by combustion synthesis in dry reforming of methane, Appl. Catal. A Gen. 384 (2010) 1–9. https://doi.org/10.1016/j.apcata.2010.05.027.

[33] A.A. Rownaghi, Y.H. Taufiq-Yap, F. Rezaei, Innovative process for the synthesis of vanadyl pyrophosphate as a highly selective catalyst for n-butane oxidation, Chem. Eng. J. 165 (2010) 328–335. https://doi.org/10.1016/j.cej.2010.09.043.

[34] K.Y. Koo, H.S. Roh, U.H. Jung, D.J. Seo, Y.S. Seo, W.L. Yoon, Combined H2O and CO2 reforming of CH4over nano-sized Ni/MgO-Al2O3 catalysts for synthesis gas production for gas to liquid (GTL): Effect of Mg/Al mixed ratio on coke formation, Catal. Today. 146 (2009) 166–171. https://doi.org/10.1016/j.cattod.2009.02.002.

[35] V. García, J.J. Fernández, W. Ruíz, F. Mondragón, A. Moreno, Effect of MgO addition on the basicity of Ni/ZrO2and on its catalytic activity in carbon dioxide reforming of methane, Catal. Commun. 11 (2009) 240–246. https://doi.org/10.1016/j.catcom.2009.10.003.

[36] L. Xu, H. Song, L. Chou, Carbon dioxide reforming of methane over ordered mesoporous NiO-MgO-Al2O3 composite oxides, Appl. Catal. B Environ. 108–109 (2011) 177–190. https://doi.org/10.1016/j.apcatb.2011.08.028.

[37] X. Li, A. Alwakwak, F. Rezaei, A.A. Rownaghi, Synthesis of Cr , Cu , Ni , and Y - Doped 3D-Printed ZSM-5 Monoliths and Their Catalytic Performance for n-Hexane Cracking, ACS Appl. Energy Mater. 1 (2018) 2740–2748. https://doi.org/10.1021/acsaem.8b00412.

[38] X. Li, W. Li, F. Rezaei, A. Rownaghi, Catalytic cracking of n-hexane for producing light olefins on 3D-printed monoliths of MFI and FAU zeolites, Chem. Eng. J. 333 (2018) 545–553. https://doi.org/10.1016/j.cej.2017.10.001.

[39] F. Magzoub, X. Li, J. Al-Darwish, F. Rezaei, A.A. Rownaghi, 3D-printed ZSM-5 monoliths with metal dopants for methanol conversion in the presence and absence of carbon dioxide, Appl. Catal. B Environ. 245 (2019) 486–495. https://doi.org/10.1016/j.apcatb.2019.01.008.

[40] C. Morterra, G. Cerrato, G. Meligrana, Revisiting the use of 2,6-dimethylpyridine adsorption as a probe for the acidic properties of metal oxides, Langmuir. 17 (2001) 7053–7060. https://doi.org/10.1021/la010707e.

[41] J.A.O. Anna Penkova, Luis F. Bobadilla1, Francisca Romero-Sarria, Miguel A. Centeno, Surface Science DFT study of carbon monoxide adsorption on α -Al_2O_3 (0001)Pyridine adsorption on NiSn/MgO–Al_2O_3: An FTIR spectroscopic study of surface acidity, Appl. Surf. Sci. Jou. 317 (2014) 241–251. https://doi.org/10.1016/j.susc.2011.05.033.

[42] X. Li, F. Rezaei, A. Rownaghi, Methanol-to-olefin conversion on 3D-printed ZSM-5 monolith catalysts: Effects of metal doping, mesoporosity and acid strength, Microporous Mesoporous Mater. 276 (2019) 1–12. https://doi.org/10.1016/j.micromeso.2018.09.016.

[43] B. Gao, I. Wang, L. Ren, T. Haines, J. Hu, Catalytic Performance and Reproducibility of Ni/Al2O3 and Co/Al_2O_3 Mesoporous Aerogel Catalysts for Methane Decomposition, Ind. Eng. Chem. Res. 58 (2018) 798–807. https://doi.org/10.1021/acs.iecr.8b04223.

[44] B. Pawelec, S. Damyanova, K. Arishtirova, J.L.G. Fierro, L. Petrov, Structural and surface features of PtNi catalysts for reforming of methane with CO_2, Appl. Catal. A Gen. 323 (2007) 188–201. https://doi.org/10.1016/j.apcata.2007.02.017.

[45] H. Ren, Q. Hao, S. Ding, Y. Zhao, M. Zhu, S. Tian, Q. Ma, W. Song, Z. Miao, Z. Liu, A High-Performance NiSiO_2 Prepared by the Complexed- Impregnation Method with Citric Acid for Carbon Dioxide Reforming of Methane, Ind. Eng. Chem. Res. 57 (2018) 16257–16263. https://doi.org/10.1021/acs.iecr.8b03897.

[46] C. Chen, X. Wang, L. Zhang, X. Zou, W. Ding, X. Lu, Synthesis of mesoporous Ni–La2O3/SiO2 by ploy(ethylene glycol)-assisted sol-gel route as highly efficient catalysts for dry reforming of methane with a H2/CO ratio of unity, Catal. Commun. 94 (2017) 38–41. https://doi.org/10.1016/j.catcom.2017.02.018.

SUPPORTING INFORMATION

IMPROVEMENT Ni STABILIZED ON Al_2O_3-CeO_2 CATALYSTS FOR DRY REFORMING OF METHANE: EFFECT OF Fe, Mg and Pt DOPING

Abbas Jawad, Xin Li, Fateme Rezaei, Ali A. Rownaghi*

Department of Chemical & Biochemical Engineering, Missouri University of Science and Technology, 1101 N. State Street, Rolla, Missouri 65409, United States

Figure S1: Catalytic performance of the (A) Al_2O_3-CeO_2; (B) Ni/Al_2O_3-CeO_2; (C) FeNi/Al_2O_3-CeO_2; (D) Pt/FeNi/Al_2O_3-CeO_2; (E) Mg/FeNi/Al_2O_3-CeO_2; and (F) Pt/Mg/FeNi/Al_2O_3-CeO_2 composite catalysts.

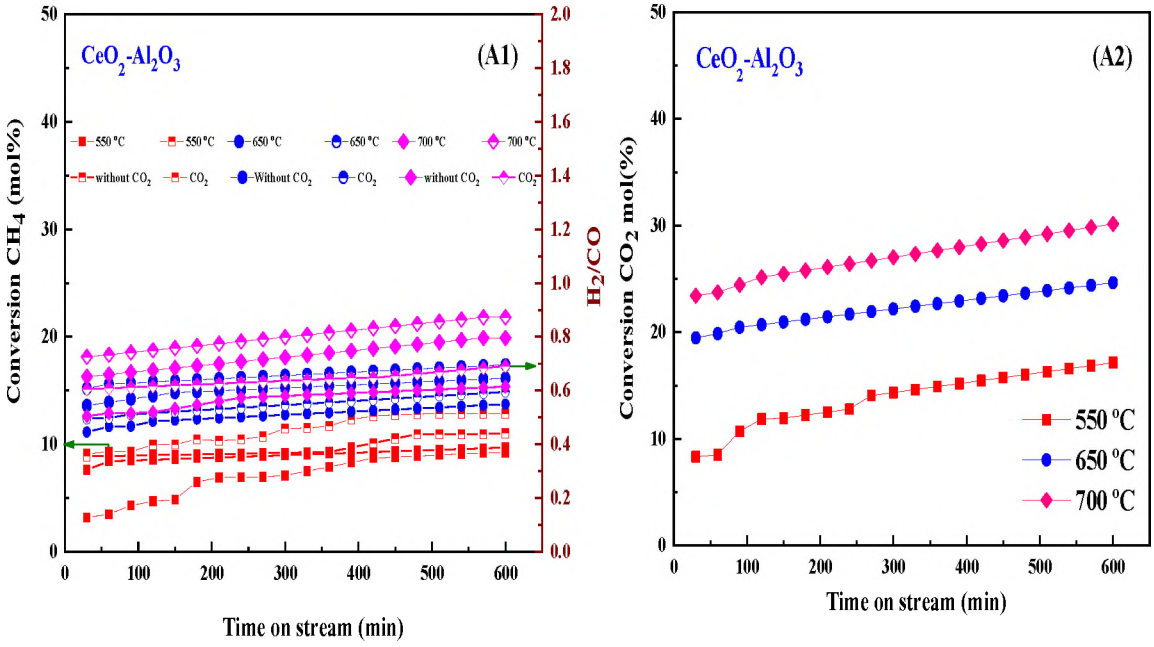

Figure S.1. Catalytic performance of the (A) Al_2O_3-CeO_2; (B) Ni/Al_2O_3-CeO_2; (C) FeNi/Al_2O_3-CeO_2; (D) Pt/FeNi/Al_2O_3-CeO_2; (E) Mg/FeNi/Al_2O_3-CeO_2; and (F) Pt/Mg/FeNi/Al_2O_3-CeO_2 composite catalysts. Reaction condition ; reaction temperature 550-700 ^oC ; P = 1 bar; feed gas pure CH_4 and CH_4/CO_2 = 50/50, flow rate = 60 mL min^{-1}, WHSV = 12,000 mL g_{cat}^{-1} h^{-1}.

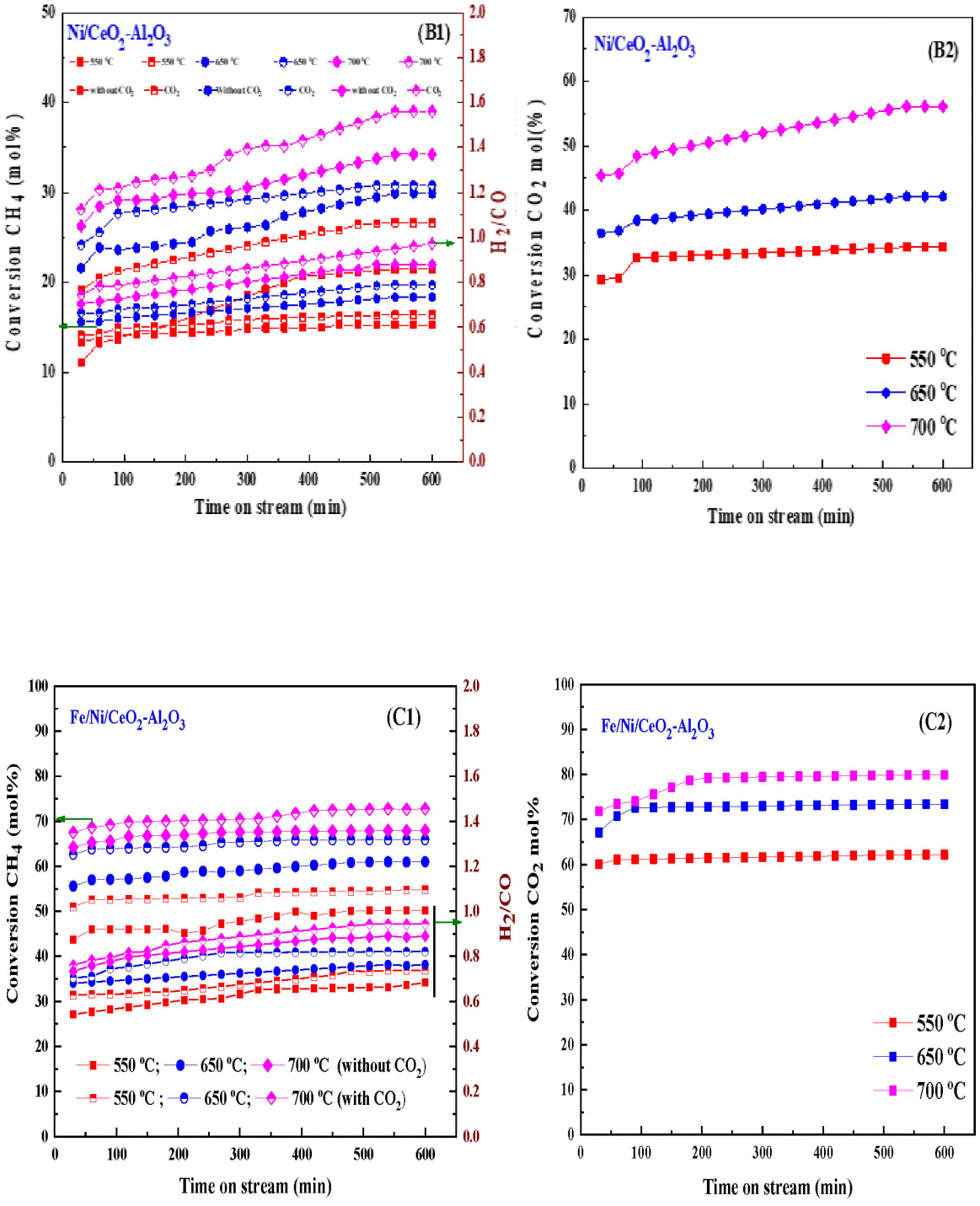

Figure S.1. Catalytic performance of the (A) Al_2O_3-CeO_2; (B) Ni/Al_2O_3-CeO_2; (C) FeNi/Al_2O_3-CeO_2; (D) Pt/FeNi/Al_2O_3-CeO_2; (E) Mg/FeNi/Al_2O_3-CeO_2; and (F) Pt/Mg/FeNi/Al_2O_3-CeO_2 composite catalysts. Reaction condition ; reaction temperature 550-700 °C ; P = 1 bar; feed gas pure CH_4 and CH_4/CO_2 = 50/50, flow rate = 60 mL min^{-1}, WHSV = 12,000 mL g_{cat}^{-1} h^{-1} (cont.).

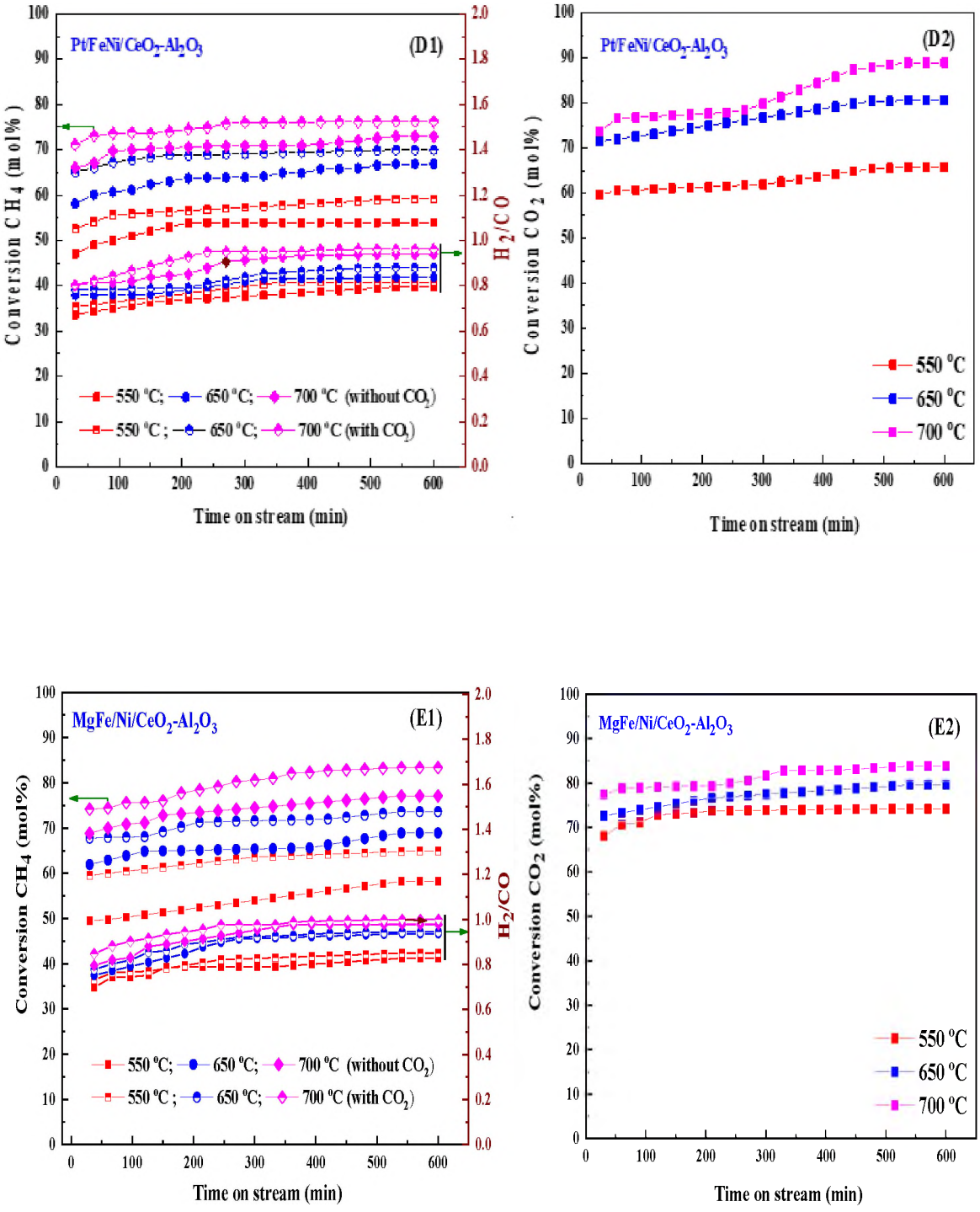

Figure S.1. Catalytic performance of the (A) Al_2O_3-CeO_2; (B) Ni/Al_2O_3-CeO_2; (C) FeNi/Al_2O_3-CeO_2; (D) Pt/FeNi/Al_2O_3-CeO_2; (E) Mg/FeNi/Al_2O_3-CeO_2; and (F) Pt/Mg/FeNi/Al_2O_3-CeO_2 composite catalysts. Reaction condition ; reaction temperature 550-700 °C ; P = 1 bar; feed gas pure CH_4 and CH_4/CO_2 = 50/50, flow rate = 60 mL min^{-1}, WHSV = 12,000 mL g_{cat}^{-1} h^{-1} (cont.).

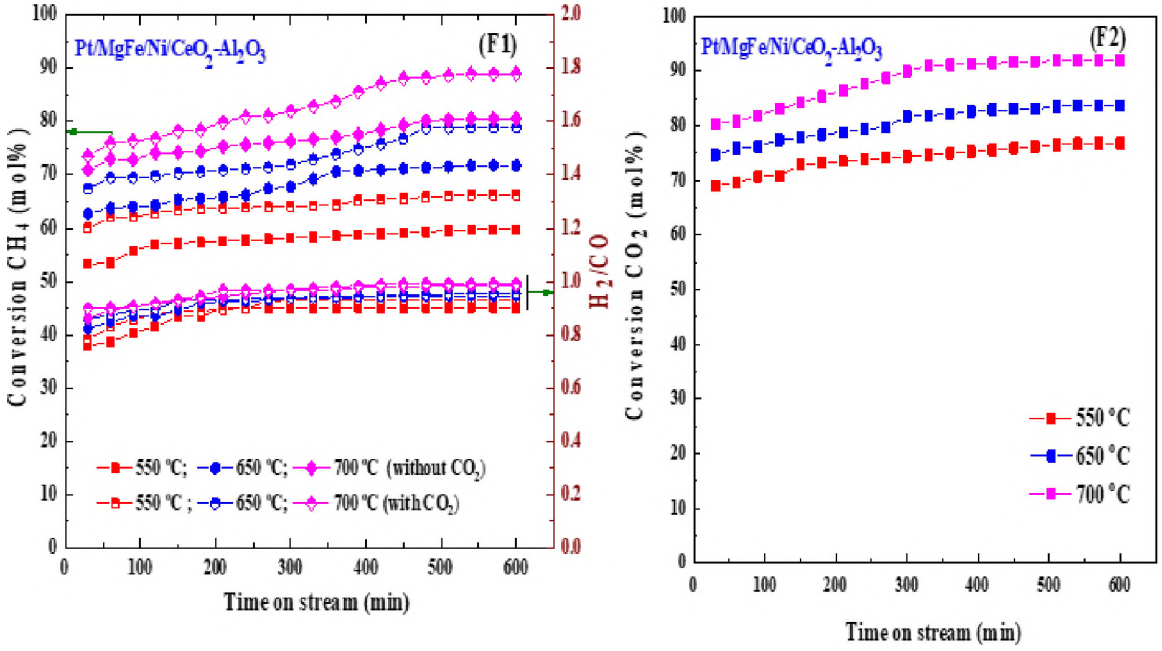

Figure S.1. Catalytic performance of the (A) Al_2O_3-CeO_2; (B) Ni/Al_2O_3-CeO_2; (C) FeNi/Al_2O_3-CeO_2; (D) Pt/FeNi/Al_2O_3-CeO_2; (E) Mg/FeNi/Al_2O_3-CeO_2; and (F) Pt/Mg/FeNi/Al_2O_3-CeO_2 composite catalysts. Reaction condition ; reaction temperature 550-700 ^oC ; P = 1 bar; feed gas pure CH_4 and CH_4/CO_2 = 50/50, flow rate = 60 mL min^{-1}, WHSV = 12,000 mL g_{cat}^{-1} h^{-1} (cont.).

IV. OXIDATIVE DEHYDROGENATION OF PROPANE OVER (Ga−, V−, Cr−) DOPED H-ZSM-5 IN PRESENCE AND ABSENCE CO_2

Abbas Jawad, Fateme Rezaei, Ali A. Rownaghi*

Department of Chemical & Biochemical Engineering, Missouri University of Science and Technology, 1101 N. State Street, Rolla, Missouri 65409, United States

ABSTRACT

A systematic study of the comparative performances of 4 wt% Ga, 4%V and 1 wt% Cr impregnated H-ZSM-5 catalysts have been tested for the dehydrogenation of propane to propene in the presence and absence of carbon dioxide. Several techniques including X-ray diffraction, NH_3-temperature-programmed desorption, H_2-temperature-programmed reduction and N_2 physisorption were applied to characterize the physicochemical properties of the as-synthesized materials. Catalytic tests showed that all In-containing samples were active in the CO_2-promoted dehydrogenation of propane with good propene selectivity. Among the metal dopants -H-ZSM-5 catalysts tested, the Cr/V-Ga/H-ZSM-5 catalyst showed the highest dehydrogenation activity with superior long-term stability. The specific interaction between metal dopants leading to a high component dispersion is suggested to play a crucial role in regulating the redox and structural properties of catalyst surface, which makes the Cr/V-Ga/H-ZSM-5 composite highly active and stable for the reaction.

Keywords: dehydrogenation of propane; Cr/V-Ga/H-ZSM-5; redox property.

1. INTRODUCTION

The process of catalytic dehydrogenation of propane into propene is of increasing interest due to the growing demand for propene, an important raw material for producing propene, polyacrylonitrile, acrolein and acrylic acid.[1] The two main commercial processes (steam cracking of naphtha or liquid petroleum gas, and fluid catalytic cracking, FCC, of heavier oil fractions) have already reached their optima for propene production.[2] The catalytic dehydrogenation of alkanes is of the considerable industrial importance, for it represents a route that economically upgrades low-cost saturated hydrocarbons into the more expensive alkene.[3] In this context, selective dehydrogenation of propane to propene is one of the major challenges for producing precious feedstocks. An alternative route that has received attention recently is the dehydrogenation (DH) of propane, which operates at high temperatures (above 527 ^{o}C) in order to circumvent inherent drawbacks: thermodynamic limitations for propane conversion, high energy requirements due to endothermic reaction and limited catalytic stability owing to coke formation, leading to decreased propene selectivity and yield.[4] As an alternative to DH, oxidative dehydrogenation (ODH) of propane by molecular oxygen offers the possibility of being an energy-saving process for propene production.[5] Nevertheless, this process suffers from a significant loss of propene selectivity due to the overoxidation of propane to carbon dioxide in the reaction and has several safety issues.

Recently, the use of CO_2 as a mild/soft oxidant to activate the short chain alkanes has emerged as new promising technology for the development of safer, more economical and environmentally friendly propane dehydrogenation process.[6] It has been shown that

in this new process propene can be obtained with a higher yield than in the commercial one. The promotion effect of the presence of CO_2 in the reaction stream has been attributed to an increase of the dehydrogenation efficiency via a direct surface redox mechanism in which the catalyst undergoes reduction (by propane) and re-oxidation (by CO_2) cycles [7] or a more complex reaction pathway involving a simple dehydrogenation followed by the reverse water gas shift (RWGS) reaction.[8]

In the latter case CO_2 removes hydrogen from the reaction system and releases the thermodynamic restrictions. It has been demonstrated that in many catalyst systems propene formations is promoted by both presented mechanisms.[9] Moreover, in the dehydrogenation process CO_2 can act as a diluent[10], it delivers the required heat and reduces coking of catalyst by the coke gasification. Among all the tested catalysts, the supported gallium oxide-based materials have been documented as the most promising ones due to their high catalytic efficiency.[11] One critical limitation associated with the conventional Ga_2O_3-catalyzed propane DH process, however, is the drastic deactivation during a few hours on-stream.[10]

ODH reactions on supported VO_x catalysts including redox cycles and kinetically relevant C-H bond activation steps that require electron transfer from O to V within VO_x domains. Chen et al.[12] displayed that ODH turnover rates augment with declining VO_x UV-visible absorption edge energies and with increasing reducibility of VO_x domains in H_2. ODH turnover rates increased as polyvanadates became the predominant VO_x species, suggesting that linkages between monovanadate structures and support cations decline the reactivity and reducibility of V-oxo species. These data also suggested that an intervening layer of a more reducible oxide (MO_x) may minimize these support effects by replacing V-

O support linkages with more reactive V-O-M linkages. Recently zirconia, usually used as a ceramic material, is also attracting attention. It can be used either as a support[12] or as an active material.[13] The important properties that favor zirconia over the conventional supports include strong interaction with the active metal phase resulting in higher dispersion as well as higher thermal and chemical stability. It is reported to be stable even under reducing conditions.[14] Zirconia is the only metal oxide possessing all the four chemical properties important for catalysis: acidity, basicity, reducing ability and oxidizing ability. These unique features of zirconia make it suitable as catalytic material for many reactions. Currently, it is widely used either as a single support or mixed support for vanadia catalysts in various reactions. Notably, Cr-containing catalysts have been widely used for the oxidative dehydrogenation of alkanes[6], which uses an RWGS process to eliminate the hydrogen generated from alkanes with CO_2. In these processes, Cr species can effectively promote the elimination of hydrogen dissociated from the C-H bonds of the alkane with CO_2 by means of the RWGS, promoting the generation of alkenes. Coke deposition can also be alleviated by carbon elimination with CO_2.

Zeolites are microporous aluminosilicate minerals that have a porous structure to host a wide variety of cations, such as H^+, Na^+, K^+, and Mg^{2+}. The most majority features of zeolite materials are the appropriate Brønsted/Lewis acid ratio, dual meso-/microporosity and excellent mass-transfer ability, which make them good candidates for a wide number of applications including catalysis, adsorption and separation.[15] The acidity of zeolite depends on the atomic ratio of Si/Al. The amount of Al atoms is proportional to the amount of Brønsted acid sites; the higher the ratio of Al/Si, the higher the acidity of the catalyst. In continuation of our interest in exploring the applications of

ZSM-5-supported oxide catalysts in oxidative dehydrogenation of propane in the presence of carbon dioxide (ODPC).[16] Transition metal containing zeolites are of special interest due to their Lewis acidity. For example, chromium and gallium oxide, which are the most active, selective and stable in the process with CO_2. It is well known that Ga-loaded ZSM-5 is a good catalyst for aromatization of ethane and propane. The process is regarded as a bifunctional mechanism, in which gallium oxide is responsible for catalyzing the dehydrogenation of propane while Brønsted acid sites account for catalyzing the oligomerization of the olefins thus produced and their subsequent aromatization. The high propene yield and superior stability were ascribed to the decrease in the number of acid sites with medium to strong strength on the catalysts, which results in the suppression of the side reactions such as oligomerization, cyclization, cracking and aromatization. Furthermore, it has been observed that the over the latter mentioned catalysts positive effect exerted by CO_2.[17] In the present work, evaluation was made of catalytic performance in the presence and absence of CO_2, using metal dopants (Cr, V, and Ga)/H-ZSM-5 catalysts obtained by impregnation method. The obtained materials, with an identical well-ordered pore structure and large surface area, were characterized physicochemically and tested as catalysts in the oxidative dehydrogenation of propane (ODP) process. The effects of the Cr/, V/, and Ga/ on the structure and adsorption properties were systematically conducted. In particular, the role of surface components on the optimum composition was investigated. According to the results, this study confirms that there is a synergetic effect existed in di/or multi-metal-oxide systems in detail of the physicochemical characterization, which greatly change the adsorption properties of two reactants (C_3H_8 and CO_2) during for oxidative dehydrogenation of propane in presence and absence of CO_2.

2. EXPERIMENTAL

2.1. CATALYST SYNTHESIS

The pristine MFI zeolite powder was the commercial ZSM-5 (CBV 8014, Zeolyst International, nominal Si/Al ratio =50, NH_4-form) was converted to the protonic form by calcination at 550 °C for 6 h in static air (ramp rate = 10 °C/min). The transition metal oxide precursors including $Ga(NO_3)_3.xH_2O$, $Cr(NO_3)_3 \cdot 9H_2O$, and vanadium (V) oxide (V_2O_5) ,were all purchased from Sigma-Aldrich. Cation introduction (Ga, V, and Cr) was achieved by wet impregnation in stirred aqueous solutions of the corresponding nitrates (99% Sigma Aldrich) and then dried overnight at 120 °C . Subsequcent, the samples were calcined in a muffle furnace at 550 °C for 6 h (ramp rate = 10 °C/min). The metal loadings were set at 4 wt% Ga for Ga/H-ZSM-5;and 4wt% V, and 4 wt% Ga for V-Ga/H-ZSM-5; and 1 wt% Cr ,4wt% V, and 4 wt% Ga for Cr/V-Ga/H-ZSM-5.

2.2. CTALALYST CHARACTERIZATION

X-ray diffraction (XRD) patterns of the catalysts were obtained by a diffractometer (PANalytical) operated at 30 kV and 15 mA with Cu Kα1 monochromatized radiation (λ = 0.154178 nm). XRD patterns were measured at a scan rate of 0.026°/s. N_2 physisorption isotherm measurements were carried out in Micromeritics 3Flex surface characterization analyzer at -196 °C. Textural properties such as surface area, total pore volume, micropore volume, and average pore width were determined using Brunauer-Emmett-Teller (BET), Barrett-Joyner-Halenda (BJH), and t-plot methods, respectively. The strength and concentration of total acid sites of catalysts were determined by NH_3 temperature-

programmed desorption (NH_3-TPD) using a Micromeritics 3Flex analyzer. Typically, 100 mg of powder sample was placed in a U-shaped fixed-bed reactor, preheated at 530 °C for 1 h, and cooled to 100 °C. Then NH_3 gas was injected to saturate the sample, followed by introduction of a He carrier gas to purge the excess NH_3 . After stabilization for 1 h, the sample was heated to 600 °C at a ramping rate of 10 °C/min. The desorption profile of NH_3 in the temperature range of 100−600 °C was followed by on-line mass spectroscopy (MKS). The NH_3 -TPD profiles were deconvoluted by peak-fitting to quantify the numbers of acid sites at different temperatures. H_2-TPR measurements were carried out in a U-shaped quartz cell using a 5% vol H_2/He gas with flow rate of 30 cm^3/min at heating rate of 10 °C/min up to 800 °C by using Micromeritics 3Flex analyzer. Hydrogen consumption was followed by on-line mass spectroscopy (MKS) and quantitative analysis was done by comparison of reduction signal with hydrogen consumption of a CuO reference.

2.3. CATALYST EVALUTION

To measure catalytic activity of the system towards selective to propene, the catalyst tests would carried out in a stainless-steel packed-bed reactor with an internal diameter of 12.7 mm and a length of 300 mm. The feed gas consisted of either C_3H_8/N_2 = 2.5/97.5% or $C_3H_8/CO_2/N_2$ = 2.5/5/92.5% was introduced with a flow rate of 75 mL/min and its flow rate was controlled by a digital mass flow controller (MFC, Brocks Instrument) towards the reaction zones. Nitrogen was used as an internal standard to account for the changes of ethane flow rate due to the reaction. In a typical run, 300 g of catalyst (particle size 0.5 μm) was diluted with sand (particle size 0.5 μm) at the ratio of 1:4 and placed in the center of the reactor by quartz wool at both ends.the test was evaluated within a

temperature range of 400-550 °C at a constant weight hourly space velocity (WHSV), 4 Kg_{cat} s mol^{-1}_{C3H8}. Prior to the reaction, the catalyst was activated *in-situ* at 600 °C in nitrogen (N_2) flow for 1 h. Next, the sample was reduced at 600 °C for1 h by 5% H_2/He. After purging with N_2 for 5 min, 75 mL/min of 10% CO_2/Ar was introduced to re-oxidize the catalyst and a catalytic test was conducted. The reaction temperature was controlled by embedding a type-K thermocouple inside the catalyst center. The reactions were carried out isothermally for 10 h time-on-stream. The reaction products will analyzed online every 30 min with a gas chromatography (SRI 8610C) equipped with a flame ionized detector (GC-FID) connected to capillary column to detect propene and by-products. The effluent line of the reactor until GC injector will kept at 110 °C to avoid potential condensation of the hydrocarbon.

3. RESULTS AND DISCUSSION

3.1. CHARACTERIZATION OF THE CATALYST

The XRD patterns of the as-synthesized metal doped H-ZSM-5 catalysts are displayed in Figure 1. Characteristic peaks observed at $2\theta = 7.89°$, 8.83°, 23.1°,23.43°, and 24.0° were attributed to (101), (200), (501), (341), and (303) planes of the zeolite crystal with MFI framework. The patterns indicate that the crystal phase of H-ZSM-5 does not destroyed during the process of metal loading and calcination. However, the intensity of characteristic H-ZSM-5 peak in metal doped-H-ZSM-5 catalyst decreases. According to the literature[18], the metal oxide species loaded on H-ZSM-5 could enhance the zeolites' absorption of X-ray, causing the decrease in the intensity of characteristic H-ZSM-5 peaks.

Additionally, this reduction in crystallization occurs with the decrease in the micropores and all pores of the catalyst to ZSM-5; and alters the ratio of Si / Al to the framework of zeolite . No obvious diffraction peaks were found within the investigated angles corresponding to gallium, vanadium, and/or chromium species are observed in the XRD patterns, indicating that dopant species may be well dispersed on the surface of ZSM-5 zeolite [20] or aggregated into mini-crystals that are too small less than 4 nm, which made them difficult to detect by XRD.[21] Furthermore, the low metal loading in the samples together with either a location of the cations at ion exchange positions or a possible overlap with the diffraction peaks of the parent H-ZSM-5 zeolite cannot be ruled out. It is generally accepted that the small angle X-ray diffraction (SAXRD) patterns as shown in Figure 1b of microporous materials are very sensitive to the presence of any particle inside their micropore channel structures, where the intensity and the d-spacing of the diffraction peak changes accordingly.[22] Moreover, the height of the diffraction lines of the mesoporous samples is slightly lowered and broaden, which is due to the presence of nanometer-sized crystals based on the Scherrer equation.[23] The intensity of the low angle diffraction peaks between $2\theta = 7–10°$ was significantly lower with metal dopants (V, and Cr) compared to Ga/H-ZSM-5 and H-ZSM-5 catalysts, which could indicate a strong interaction between metal species and the Al framework on the catalyst surface leading to lower crystallinity.[24] As a result of the impregnation method used during preparation of these catalysts most of the V particles likely remained on the zeolite external surfaces and did not diffuse into the pore structure of HZSM-5. In contrast, Ga_2O_3 can thermally diffuse inside H-ZSM-5 micropores and anchor to the Brönsted acid sites as reported by Xu et al.[25] and Borry et al.[26] No effect on the diffraction patterns was observed between Cr addition to its dopants

suggesting that Cr addition had no significant effect on the crystallinity of that catalyst compared to V. This could be due to the difference in V, and Cr concentrations.[27]

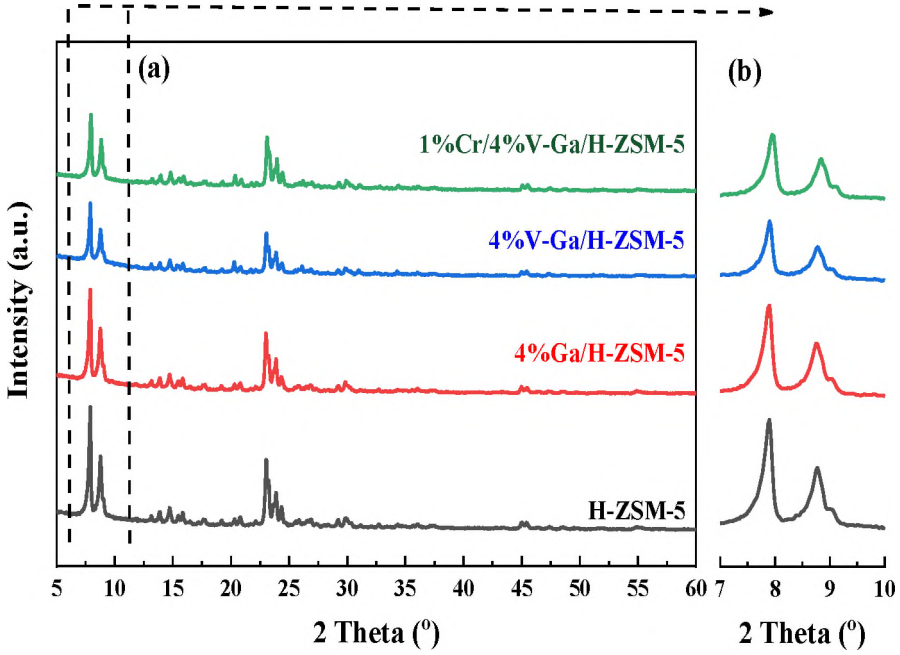

Figure 1. XRD patterns of the bare and Ga/, V-Ga/, and Cr/V-Ga/ doped H-ZSM-5.

The total number of acid sites on the catalysts was determined by ammonia-temperature-programmed desorption (NH_3-TPD) analysis. From this characterization, information about the different types of acid sites and their strength can be obtained on a regular basis. Figure 2 represents NH_3-TPD profiles of H-ZSM-5 before and after loading with metal dopants. The position and distribution of weak and medium-strong acid sites were determined using the NH_3-TPD profiles (Table 1). Pure H-ZSM-5 exhibited two NH_3 desorption peaks at 269 and 536 °C from weak acid sites (mostly Lewis acid) and medium-strong acid sites (mostly Lewis and Brönsted acid), respectively.[27] Since the zeolite sample is acidic and possess high crystallinity, the number of molecules of ammonia

desorbed at high temperature are proportional to the number of atoms of aluminum in zeolites. Ammonia, which is desorbed at low temperatures, is mainly absorbed on metal cation, while in H form or shape of the acidic zeolite, NH_3 is absorbed on Brønsted acid sites and NH^{4+}. The driving force behind this kind of absorption is mainly based on the electrostatic interactions between the sites of ion exchange and N-H bonds. The interaction of water molecules with such status (hydrogen bonding) is stronger than the interaction of ammonia, because the polarity of O-H in water is more than N-H of Ammonia, so this type of ammonia is replaced with water. Thus, low temperature peak has no solid acidic properties on the H zeolite. In other hands, the ammonia that remains after the water evaporation must interact with acidic sites, because the amount of ammonia is more than water. While ammonia is absorbed on the Brønsted acid sites, it can also absorb on the sites of Al or Al outside the structure of zeolites. When the ammonia is adsorbed on the solid acid (ions with high loads and low beam) due to the strong interaction at a higher temperature desorption is occurred. Quantitative analysis results of different acid sites and their Ga/H-ZSM-5 has shown higher amount of weak acid sites (301 μmol/g_{cat}) compared to the parent H-ZSM-5 (157 μmol/g). The decrease in Brönsted acid sites suggests that some of the Ga oxide migrated via surface thermal diffusion mechanism during heat treatment into H-ZSM-5 channels anchoring to the bridging hydroxyl groups of tetrahedral Al framework sites.[25] Meanwhile, the increase in the Lewis acid sites upon addition of Ga species is also indicative of highly dispersed Ga_2O_3 on H-ZSM-5 thereby, generates extra Lewis acid sites. For the V/ doped-Ga/H-ZSM-5 catalyst, the total acid quantity is the highest (494 μmolNH_3 g^{-1}), but the strong acid proportion is the lowest compare to the Ga/H-ZSM-5 and H-ZSM-5. This could indicate that V incorporation had a positive effect

on the increase in the acid site (especially the Lewis acid site) number with insignificant effect on the number of Brönsted acid sites confirming that V is mostly deposited on the catalyst surface, as the XRD and BET results suggested. Similarly, Xu et al.[25] showed that the addition of Fe did not negatively influence the Brönsted acid sites distribution since they are supported on the external surfaces. Figure 2 shows the NH_3-TPD profiles of V-Ga/H-ZSM-5 before and after impregnation with Cr species. It is clear that deposition of transition metal dopant brings about a decrease of the overall acidity as compared to V-Ga/H-ZSM-5 . This may be due to the coverage of (V, and Ga) species and H-ZSM-5 by Cr species, thereby, resulting in leading to the improvement of the catalytic activity. Meanwhile, these results suggest that calcination at 550 ^{o}C after H-ZSM5 reduces the amount of acidic site of zeolite by framework collapse due to dealumination, and metal dopants enhance the framework collapse.[28][29]

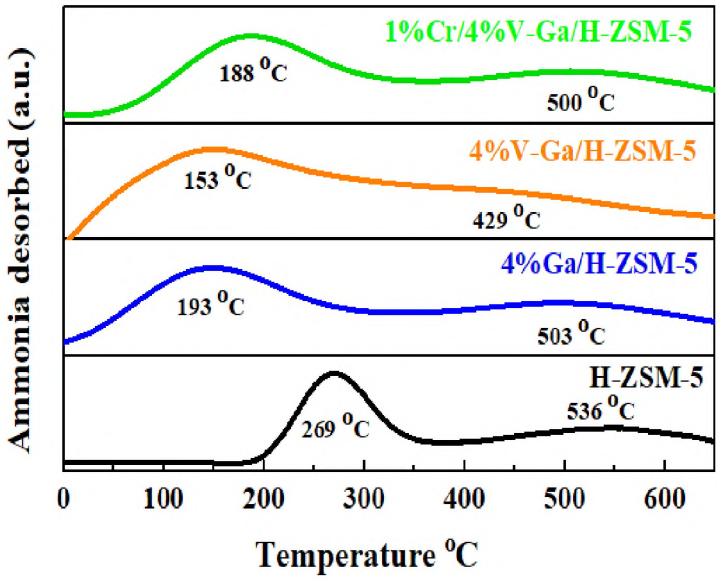

Figure 2. Peak fitting results of NH_3-TPD profiles of the bare and Ga/, V-Ga/ , Zr-V-Ga/ , Cr/V-Ga/ , and Cr/Zr-V-Ga/ doped H-ZSM-5.

Table 1. Summary of calculations for acid site analysis based upon NH_3-TPD profiles.

Catalysts	Total weak acid peak[a]		Total medium-strong peak[a]		Total acid[a]
	T (°C)	Amount ($\mu molNH_3\ g^{-1}$)	T (°C)	Amount ($\mu molNH_3\ g^{-1}$)	Amount ($\mu molNH_3\ g^{-1}$)
H-ZSM-5	269	157	536	248	405
4%Ga/H-ZSM-5	193	301	503	148	449
4%V-Ga/H-ZSM-5	153	331	429	163	494
1%Cr/4%V-Ga/HZSM-5	188	243	500	211	454

[a]Determined from NH_3-TPD results.

The redox properties of the various metal doped-H-ZSM-5, H_2-TPR analysis was performed, and the corresponding reduction curves and amount of H_2 consumption are shown in Figure 3 and Table 2, respectively. H_2-TPR profile of Ga/H-ZSM-5 catalyst consist of low-temperature reduction at (~ 368 °C) peaks and high-temperature reduction peaks at (~ 708 °C) peaks. The low-temperature reduction is associated to highest number of exchangeable sites, to the reduction of the reminiscent not oxidized Ga^{3+} cations compensating the negative charge of the zeolite. Similar results were also observed by Brabec et al.[30] Upon Ga introduction to the H-ZSM-5 zeolite, the reduction becomes difficult, and as such the five reduction peaks of the Ga modified H-ZSM-5 catalysts translate to higher temperatures (centred ~ 260, 383, and 662 °C) as observed in Figure 3. The principal reason in the increase of the reduction temperature is related to the Ga_2O_3 species being highly dispersed onto the H-ZSM-5 zeolite host. Previous literature [31] has implied that the major peak (~ 383 °C) is assigned to the reduction of small Ga_2O_3 particles to Ga^+ on the external H-ZSM-5 surface, while the response at (~ 662 °C) is related to $(GaO)^+$, an oxo Ga^{3+} species that interacts strongly with H-ZSM-5 at the cation position in cavities. The response at (> 662 °C) is related to the reduction of segregated,

large Ga_2O_3 clusters to Ga_2O, which is in accordance with the XRD results for Ga/H-ZSM-5 that no Ga_2O_3 peaks were found, resulting in the Ga_2O_3 particles are finely dispersed. The H_2-TPR profile for the introduction of vanadium oxide to Ga/H-ZSM-5 shows reduction temperature peak as (~468 °C) attributed to the reduction of monomeric, dimeric, and oligomeric $(V_4^{3-})_n$ species in tetrahedral coordination geometry[32], while, the peak at (~ 622 °C) should probably be ascribed to the reduction of dispersed vanadia species as (crystalline and polymeric vanadia) on the surface of Ga/H-ZSM-5 as also correlated with the XRD (Figure 1) results. By analogy with previous studies on the reducibility of VO_x/SiO_2 and other V containing mesoporous materials[33], the peak at low temperature is attributed to the reduction of dispersed tetrahedral vanadium species, whereas the peak at 468 °C is attributed to the reduction of polymeric V^{5+} species V_2O_5-like. The response at (> 622 °C) is attributed to the V_2O_3, for the complete reduction of bulk V_2O_5 species from V^{5+} to V^{3+} as demonstrated by Muhler et al.[34] With the surface vanadium coverage increasing, the area of hydrogen consumption peak gradually went up, which provided more and more redox sites for oxidative dehydrogenation of propane in presence and absence of CO_2 towards propene. The appropriate value of redox sites facilitated the formation and transform of propene. The impregnation of vanadium oxide not only provided the redox sites, but also changed the acid strength significantly and distribution of Ga/H-ZSM-5 zeolite as confirmed by NH_3-TPD (Figure 2) measurement. The oxide reduced the number of strong acid sites, and simultaneously increased the amount of weak acid sites (increasing Lewis acid sites), thereby increasing the dispersion of gallium as shown in Table 3.[35] The modification of the support plays a pivotal role to determine the activity of the active species. The reduction profile peaks of Cr/V-Ga/H-

ZSM-5 catalyst consist of reduction temperature peaks at 327-604 °C as observed in Figure 3. The low temperature reduction (327 °C) reduction peak could be due to the reduction of chromium, vanadium, and gallium species and later are for the reduction of Cr^{5+} to Cr^{3+} and Cr^{3+} to either Cr^{2+} or to Cr^{0}.[39] It is suggested that Cr reduction is dominant over the V, and Ga species in the Cr/V-Ga/H-ZSM-5 catalyst, which may be due to the coverage of vanadium, and gallium species by the chromium ions.[40] The high temperature reduction peaks (604 °C) of Cr/V-Ga/H-ZSM-5 show much lower intensity/quantities than low temperature reduction as shown in (Figure 3 and Table 3), and is typically connected with bulk Cr_2O_3 reduction to oxidation states lower than +3 [41], as well as to hydrogen adsorption either on chromium, zirconium, vanadium, and gallium. We cannot also rule out that high temperature reduction is due to reduction of Cr(VI) mono-oxo species. This result indicates that the Cr(III) on Cr/V-Ga/H-ZSM-5 has a stronger association capability for hydrogen, which indicates a better dehydrogenation ability. Meanwhile, Table 3 shows higher consumption of hydrogen reflects higher amount of Cr(VI) and Cr(V) species which as was mentioned above are precursors of redox Cr(III) and Cr(II) sites catalytically active in oxidative dehydrogenation of propane in presence or absence of CO_2 process. The latter redox in origin sites together with non-redox Cr(III) species are responsible for high catalytic activity of Cr/V-Ga/H-ZSM-5, which improved the mobility of the oxygen as well as the valence and oxidization properties of metal dopants[42], thus increase the dispersion of gallium as illustrated in (Figure 3 and Table 3).

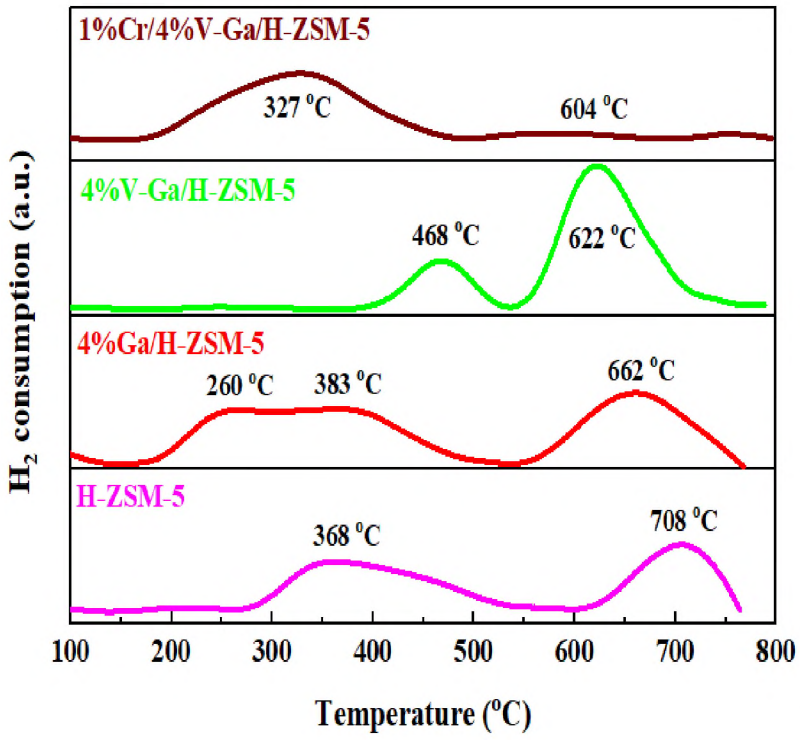

Figure 3. H_2-TPR profiles with peak fitting of the bare and Ga/, V-Ga/ , Cr/V-Ga/ doped H-ZSM-5.

Table 2. Summary of calculations for H_2 consumption from the H_2-TPR profiles.

	H_2 consumption value (mmol g^{-1}) [a]		Total H_2-consumption[a]
Catalysts	T (°C)	Amount (mmol g^{-1})	Amount (mmol g^{-1})
H-ZSM-5	368 708	0.215 0.123	0.338
4%Ga/H-ZSM-5	260 383 662	0.208 0.372 0.705	1.285
4%V-Ga/H-ZSM-5	468 621	0.200 1.300	1.500
1%Cr/4%V-Ga/HZSM-5	327 604	2.337 0.478	2.815

[a]Determined from NH_3-TPD results.

The N_2 adsorption-desorption isotherms and their corresponding pore size distribution of the studied materials are presented in Figure 4 . All samples exhibit type IV physisorption relating to the presence of mesoporosity with hysteresis loops of various sizes in the relative pressure range of 0.45 to 1.0, according to the IUPAC classification.[43] For the metal oxides doped-H-ZSM-5 zeolites, there is an apparent type H3 hysteresis loop as shown in Figure 4 because of the presence of both mesopores and macropores at high relative pressure (p/p_0 = 0.8-1.0) relating to inter-crystalline voids produced by stacking of the nano-sized crystals.[44] The Barrett-Joyner-Halenda (BJH) method is one model typically employed to determine the mesopore size distribution.[45] The pore size distribution curves of samples, derived from the BJH model using the adsorption branch of the isotherms, are shown in Figure 4. The metal oxides doped-H-ZSM-5 zeolites shows mesoporous size distribution varies in the narrow range of 3-5 nm with the maxima centered ~ 4 nm and 20-50 nm. Furthermore, samples clearly show the presence of significant macropores (> 50 nm). As listed in Table 3, after loading metal dopants, the BET surface area declined from 470 m^2 /g to 417, 297, and 334 m^2 /g for H-ZSM-5, Ga/H-ZSM-5, V-Ga/H-ZSM-5, and Cr/V-Ga/H-ZSM-5, respectively. The results can be ascribed to the metal dopants which disperse in the pore canal and block the pores. Similarly, the pore volume also attenuated from 0.43 cm^3 g^{-1} to 0.32, 0.23, and 0.29 cm^3 g^{-1} for H-ZSM-5, Ga/H-ZSM-5, V-Ga/H-ZSM-5, and Cr/V-Ga/H-ZSM-5, respectively. It should imply that after Cr addition to V-Ga/H-zsm-5, the BET surface area increases from 297-334 as well as pore volume from (0.23-0.29 cm^3 g^{-1}) as a function of decreasing crystal size. Additionally, there is a corresponding increase in mesopore volume from 0.16 to 0.21 cm^3/g. These results match well with previous literature.[46] The change of the

micropore volume was less significant than the change in the mesopore volume after metal incorporation, suggesting that the decrease in pore volume resulted from the metal dopant clogging in the mesopores of the zeolite. The average crystal sizes of the samples were also quantified by applying the Debye-Scherrer equation and the size of the metal oxides doped-H-ZSM-5 particles were determined to be less than 22 nm, as listed in Table 3. The results observed that the average crystal size was in nanometers scale and that the addition of metal dopant nanoparticles slightly decreased the average crystal size compare to parent zeolite thus hinder the agglomeration of metal dopants.[47] Decrease in crystallinity in other catalysts is due to the leaching of the aluminum to the external sides of the structure and the filling of the pores by silica. These findings are in good agreement with previous literature.[48] The active metal surface area (ASA) is increased proportional with addition of metal oxides (V, and Cr) compare to Ga/H-ZSM-5. Based on average crystal size results, the Ga dispersion was calculated to be 22-29% as presented in Table 3, indicating the formation of highly dispersed Ga metal particles. The high dispersion of the Ga nanoparticles is resulted from the homogeneous distribution of Ga species in the (MGa/H-ZSM-5)O, M = (V, and Cr) calcined product as well as the strong interaction between Ga and V, and Cr. This has been confirmed by XRD profiles (refer Figure 1), as discussed earlier. This finding is in an agreement with previous studies.[49]

3.2. CATALYTIC PERFORMANCE

The performance of the bare and Ga-, and Cr-doped H-ZSM-5 zeolites for ODP reaction was carried out at 400-550 °C and atmospheric pressure in presence and absence of CO_2 with WHSV of 4 Kg_{cat} s mol^{-1}_{C3H8} .

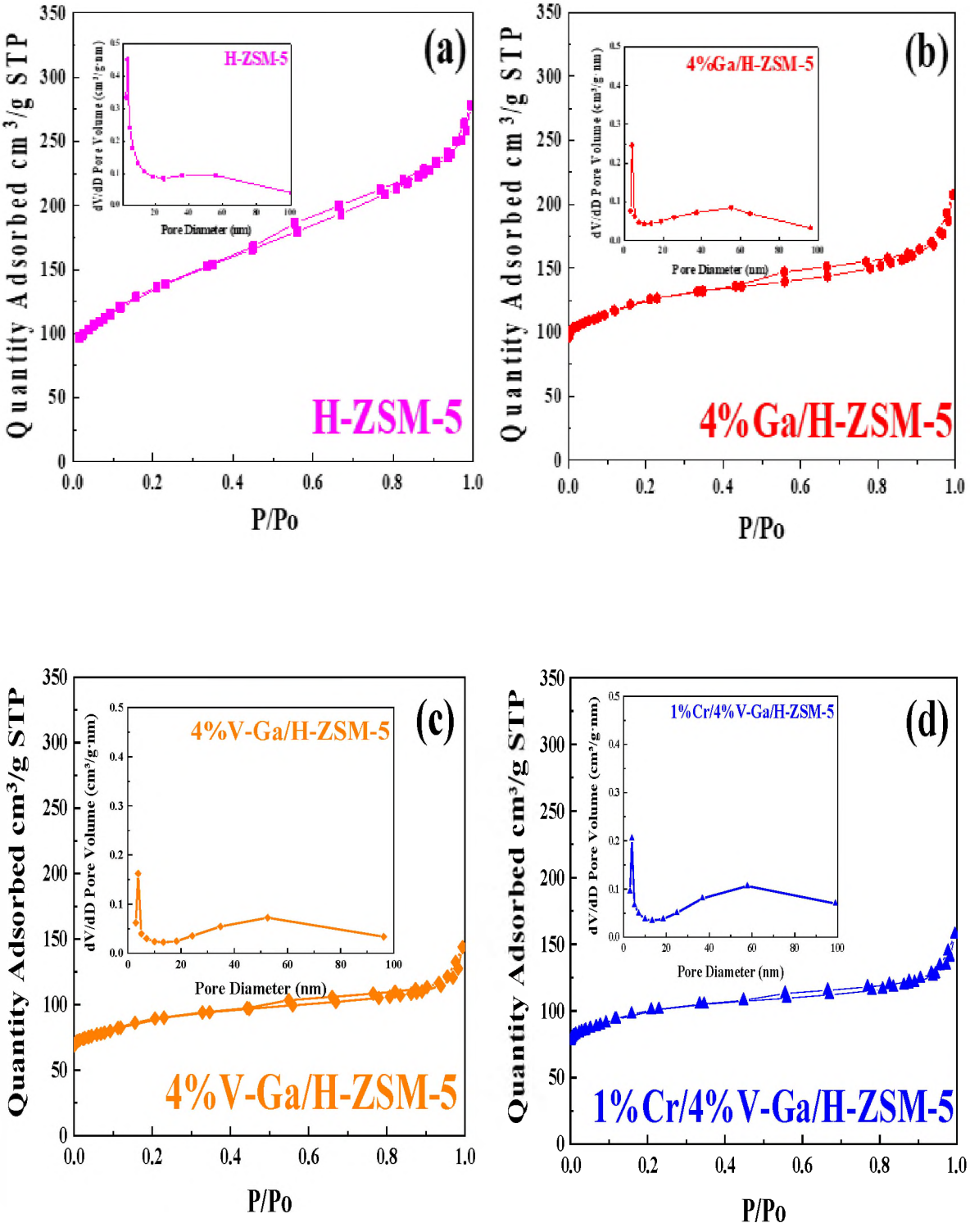

Figure 4. N_2 physisorption isotherms of metal oxides doped-H-ZSM-5 zeolites.

Table 3. Characteristic properties of metal oxides doped-H-ZSM-5 zeolites.

Catalysts	S_{BET} (m^2/g)[a]	S_{micro} (m^2/g)[b]	S_{ext} (m^2/g)[b]	V_{total} (cm^3/g)[b]	V_{micro} (cm^3/g)[b]	V_{meso} (cm^3/g)[d]	Pore size (nm)[e]	Dp (nm)[f]	ASA (m^2/g)[g]	D%[h]
H-ZSM-5	470	248	222	0.43	0.13	0.30	4.44	21	–	–
4%Ga/H-ZSM-5	417	201	216	0.32	0.10	0.22	5.07	20	9	22
4%V-Ga/H-ZSM-5	297	130	169	0.23	0.07	0.16	4.62	16	10	26
1%Cr/4%V-Ga/H-ZSM-5	334	159	175	0.29	0.08	0.21	6.00	14	12	29

[a]Estimated by analyzing nitrogen adsorption data at -196 °C in a relative vapor pressure ranging from 0.05 to 0.30.
[b]Estimated by a *t*-plot method.
[c]Total pore volume was estimated based on the volume adsorbed at P/P_o =0.99.
[d]Estimated by subtracting $V_{meso} = V_{total} - V_{micro}$
[e]Estimated by BJH desorption average pore diameter.
[f]Estimated by Debye-Scherrer equation of XRD, Dp (average crystal size).
[g]Estimated by [Total number of surface metal atoms]*[Cross-section area of active metal].
[h]Estimated by moles of metal on surface sample/moles of total metal present in sample.

Intra-particle diffusion limitation can be excluded according to the Weisz-Prater analysis (shown in the supplementary information). The products obtained from the propane conversion over the investigated catalysts were mainly paraffins (methane (C_1) and ethane (C_2)), light olefins (ethene (C_2=), propene (C_3=), butene (C_4=) and pentene (C5=)), aromatics, BTX (benzene, toluene, and xylene), hydrogen (H_2), and CO as shown in (Figure 5 and Figure 6). Both propane conversion and carbon dioxide conversion increased monotonically with increasing temperature. To probe the advantages of H-ZSM-5 as a control experiment to evaluate the potential impact of H-ZSM-5. Figure 5 & Figure 6 & Table 4 and Table 5, show both the conversion of the propane and the selectivity of the hydrocarbon product as a function of time on stream and raising of reaction temperatures over the investigated catalysts. The H-ZSM-5 catalyst performance (Figure 5a & Figure 6& Table 4 and Table 5) was further significantly increased propane conversion and propene selectivity in presence CO_2 over absence CO_2 (34% vs 32%) and (20 vs 9) at 550 °C. The product distribution for propane conversion over H-ZSM-5-RE-

OX during ODP reaction in presence and absence of CO_2 is summarized in (Figure 5a & Figure 6 & Table 4 and Table 5). On the other hand, a Ga/H-ZSM-5 catalyst showed a higher conversion of propane and propene selectivity in presence of CO_2 to in absence CO_2 (54% vs 48%) and (25 vs 23) compare to H-ZSM-5 as shown in Figure 5b. This indicates the incorporated gallium with H-ZSM-5 leads to reduce concentrations of Brønsted acid sites and more Lewis acid sites, with significant concentrations of strong Lewis acid sites. These results are in agreement with Choudhary et al.[50], the propene selectivity was estimated to be about 15% at this conversion level. The improved performance in these Ga-MFI samples prepared with MPS addition is likely due to the lower concentration of Brønsted acid sites, as exemplified in MG11, since it is believed that Brønsted acid sites are active in the oligomerization and cyclization steps of alkane aromatization and subsequently form coke.[51] During the oxidative dehydrogenation of propane in presence of CO_2 process over the Ga/H-ZSM-5, Ga species catalyze the dehydrogenation of propane and intermediates, thus promoting the conversion of propane. Brønsted acid sites are responsible for the oligomerization, cyclization and cracking of olefins, while Lewis acid sites catalyze the dehydrogenation reaction.[52] Therefore, the lower selectivity to cracking products of Ga/H-ZSM-5 is attributed to the decrease in the Brønsted acid sites evident from NH_3-TPD profile (refer Figure 2 and Table 1). Thus, it can be deduced that the gallium species and the acid sites of Ga/H-ZSM-5 collaboratively catalyze the dehydrogenation, oligomerization and cyclization of olefins to aromatics, but inhibit the cracking reaction over the Ga/H-ZSM-5 treated at different conditions at the reaction time of 10 h were summarized in Table 4 and Figure 6. Furthermore, reduction-oxidation treatment of Ga/H-ZSM-5 (Ga/H-ZSM-5-RE-OX) prior to reaction has a crucial impact on ODP process

shows higher propane conversion and light olefin selectivity and aromatic selectivity and lower cracking product selectivity in presence of CO_2 than in absence of CO_2 [53], as shown in (Figure 5b, Figure 6, Table 4, and Table 5). This may be closely related to the state of gallium species in the Ga/H-ZSM-5. However, that the gallium species in the air-oxidized sample are likely present as Ga_2O_3 particles finely dispersed on the outer surface of zeolite crystals, while H_2-reduced sample mainly contains Ga^+ and GaH^{2+}, which are more active than Ga_2O_3 particles.[54] In contrast, the gallium species in the reduced and subsequently oxidized sample are GaO^+ located in the internal surface and the cation-exchange positions of ZSM-5.[55] It was reported that the initial aromatization activity of GaO^+ is much higher than that of Ga^+ and GaH^{2+}.[56] In addition, the GaO^+ well-dispersed in the zeolite channels can closely contact with propane and intermediates. Therefore, (Ga/H-ZSM-5- RE-OX) in presence of CO_2 depicts higher catalytic activity for aromatization of propane and light olefin selectivity compare to (Ga/H-ZSM-5-RE-OX) absence of CO_2. As observed, V-Ga/H-ZSM-5 shows high propane conversion and propene selectivity in presence of CO_2 to in absence of CO_2 (60% vs 58%) and (89% vs 85%) at 550 °C as illustrated in Figure 5c. V species modification of the Ga/H-ZSM-5 zeolite led to stronger metal–support interactions between the Ga species and the zeolite [57], it was suggested that the addition of vanadia provides more weak surface acid sites and more active sites for catalysis as shown in Figure 2 and Table 1. Furthermore, additive vanadia inhibited the loss of active gallium species during the reaction by supplying electrons to anchor the active gallium species. Therefore, these phenomena were responsible for the high catalytic activity of the V- containing Ga/H-ZSM-5 catalyst towards target selectivity.[58] additionally, V species into the Ga/H-ZSM-5 has a great effect on the reaction, not only on the conversion of

propane, but also on the selectivity of propene compare to Ga/H-ZSM-5.This result is consistent with H_2-TPR profile (Figure 3). The product distribution, however, essentially changed as shown in (Table 4 and Table 5). Furthermore, reduction-oxidation treatment of V-Ga/H-ZSM-5 (Ga/H-ZSM-5-RE-OX) prior to reaction has a crucial impact on ODP process shows higher light olefin (i.e. ethene, propene, and pentene) selectivity and lower cracking product (methane) selectivity in presence of CO_2 than in absence of CO_2 [53], as shown in (Figure 5c, Figure 6, Table 4, and Table 5). When vanadium oxide was mixed, the conversion of carbon dioxide and the rate of consumption of hydrogen were remarkably improved. The consumption of hydrogen is defined as the proportion of hydrogen consumed, by the reverse water-gas shift conversion, to that formed by dehydrogenation of propane as shown in (Table 4 and Table 1). Therefore, the appearance of the multiple peaks suggests that successive reduction-oxidation cycles results in aggregation of some of the surface vanadia species.[59] Figure 5d shows high propane conversion and propene selectivity in presence of CO_2 to absence of CO_2 (67% vs 63%) and (89% vs 84%) at 550 °C over Cr- containing V-Ga/H-ZSM-5. The reason is reflecting higher amount of Cr(VI) and Cr(V) species which as was mentioned above are precursors of redox Cr(III) and Cr(II) sites catalytically active in ODP reaction. The latter redox in origin sites together with non-redox Cr(III) species are responsible for high catalytic activity of Cr- containing V-Ga/H-ZSM-5 catalyst, in agreement with (TPR analysis; Figure 3 and Table 2). However, the reduced Cr species on the H-ZSM-5 are re-oxidized to Cr^{6+} (or Cr^{5+}) species easily by CO_2 treatment. Then, the activation energy recovers to almost the same initial value by CO_2 treatment after hydrogen treatment.[60] This result indicates that the reduced Cr active species is easily re-oxidized by CO_2 to a highly active initial state, which is in consistent

with previously reported work by Ohishi et al.[61] The distribution data for propane conversion over Cr/V-Ga/H-ZSM-5-RE-OX during ODP reaction, afforded a light olefin (i.e. ethene and propene) selectivity in presence of CO_2 compare to absence of CO_2 as summarized in (Figure 6, Figure 7,Table 4, and Table 5. However, the reduced Cr species on the H-ZSM-5 are re-oxidized to Cr^{6+} (or Cr^{5+}) species easily by CO_2 treatment. Then, the activation energy recovers to almost the same initial value by CO_2 treatment after hydrogen treatment.[60] This result indicates that the reduced Cr active species is easily re-oxidized by CO_2 to a highly active initial state, which is in consistent with previously reported work by Ohishi et al.[61] and Takehira et al.[6] studied Cr-MCM-41 catalysts for the dehydrogenation of ethylbenzene to styrene and propane to propylene. They studied the Cr species on the MCM-41 mesoporous silica and concluded that a redox process involving carbon dioxide forming Cr^{6+} species is involved in the dehydrogenation.

The turnover frequency (TOF) representing the activity of Cr, V and Ga-doped H-ZSM-5 zeolites for ODP reaction was carried out in presence and absence of CO_2 within temperature range of 400-550 ^oC are also shown in Table 4 and Table 5. The TOF herein is defined as the moles of propane/product reacted or produced over per unit mole of acid cite per unit time. The acid amount was estimated using NH_3-TPD as listed in Table 1. It can be seen that Cr/V-Ga/H-ZSM-5 catalyst has the highest TOF_{C3H8} value to other catalysts in presence CO_2 to absence of CO_2, which should be ascribed to the high interaction and dispersion metal dopants onto catalyst surface as in accordance with XRD results (Table 3).

Notably, all catalysts, at the beginning of the reaction, the propane conversion is higher in the absence of CO_2 than in presence of CO_2 . This probably be indicative that

CO_2 was absorbed on the metal-oxide catalyst surfaces and/or on the active sites, forming carbonate species at low temperatures and blocking the sites for propane adsorption in the first step. However, with desorption of CO_2 as a function of temperature Although nanoparticles of oxides, with basic properties could be active for dehydrogenation of hydrocarbon at low temperatures, the strong adsorption of olefin on active site make the reaction impracticable at low temperature.[64] For ODP-CO_2 the strong adsorption of H_2O formed during oxidation could adsorb on active site.[65] Thus, reactants and products in ODP-CO_2 contribute to blocks the basic active site at low temperatures. Both effects caused decreases in the initial conversions in the presence of CO_2.[25] The catalyst deactivated much slowly in the presence of CO_2 than in the absence of CO_2. Due to, in the presence of CO_2, in the presence of CO_2, nevertheless, the catalyst stability improved due to reverse Boudouard reaction ($CO_2 + C \rightarrow 2CO$), which prevents deposition of active carbon species on the metal surface. Moreover, this could be due to the difference in the particle size, reducibility of metals and surface texture of the metal oxides. Additionally, transforming H_2 into CO and H_2O through the RWGS reaction. Considering the above, it seems that CO_2 can participate in direct oxidation of propane to propene via followed a bi-functional Mars-Van Krevelen (MvK) redox mechanism dominated that CO_2 could be readily activated on the partially reduced Ga or metal-Ga interface, and the formed active oxygen species subsequently promoted propane conversion.

The donation of oxygen species and/or in the removal of H_2 in the RWGS reaction. Therefore, the roles of CO_2 in the dehydrogenation of propane under a CO_2 atmosphere would be considered either as lattice oxygen supplier to maintain the metal dopants species at higher valence state and help redox cycle proceed or as hydrogen consumer in RWGS

reaction. Another role of CO_2 in the dehydrogenation of propane might be the assistant in the rapid desorption of product (propene) from the surface of the catalyst which seems to be necessary for obtaining high dehydrogenation activity and anticoking [65]. This finding in a good agreement with our results as presented in Figure 7, Table 6, and Table 7. The trend for CO_2 conversion was more stable than propane conversion over all the Ga/, and Cr/ doped H-ZSM-5 zeolites under the same condition. The conversion of propane in presence of CO_2 increases with the elevation of the reaction temperature (400, 450, 500, and 550 ^oC) while the selectivity to propene gradually drops as shown in (Table 4 and Table 5). At the same time, the selectivity to by-products (i.e. methane and ethane….etc.) rise as the temperature augment, indicating facilitation of side reactions, like cracking and hydrocracking, at high temperatures. Moreover, the elevate of the reaction temperature improves useful by-products, H_2 and CO as shown in (Table 4).

3.3. INVESTIGATION OF HEAT AND MASS TRANSFER LIMITATION

Kinetic data collection in any experiment can only be considered intrinsic in the absence of heat and mass transport limitations. Since catalytic oxidative of dehydrogenation of propane with carbon oxide reaction at high temperatures (550 ^oC) are very fast and tend to be mass-transfer limited, it is very important to determine to what extent, if at all, these transport resistances affect the rate of reaction. Several correlations are available in the literature to determine the effects that interparticle and intraparticle heat and mass transport limitations could have on the rate of reaction. In our work, these effects were investigated at a temperature of 550 ^oC and the low pressure (1 bar) for 1%Cr/4% V-Ga/H-ZSM-5 , which are used for the reaction.

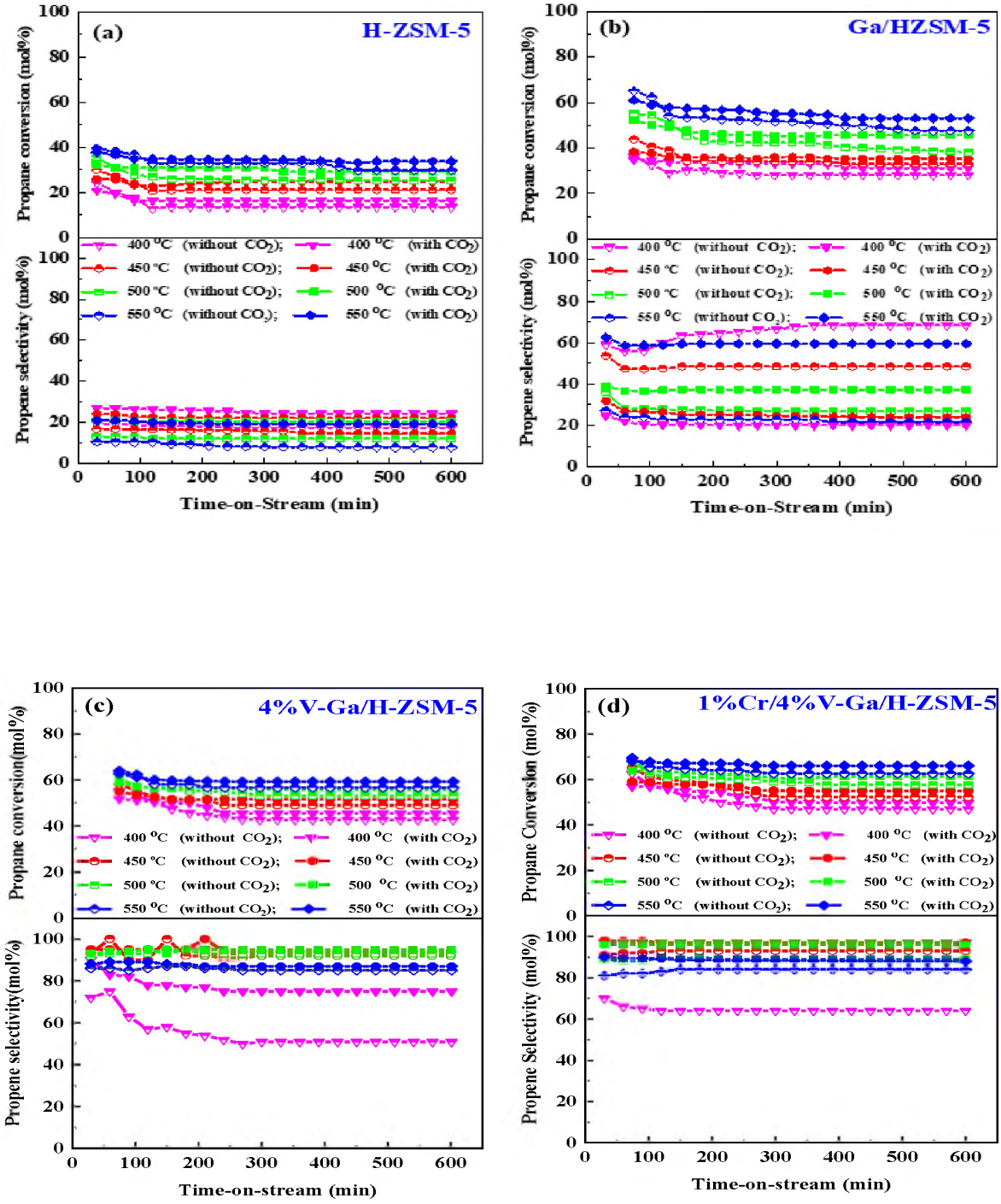

Figure 5. Catalytic performance of the (a) H-ZSM-5; (b) 4%Ga/H-ZSM-5; (c) 4%V-Ga/H-ZSM-5; and (d) 1%Cr/4%V-Ga/H-ZSM-5 catalysts. Reaction condition ; reaction temperature, 400-550 °C ; Pressure, 1 bar ; feed gas, C_3H_8/N_2 = 2.5/97.5 and $C_3H_8/CO_2/N_2$ = 2.5/5/92.5; flow rate, 75 mL min^{-1}, WHSV, 4 Kg cat s mol_{C3H8}^{-1} .

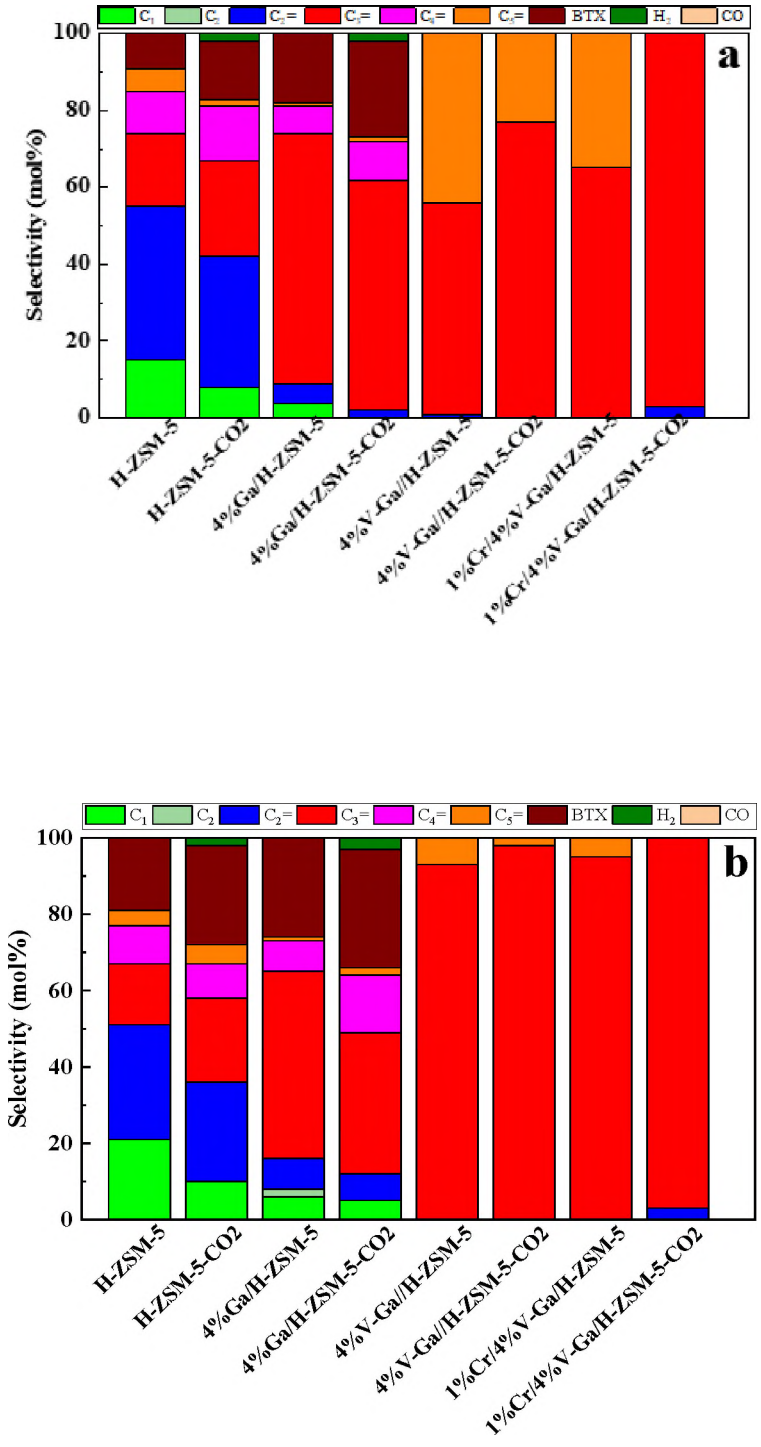

Figure 6. Product distribution of bare and the metal oxides doped-H-ZSM-5 zeolites in presence and absence of CO_2 at (a) 400 °C , (b) 450 °C, (c) 500 °C, and (d) 550 °C. Reaction condition ; reaction temperature, 400-550 °C ; Pressure, 1 bar ; feed gas, C_3H_8/N_2 = 2.5/97.5 and $C_3H_8/CO_2/N_2$ = 2.5/5/92.5; flow rate, 75 mL min^{-1}, WHSV, 4 Kg cat s mol_{C3H8}^{-1} .

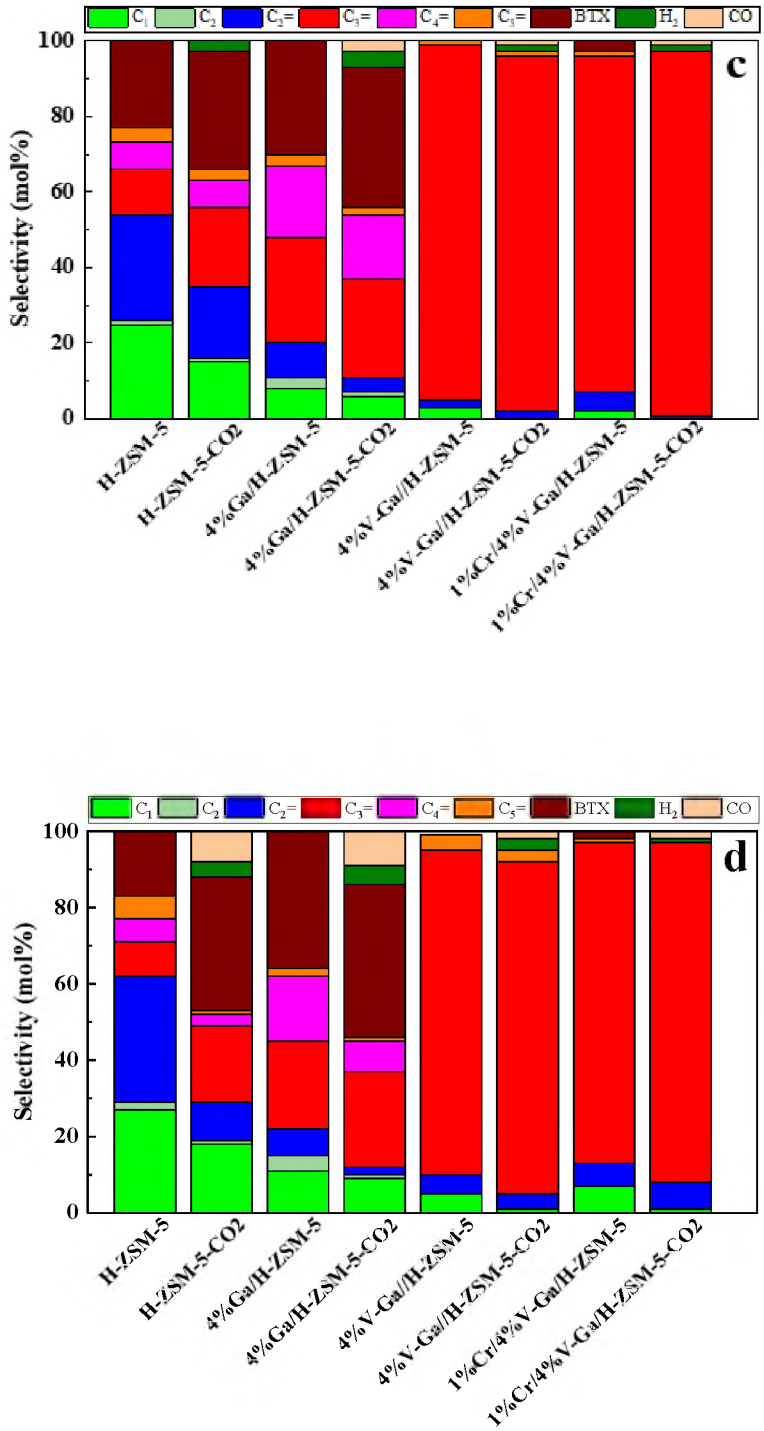

Figure 6. Product distribution of bare and the metal oxides doped-H-ZSM-5 zeolites in presence and absence of CO_2 at (a) 400 °C , (b) 450 °C, (c) 500, and (d) 550. Reaction condition ; reaction temperature, 400-550 °C ; Pressure, 1 bar ; feed gas, C_3H_8/N_2 = 2.5/97.5 and $C_3H_8/CO_2/N_2$ = 2.5/5/92.5; flow rate, 75 mL min^{-1}, WHSV, 4 Kg $_{cat}$ s mol_{C3H8}^{-1} (cont.).

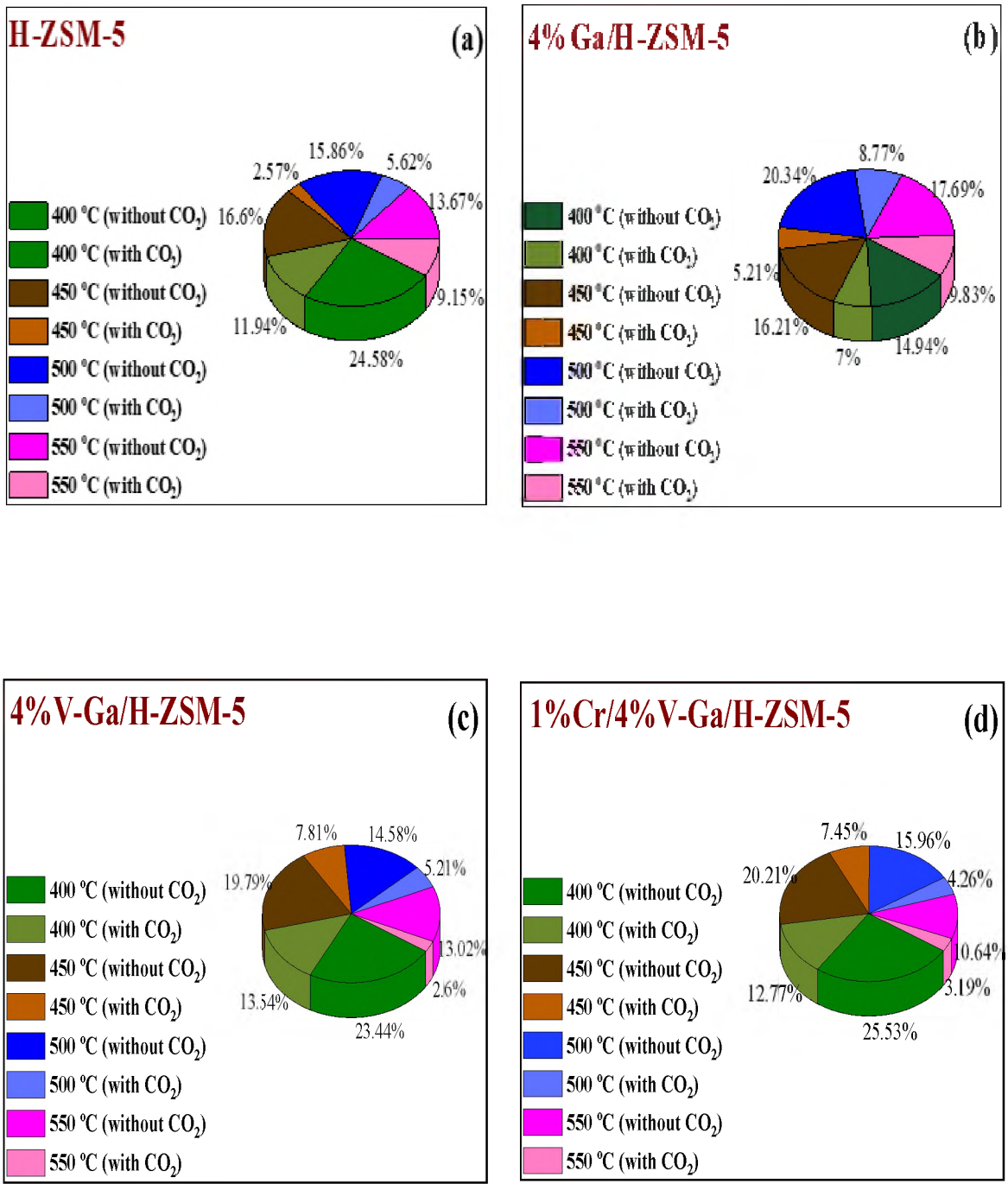

Figure 7. Deactivation factor of the bare and metal doped-H-ZSM-5 zeolites in presence and absence of CO_2 at (a) 400 °C , (b) 450 °C, (c) 500 °C, and (d) 550 °C. Reaction condition ; reaction temperature, 400-550 °C ; Pressure, 1 bar ; feed gas, C_3H_8/N_2 = 2.5/97.5 and $C_3H_8/CO_2/N_2$ = 2.5/5/92.5; flow rate, 75 mL min^{-1}, WHSV, 4 Kg $_{cat}$ s mol^{-1}_{C3H8}.

Table 4. Summary of catalytic test of metal oxides doped-H-ZSM-5 zeolites in presence CO_2.

Catalysts	Conversion (mol%)			Selectivity (mol%)									
	Temp. (°C)	C_3H_8	CO_2	C_1	C_2	$C_2^=$	$C_3^=$	$C_4^=$	$C_5^=$	BTX	H_2	CO	TOF^a_{C3H8} $\times10^{-2}(h^{-1})$
H-ZSM-5	400	16	8	8	–	34	25	14	2	15	2	–	–
	450	25	16	10	–	26	22	9	5	26	2	–	–
	500	29	21	15	1	19	21	7	3	31	3	–	–
	550	34	25	18	1	10	20	3	1	35	4	8	–
4%Ga/H-ZSM-5	400	32	18	–	–	2	60	10	1	25	2	–	35
	450	35	23	5	–	7	37	15	2	31	3	–	36
	500	46	32	6	1	4	26	17	2	37	4	3	44
	550	54	42	9	1	2	5	8	1	40	5	9	49
4%V-Ga//H-ZSM-5	400	47	35	–	–	–	77	–	23	–	–	–	1.91
	450	52	40	–	–	–	98	–	2	–	–	–	1.98
	500	56	47	–	–	2	94	–	1	–	2	1	1.99
	550	60	50	1	–	4	87	–	3	–	3	2	2.00
1%Cr/4%V-Ga/H-ZSM-5	400	52	40	–	–	3	97	–	–	–	–	–	2.01
	450	57	46	–	–	3	97	–	–	–	–	–	2.02
	500	62	51	–	–	1	96	–	–	–	2	1	2.08
	550	67	56	1	–	7	89	–	–	–	1	2	2.12

[a] Estimated by moles of propane/product reacted or produced over per unit mole of acid cite per unit time. Reaction condition ; reaction temperature, 400-550 °C ; Pressure, 1 bar ; $C_3H_8/CO_2/N_2$ = 2.5/5/92.5; flow rate, 75 mL min^{-1}, WHSV, 4 Kg $_{cat}$ s mol^{-1}_{C3H8}

3.3.1. Heat Limitation. The internal pore heat transfer resistance was estimated using the Prater analysis, adopted from Ibrahim and Idem[66], is given by

$$\Delta T_{particle,max} = \frac{D_{eff}(C_{As} - C_{Ac})\Delta H_{rxn}}{\lambda_{eff}} \quad (1)$$

where $\Delta T_{particle,max}$ is the upper limit of temperature variation between the pellet centre and its surface, ΔH_{rxn} is the heat of reaction, C_{As} and C_{Ac} are, respectively, the concentrations at the pellet surface and centre (assumed, respectively, to be the same as bulk concentration and zero, as suggested by Levenspiel, 1999), and D_{eff} is the effective mass diffusivity

obtained from $D_{eff} = \frac{D_{AB}\varepsilon_P}{\tau}$ [67], where D_{AB} is the bulk diffusivity of component A in B, which in turn, is estimated using the Brokaw equation.[68]

Table 5. Summary of catalytic test of metal oxides doped-H-ZSM-5 zeolites in absence CO_2.

		Conversion (mol%)	Selectivity (mol%)							
Catalysts	Temp. (oC)	C_3H_8	C1	C2	C2=	C3=	C4=	C5=	BTX	TOFa_{C3H8} ×10-2 (h-1)[a]
H-ZSM-5	400	13	15	–	40	19	11	6	9	–
	450	22	21	–	30	16	10	4	19	–
	500	23	25	1	28	12	7	4	23	–
	550	32	27	2	33	9	6	6	27	–
4%Ga/H-ZSM-5	400	28	4	–	5	65	7	1	18	0.31
	450	33	6	2	8	49	8	1	26	0.34
	500	38	8	3	9	28	19	3	30	0.37
	550	48	11	4	7	23	17	2	36	0.43
4%V-Ga//H-ZSM-5	400	45	–	–	1	55	–	44	–	1.83
	450	50	–	–	–	93	–	7	–	1.90
	500	54	3	–	2	94	–	1	–	1.91
	550	58	5	–	5	85	–	4	–	1.93
1%Cr/4%V-Ga/H-ZSM-5	400	49	–	–	–	65	–	35	–	1.94
	450	53	–	–	–	95	–	5	–	1.98
	500	58	2	–	5	89	–	1	3	1.99
	550	63	7	–	6	84	–	1	2	2.00

[a] Estimated by moles of propane/product reacted or produced over per unit mole of acid cite per unit time. Reaction condition ; reaction temperature, 400-550 oC ; Pressure, 1 bar ; C3H/N2 = 2.5/97.5; flow rate, 75 mL min^{-1}, WHSV, 4 Kg cat s mol^{-1}_{C3H8}.

Table 6. Summary of weight loss of metal doped-H-ZSM-5 zeolites in presence and absence of CO_2 at 800 °C.

	Weight loss%	
Catalysts	C[a]	C[b]
H-ZSM-5	0.039	0.025
4%Ga/H-ZSM-5	0.056	0.028
4%V-Ga/H-ZSM-5	0.035	0.032
1%Cr/4%V-Ga/HZSM-5	0.038	0.035

[a] In absence CO_2.
[b] In presence CO_2.

Table 7. Summary of carbon balance of metal doped-H-ZSM-5 zeolites in presence and absence of CO_2.

Catalysts	Temp. (°C)	Carbon Balance %	
		C_B[a]	C_B[b]
H-ZSM-5	400	96.917	97.69
	450	96.825	97.62
	500	96.461	97.52
	550	96.454	97.44
4%Ga/H-ZSM-5	400	97.949	98.32
	450	97.249	98.23
	500	97.366	98.15
	550	97.211	98.10
4%V-Ga//H-ZSM-5	400	98.334	99.202
	450	98.042	99.938
	500	98.887	99.792
	550	98.764	99.685
1%Cr/4%V-Ga/H-ZSM-5	400	99.221	99.999
	450	99.911	99.815
	500	99.685	99.629
	550	99.601	99.456

[a] In absence CO_2.
[b] In presence CO_2.

The value for D_{AB} was found, at the temperature of 823K, to be 1.41×10^{-6} m^2/s. The effective diffusivity D_{eff} was estimated to be 4.259×10^{-7} m^2/s. ε_p is the void fraction (estimated as the ratio of the volume occupied by voids to the total bed volume = 0.453) and calculated using the formula $\varepsilon_P = 0.38 + .073[1 + \frac{(d/dp-2)^2}{(d/dp)^2}]$ [69], where d and dp are the internal diameter of the reactor and the diameter of the particle, respectively. τ is the tortuosity factor.[66][67][70] λ_{eff} is the effective thermal conductivity obtained using the correlation, $\lambda_{eff}/\lambda=5.5+0.05N_{Re}$ [71] for packed bed tubular reactors. λ is the molecular thermal conductivity calculated using the Wassiljewa correlation to be 4.449×10^{-2} W/m/K

.[68] The effective thermal conductivity, λ_{eff}, was determined to be 2.447×10^{-4} kW/m/K. The detailed calculations are shown in (supplementary information, section-1). A value of 0.106 K was obtained for $\Delta T_{particle,max}$. The detailed calculation of internal pore heat transfer resistance, $\Delta T_{particle,max}$, is shown in (supplementary information, section-1).

The heat transfer limitation across the gas film was determined using the following correlation adopted from Ibrahim and Idem [66]:

$$\Delta T_{film,max} = \frac{L_c(r'_{A,obs})\Delta H_{rxn}}{h} \quad (2)$$

where $\Delta T_{film,max}$ is the upper limit of the temperature difference between the gas bulk and the pellet surface, L_c is the characteristic length, $r'_{A,obs}$ is the observed rate of reaction, h is the heat transfer coefficient (estimated from the correlation $J_H = J_D = \left(\frac{0.4548}{\varepsilon_p}\right) N_{Re}^{-1.4069}$, where J_H is the heat transfer J factor, $N_{pr} = \frac{CP\mu}{\lambda}$, and λ is the molecular thermal conductivity). The detailed calculation is shown in supplementary information. The J_D factor is given by the following correlations: $J_D = (\frac{0.4548}{\varepsilon_p}) N_{Re}{}^{-0.4069}$ (Geankoplis, 2003); $N_{Re} = \frac{d_p u \rho}{\mu(1-\varepsilon_p)}$. kc is the mass transfer coefficient obtained as, 7.34 m/s. The heat transfer coefficient, h, was determined to be 2.865×10^{-2} kJ/m^2.s.K. A value of 0.397 K was obtained for $\Delta T_{film,max}$ which shows that there was a small temperature variation between the bulk temperature and the temperature of the catalyst surface. The results confirm the absence of heat transfer limitations internally whereas an insignificant temperature gradient is observed externally. The detailed calculation is listed in (supplementary information, section-2). Additionally, a more rigorous criterion for determining the onset of heat transport limitation during reaction which was developed by Mears[72] was also used to

further ascertain the absence of heat transfer resistance as

$$\frac{r'_{A,obs}\rho_b R_c E\,\Delta H_{rxn}}{hT^2 R} < 0.15 \tag{3}$$

In substituting the numerical values for the terms on the left-hand side (LHS) of Eq. (1.3), a value of 2.93×10^{-4} is obtained, which is much less than 0.15. Hence, the heat transport limitation did not occur. The detailed calculation of Mears' criteria is presented in (supplementary information, section-3).

3.3.2. Mass Limitation. The internal pore mass transfer resistance was calculated using the Weisz–Prater criterion, adopted from Ibrahim and Idem[66], as given by:

$$C_{WP,ipd} = \frac{(-r'_{A,obs})\rho_c {R_c}^2}{D_{eff} C_{As}} < 1 \tag{4}$$

where, $C_{wp,ipd}$ is the Weisz–Prater criterion for internal pore diffusion, ρ_c is the pellet density, and Rc is the catalyst particle radius. The estimated value for $C_{wp,ipd}$ was 5.025×10^{-4}. This value is much less than 1. Thus, this result indicates that the concentration of reactant on the catalyst surface is more or less the same as the concentration within its pores. According to Fogler[67], this result is obtained as a consequence of the absence of internal pore diffusion limitations. A detailed calculation is shown in (supplementary information, section-4).

To determine whether film mass transfer resistance has any effect on the rate of reaction, the ratio of observed rate to the rate if film resistance exists was examined, as shown in.[73] Eq. (5) illustrates this criterion:

$$\frac{Observed\ rate}{Rate\ if\ film\ resistance\ controls} = \frac{-r'_{A,obs}}{C_{Ab} K_c}\frac{d_p}{6} \tag{5}$$

The estimated value for the ratio in Eq. (5) was calculated to be 3.89×10^{-5}. This result indicates that the observed rate is very much lower than the limiting film mass

transfer rate. Thus, the resistance to film mass transfer should not influence the rate of reaction.[73] A detailed calculation for this is shown in (supplementary information, section-5).

Mears' criterion[67] is often considered a more rigorous criterion for determining the onset of mass transport limitation in the film. Therefore, it was applied to determine if there was any mass transfer limitation during the collection of the kinetic data. This correlation is given as:

$$\frac{(-r'_{A,obs})\rho_c R_c n}{K_c C_{As}} < 0.15 \quad (6)$$

The value of the LHS of the equation is 8.16×10^{-5} which is far less than the RHS. Therefore, it can be concluded that there was no mass transport limitation in the film. A detailed calculation is shown in (supplementary information, section-6).

4. CONCLUSION

This study implied that the H-ZSM-5 mixed oxides have been found to exhibit superior performance for propane dehydrogenation due to the formation of highly dispersed Ga species in the as-synthesized materials. Combined XRD and H_2-TPR results demonstrated that the specific interaction between Ga and metal dopants can result in the formation of Cr, V and Ga-doped H-ZSM-5 catalysts in which the structural and surface redox properties are substantially modified. Compared to Ga/H-zsm-5, the as-prepared Cr/, and V/ doped H-ZSM-5 catalysts mixed oxide catalysts reveal dramatically enhanced activity for propane dehydrogenation. Our results show that the highest catalytic performance can be attained at a Cr/V-Ga/H-ZSM-5 catalyst which allows the steady

formation of a maximum propane conversion and propene selectivity of 69 and 78% , respectively in the catalytic dehydrogenation of propane at 550 °C.

REFERENCES

[1] I. Amghizar, L. A. Vandewalle, K. M. Van Geem, G. B. Marin, *Engineering* **2017**, *3*, 171–178.

[2] A. T. B. Jason Wu, Shaama Mallikarjun Sharada, Chris Ho, Andreas W.Hauser, MartinHead-Gordon, *Appl. Catal. A Gen.* **2015**, *506*, 25–32.

[3] T. Davies, S. H. Taylor, *Catal. Letters* **2004**, *93*, 151–154.

[4] J. Q. Chen, A. Bozzano, B. Glover, T. Fuglerud, S. Kvisle, *Catal. Today* **2005**, *106*, 103–107.

[5] Y.-M. Liu, W.-L. Feng, T.-C. Li, H.-Y. He, W.-L. Dai, W. Huang, Y. Cao, K.-N. Fan, *J. Catal.* **2006**, *239*, 125–136.

[6] K. Takehira, Y. Ohishi, T. Shishido, T. Kawabata, K. Takaki, Q. Zhang, Y. Wang, *J. Catal.* **2004**, *224*, 404–416.

[7] Y. Wang, Y. Ohishi, T. Shishido, Q. Zhang, W. Yang, Q. Guo, H. Wan, K. Takehira, *J. Catal.* **2003**, *220*, 347–357.

[8] K. Nakagawa, C. Kajita, K. Okumura, N. oki Ikenaga, T. Suzuki, K. Nakagawa, T. Ando, T. Suzuki, M. Nishitani-Gamo, T. Ando, et al., *J. Catal.* **2001**, *203*, 87–93.

[9] M. Chen, J. Xu, Y. M. Liu, Y. Cao, H. Y. He, J. H. Zhuang, *Appl. Catal. A Gen.* **2010**, *377*, 35–41.

[10] J. Ogonowski, E. Skrzyńska, *Catal. Letters* **2006**, *111*, 79–85.

[11] K. Nakagawa, C. Kajita, Y. Ide, M. Okamura, S. Kato, H. Kasuya, *Science (80-.).* **2000**, *64*, 215–221.

[12] D. Pietrogiacomi, M. C. Campa, S. Tuti, V. Indovina, *Appl. Catal. B Environ.* **2003**, *41*, 301–312.

[13] F. R. Chen, G. Coudurier, J. F. Joly, J. C. Vedrine, *Am. Chem. Soc. Div. Pet. Chem. Prepr.* **1991**, *36*, 878–886.

[14] K. Ridge, *Appl. Catal. A Gen.* **1996**, *145*, 267–284.

[15] J. C. Colmenares, A. Magdziarz, O. Chernyayeva, D. Lisovytskiy, K. Kurzydłowski, J. Grzonka, *ChemCatChem* **2013**, *5*, 2270–2277.

[16] Z. Shen, J. Liu, H. Xu, Y. Yue, W. Hua, W. Shen, *Appl. Catal. A Gen.* **2009**, *356*, 148–153.

[17] H. Ri, V. L. V Dqg, *React. kinet. catal. lett.* **2008**, *95*, 113–122.

[18] Y. Yan, S. Jiang, H. Zhang, *Sep. Purif. Technol.* **2014**, *133*, 365–374.

[19] E. Sarmini, I. Saptiama, H. Setiawan, *Atom Indones.* **2017**, *43*, 1–6.

[20] J. F. Joly, H. Ajot, E. Merlen, F. Raatz, F. Alario, Parameters Affecting the Dispersion of the Gallium Phase of Gallium H-MFI Aromatization Catalysts, **1991**.

[21] H. Ohtsuka, T. Tabata, O. Okada, L. M. F. Sabatino, G. Bellussi, *Catal. Lett.* **1997**, *44*, 265–270.

[22] B. Li, S. Li, N. Li, H. Chen, W. Zhang, X. Bao, B. Lin, *Microporous Mesoporous Mater.* **2006**, *88*, 244–253.

[23] J. Ahmadpour, M. Taghizadeh, *J. Nat. Gas Sci. Eng.* **2015**, *23*, 184–194.

[24] H. M. E.-K. and T. E. R. M. Samy El-Shall, Victor Abdelsayed, Abd El Rahman S. Khder, Hassan M. A. Hassan, Received, *J. Mater. Chem.* **2009**, *19*, 7625–7631.

[25] Y. Xu, J. Wang, Y. Suzuki, Z. Zhang, *"Applied Catal. A, Gen.* **2011**, *409–410*, 181–193.

[26] R. W. B. Iii, Y. H. Kim, A. Huffsmith, J. A. Reimer, E. Iglesia, *J. Phys. Chem. B* **1999**, *2*, 5787–5796.

[27] V. Abdelsayed, D. Shekhawat, M. W. Smith, *FUEL* **2015**, *139*, 401–410.

[28] M. Inaba, K. Murata, I. Takahara, K. I. Inoue, *Adv. Mater. Sci. Eng.* **2011**, *2012*, DOI 10.1155/2012/293485.

[29] Y. Chu, X. Gao, X. Zhang, G. Xu, G. Li, A. Zheng, *Phys. Chem. Chem. Phys.* **2018**, *20*, 11702–11712.

[30] L. Kubelkova, L. Brabec, M. Jeschke, R. Klik, J. Nova, J. Meusinger, D. Freude, V. Bosa, *Appl. Catal. A Gen.* **1998**, *167*, 309–320.

[31] J. E. B. and E. S. H. G. D. Meitzner, E. Iglesia, *Catalysis* **1993**, *140*, 209–225.

[32] F. Arena, F. Frusteri, G. Martra, S. Coluccia, A. Parmaliana, *J. Chem. Soc. - Faraday Trans.* **1997**, *93*, 3849–3854.

[33] M. Baltes, K. Cassiers, P. Van Der Voort, B. M. Weckhuysen, R. A. Schoonheydt, E. F. Vansant, *J. Catal.* **2001**, *197*, 160–171.

[34] I. Kainthla, G. V. Ramesh Babu, J. T. Bhanushali, R. S. Keri, K. S. Rama Rao, B. M. Nagaraja, *New J. Chem.* **2017**, *41*, 4173–4181.

[35] G. Mitran, R. Ahmed, E. Iro, S. Hajimirzaee, S. Hodgson, A. Urdă, M. Olea, I. C. Marcu, *Catal. Today* **2018**, *306*, 260–267.

[36] K. Jacob, E. Knozinger, S. Benfer, *J. CHEM. SOC. FARADAY TRANS* **1994**, *90*, 2969–2975.

[37] O. A. Syzgantseva, M. Calatayud, C. Minot, *J. Phys. Chem.* **2012**, *116*, 6636−6644.

[38] J. Kondo, Y. Sakata, K. Domen, K. Maruya, *J. CHEM. SOC. FARADAY TRANS* **1990**, *86*, 397–401.

[39] A. Rahman, M. Ahmed, *Stud. Surf. Sci. Catal.* **1996**, *100*, 419–426.

[40] B. Thirupathi, P. G. Smirniotis, *"Applied Catal. B, Environ.* **2011**, *110*, 195–206.

[41] A. Hakuli, M. E. Harlin, L. B. Backman, A. O. I. Krause, *J. Catal.* **1999**, *184*, 349–356.

[42] D. Zhang, L. Zhang, C. Fang, R. Gao, Y. Qian, L. Shi, J. Zhang, *RSC Adv.* **2013**, *3*, 8811–8819.

[43] M. Thommes, K. Kaneko, A. V. Neimark, J. P. Olivier, F. Rodriguez-Reinoso, J. Rouquerol, K. S. W. Sing, *Pure Appl. Chem.* **2015**, *87*, 1051–1069.

[44] N. Viswanadham, R. Kamble, M. Singh, M. Kumar, G. Murali Dhar, *Catal. Today* **2009**, *141*, 182–186.

[45] K. S. W. Sing, R. T. Williams, *Adsorpt. Sci. Technol.* **2004**, *22*, 773–782.

[46] Y. Yan, X. Wu, H. Zhang, *Sep. Purif. Technol.* **2016**, *171*, 52–61.

[47] B. M. Al-Swai, N. Osman, M. S. Alnarabiji, A. A. Adesina, B. Abdullah, *Ind. Eng. Chem. Res.* **2019**, *58*, 539–552.

[48] H. Wu, G. Pantaleo, V. La Parola, A. M. Venezia, X. Collard, C. Aprile, L. F. Liotta, *Appl. Catal. B Environ.* **2014**, *156–157*, 350–361.

[49] A. Jawad, F. Rezaei, A. A. Rownaghi, *Catal. Today* **2019**, DOI 10.1016/j.cattod.2019.06.004.

[50] V. R. Choudhary, *J. Catal.* **1997**, *18*, 188–195.

[51] V. De O. Rodrigues, J. G. Eon, A. C. Faro, *J. Phys. Chem. C* **2010**, *114*, 4557–4567.

[52] S. W. Choi, W. G. Kim, J. S. So, J. S. Moore, Y. Liu, R. S. Dixit, J. G. Pendergast, C. Sievers, D. S. Sholl, S. Nair, et al., *J. Catal.* **2017**, *345*, 113–123.

[53] Y. Ono, H. Kitagawa, Y. Sendoda, *J. Japan Pet. Inst.* **1987**, *30*, 77–88.

[54] S. B. Abdul Hamid, E. G. Derouane, P. Mériaudeau, C. Naccache, *Catal. Today* **1996**, *31*, 327–334.

[55] M. Raad, A. Astafan, S. Hamieh, J. Toufaily, T. Hamieh, J. D. Comparot, C. Canaff, T. J. Daou, J. Patarin, L. Pinard, *J. Catal.* **2018**, *365*, 376–390.

[56] I. Nowak, J. Quartararo, E. G. Derouane, J. C. Védrine, *Appl. Catal. A Gen.* **2003**, *251*, 107–120.

[57] A. Kant, Y. He, A. Jawad, X. Li, F. Rezaei, J. D. Smith, A. A. Rownaghi, *Chem. Eng. J.* **2017**, *317*, 1–8.

[58] Q. Wang, M. Zhu, H. Zhang, C. Xu, B. Dai, J. Zhang, *Catal. Commun.* **2019**, 33–37.

[59] M. De, D. Kunzru, *Catal. Letters* **2004**, *96*, 33–42.

[60] N. Mimura, M. Okamoto, H. Yamashita, S. Ted Oyama, K. Murata, *J. Phys. Chem. B* **2006**, *110*, 21764–21770.

[61] Y. Ohishi, T. Kawabata, T. Shishido, K. Takaki, Q. Zhang, Y. Wang, K. Takehira, *J. Mol. Catal. A Chem.* **2005**, *230*, 49–58.

[62] J. S. Gang Lv, Feng Bin, Chonglin Song , Kunpeng Wang, *Fuel* **2013**, *107*, 217–224.

[63] S. De Rossi, M. P. Casaletto, G. Ferraris, A. Cimino, G. Minelli, *Appl. Catal. A Gen.* **1998**, *167*, 257–270.

[64] A. A. Gabrienko, S. S. Arzumanov, I. B. Moroz, A. V. Toktarev, W. Wang, A. G. Stepanov, *J. Phys. Chem. C* **2013**, *117*, 7690–7702.

[65] T. Shishido, K. Shimamura, K. Teramura, T. Tanaka, *Catal. Today* **2012**, *185*, 151–156.

[66] H. H. Ibrahim, R. O. Idem, *Chem. Eng. J.* **2007**, *62*, 6582–6594.

[67] Fogler, H. S., *Elements of Chemical Reaction Engineering. 3rd Ed.*, Cliffs, NJ: Prentice-Hall., **1999**.

[68] Perry, R.H., &Green, D.W., *Perry's Chemical Engineer's Handbook. 7th Ed.*, New York: McGraw-Hill, **1997**.

[69] Geankoplis, C. H., Transport Processes and Separation Process Principles. 4th Ed., New York: Wiley, **2003**.

[70] E. Akpan, Y. Sun, P. Kumar, H. Ibrahim, A. Aboudheir, R. Idem, *Chem. Eng. Sci.* **2007**, *62*, 4012–4024.

[71] M. W. Stanley, Chemical-Process-Equipment-Selection-and-Design, **1990**.

[72] D. E. Mears, *Ind. Eng. Chem. Process Des.* **1971**, *10*, 541–547.

[73] O. Levenspiel, Chemical Reaction Engineering. An Introduction to the Design of Chemical Reactors., Wiley, New York, **1999**.

SUPPLEMENTARY INFORMATION

OXIDATIVE DEHYDROGENATION OF PROPANE OVER (Ga− , V− , Cr−) DOPED H-ZSM-5 IN PRESENCE AND ABSENCE CO_2

Abbas Jawad, and Ali A. Rownaghi*

Department of Chemical & Biochemical Engineering, Missouri University of Science and Technology, 1101 N. State Street, Rolla, Missouri 65409, United States

Section-1; Calculation of internal pore heat transfer resistance ($\Delta T_{particle,max}$).

Section-2; Calculation of external film heat transfer resistance ($\Delta T_{film,max}$).

Section-3;Calculation of Mears' criteria for heat transport limitation.

Section-4; Calculation of Weisz-Prater criterion for internal mass diffusion.

Section-5; Calculation of external film diffusion limitation.

Section-6; Calculation of Mears' criterion for external film diffusion limitation.

Section-1: Calculation of internal pore heat transfer resistance ($\Delta T_{particle,max}$).

Calculation of D_{AB}:

For a binary mixture of hydrocarbon and CO_2, non-polar components in a low-pressure system, the Brokaw equation has been referenced to calculate D_{AB}.[1] The Borkaw equation is as follows:

$$D_{AB} = \frac{0.001858T^{3/2}M_{AB}^{1/2}}{P\sigma_{AB}^2\Omega_D} \quad \text{(S-1.1)}$$

P = 1 atm; T = 550ºC = 823 K

M_{AB}; molecular weight (g/mol).

So, the correlations needed to calculate σ_{AB} & Ω_D are adopted[1]:

So, D_{AB}= 1.41× 10^{-6} m^2/s.

Calculation of D_{eff}:

D_{eff}; Effective mass diffusivity

$$D_{eff} = \frac{D_{AB}\varepsilon_P}{\tau} \tag{S-1.2}$$

ε_p = void fraction (the ratio of the volume occupied by voids to the total catalyst bed volume)

ε_p calculated using the following formula[2]:

$$\varepsilon_P = 0.38 + .073[1 + \frac{(d/dp-2)^2}{(d/dp)^2}] \tag{S-1.3}$$

d = ID of reactor = 12.7 ×10^{-3} m

d_p = diameter of particle = 0.5 ×10^{-6} m

shortest distance between those two points

actual distance a molecule travels between two points

τ = tortuosity[3][4][5]

$$\tau = 1 - 0.5\ln(\varepsilon_p) \tag{S-1.4}$$

So, D_{eff} = 4.259×10^{-7} m^2/s.

$$K_G = 10^{-7}(14.52T_r - 5.14)^{2/3}(\frac{Cp}{\lambda}) \tag{S-1.5}$$

$$\frac{\lambda_{eff}}{\lambda} = 5.5 + 0.05(N_{Re}) \tag{S-1.6}$$

Calculation of effectiveness thermal conductivity λ_{eff}:

Using Misic and Thodos [1] equations to calculate molecular thermal conductivity (λ):

$$N_{Re} = \frac{d_p u \rho}{\mu(1-\varepsilon_p)} \tag{S-1.7}$$

So, $\lambda_{eff}=2.447\times10^{-4}$ kW/m/K.

$$\Delta T_{particle,max} = \frac{D_{eff}(C_{As}-C_{Ac})\Delta H_{rxn}}{\lambda_{eff}} \tag{S-1.8}$$

$C_{Ac}=0$, and $C_{As}=C_{Ab}=1.014$ mol/m^3; $\Delta H_{rxn}=$ 164 kJ/mol [for oxidative of dehydrogenation of propane in the presence of carbon dioxide]

So, $\Delta T_{particle,max}$ =0.106 K

Section-2; Calculation of external film heat transfer resistance ($\Delta T_{film,max}$).

$$\Delta T_{film,max} = \frac{L_c(r'_{A,obs})\Delta H_{rxn}}{h} \tag{S-2.1}$$

$r'_{A,obs}$ =1.267 Kmol/m^3.s [Data taken from experimental run at T=823 K, W/F$_A$= 270 Kg$_{cat}$.s/Kmol]

R_c=radius of catalyst particle =0.25×10^{-6} m

L_c is the characteristic length =$R_c/3=0.25*10^{-6}/3$

ΔH_{rxn}=164 kJ/mol

h=heat transfer coefficient=2.865×10^{-2} kJ/m^2.s.K

T=550°C=823 K

R=molar gas constant=8.314 J/mol/K

So, $\Delta T_{film,max}$=0.397 K

Section-3; Calculation of Mears' criteria[6] for heat transport limitation.

$$\frac{r'_{A,obs}\rho_b R_c E\ \Delta H_{rxn}}{hT^2R} < 0.15 \qquad \text{(S-3.1)}$$

$r'_{A,obs}$ =1.267 Kmol/m^3.s [Data taken from experimental run at T=823 K, W/F_A= 270 Kg_{cat}.s/Kmol], H_{bed}=4.5×10^{-2} mm, height of bed.

$V_{bed} = \pi(\frac{d}{2})^2 H_{bed}$

Catalyst bulk density, $\rho_b = \frac{W_{cat}}{V_{bed}}$

ρ_b=52.65 Kg/m^3

R_c=radius of catalyst particle =0.25×10^{-6} m

E=4.1570 ×10^4 kJ/kmol.k

ΔH_{rxn}=164 kJ/mol

h=heat transfer coefficient=2.865×10^{-2} kJ/m^2.s.K

T=550ºC=823 K

R=molar gas constant=8.314 J/mol/K

2.93×10^{-4} << 0.15

Section-4; Calculation of Weisz-Prater criterion[1] for internal mass diffusion.

$$C_{WP,ipd} = \frac{(-r'_{A,obs})\rho_c {R_c}^2}{D_{eff}C_{As}} < 1 \qquad \text{(S-4.1)}$$

$r'_{A,obs}$ =1.267 Kmol/m^3.s [Data taken from experimental run at T=823 K, and W/F_A= 270 Kg_{cat}.s/Kmol].

Catalyst particle density= $\rho_c=\rho_b/\varepsilon_p$ =1160234 kg/m^3

Rc=radius of catalyst particle =0.25×10^{-6} m

D_{eff} = 4.259×10^{-7} m^2/s

C_{As} =Concentration of A in the catalyst surface = C_{Ab} = Concentration of A in the bulk= 0.37 mol/m^3 [because, there is no external (film resistance, so concentration of A in the bulk and concentration of A in the surface can be assumed same]

After calculating , I found that $C_{wp,ipd}$ ($5.025\times10^{-4}<<1$) far less than < 1. So, we can claim that there are no internal diffusion limitations and, consequently, no concentration gradient exists within the pellet.

Section-5; Calculation of external film diffusion limitation.[7]

$$\frac{Observed\ rate}{Rate\ if\ film\ resistance\ controls} = \frac{-r'_{A,obs}}{C_{Ab}\,K_c}\,\frac{d_p}{6} \qquad \text{(S-5.1)}$$

$r'_{A,obs}$ =1.211 Kmol/m^3.s [Data taken from experimental run at T=823 K, and W/F_A= 270 Kg_{cat}.s/Kmol].

dp= 0.5×10^{-6} m

C_{Ab} = 0.37 mol/m^3

K_c=7.34 m/s

$\frac{Observed\ rate}{Rate\ if\ film\ resistance\ controls}$ = 3.89×10^{-5}

The estimated value for the ratio is found to be much less than 1, so, then, the observed rate will be significantly less than the limiting film mass transfer rate. Thus, we can conclude that the resistance to film mass transfer should not influence the rate of reaction for the reaction in this study.[7]

Section-6; Calculation of Mears' criterion[6] for external film diffusion limitation.

Mears' criterion:

$$\frac{r'_{A,obs}\rho_b R_c E\ \Delta H_{rxn}}{hT^2R} < 0.15 \qquad \text{(S-6.1)}$$

$r'_{A,obs}$ =1.267 Kmol/m^3.s [Data taken from experimental run at T=823 K, W/F_A= 270 Kg_{cat}.s/Kmol].

Catalyst particle density= $\rho_c=\rho_b/\varepsilon_p$ =1160234 kg/m^3

Rc=radius of catalyst particle =0.25×10^{-6} m, n~0.7, and $^{K}{}_{c}$=7.34 m/s

C_{As} =Concentration of A in the catalyst surface = C_{Ab} = Concentration of A in the bulk= 0.37 mol/m^3 [because, there is no external (film resistance, so concentration of A in the bulk and concentration of A in the surface can be assumed same]

As, the LHS (8.16×10^{-5}<<0.15) of Mears' criterion is less than 0.15, we can claim that there will be no external (film) resistance to mass transfer during the kinetic study experiments in this research.

REFERENCES

[1] Perry, R.H., &Green, D.W., *Perry's Chemical Engineer's Handbook. 7th Ed.*, New York: McGraw-Hill, **1997**.

[2] Geankoplis, C. H., Transport Processes and Separation Process Principles. 4th Ed., New York: Wiley, **2003**.

[3] E. Akpan, Y. Sun, P. Kumar, H. Ibrahim, A. Aboudheir, R. Idem, *Chem. Eng. Sci.* **2007**, *62*, 4012–4024.

[4] H. H. Ibrahim, R. O. Idem, *Chem. Eng. J.* **2007**, *62*, 6582–6594.

[5] Fogler, H. S., *Elements of Chemical Reaction Engineering. 3rd Ed.*, Cliffs, NJ: Prentice-Hall., **1999**.

[6] D. E. Mears, *Ind. Eng. Chem. Process Des.* **1971**, *10*, 541–547.

[7] O. Levenspiel, Chemical Reaction Engineering. An Introduction to the Design of Chemical Reactors., Wiley, New York, **1999**.

SECTION

3. CONCLUSIONS AND RECOMMENDATIONS

3.1. CONCLUSIONS

Paper I, this work is an implying that bromine ions can be immobilized permanently on microstructure APS/Zr-PAI hollow fibers for utilization as bifunctional catalysts for the transformation of CO_2 to useful chemicals. The anchoring of catalytically active Br^- ions within porous Zr-PAIHFs promising powerful catalytic system that improved the catalytic activity of bifunctional catalyst without significant ZrO_2, amine, or bromine leaching. Successful fabrication of the Br/APS/Zr-PAIHF catalyst was accomplished with a range of microstructural properties consisted of a large number of interconnected cells or channels and high surface/volume ratios, which provide excellent mass transfer properties and low resistance to flow (and therefore low pressure drop) during flow reaction. Under reaction conditions tested, a 100% SO conversion and 98% SC selectivity were obtained. Nevertheless, our results revealed that a 100% enhancement in performance of catalyst could be realized after functionalization with APS and immobilization with Br ions. In addition, characterization of fibers after the reaction confirmed that the Br/APS/Zr-PAIHFs retained their chemical and physical structure and less degree of Br leaching was obtained. Such novel bifunctional catalyst can serve as a basis extending the use of hollow fibers as a support for other catalysts such as MOFs and as microfluidic reactors for continuous-flow reaction at mild conditions. This experimental study provides a unifying basis for implementing a novel environmentally friendly method

for production of styrene carbonate from CO_2 and SO under various reaction conditions with the purpose of achieving high activity and improved reusability.

Paper II, the catalytic activity of the (Mo, Fe, and pt) promoted Ni/Al_2O_3-CeO_2 (4 wt.% Ni) catalysts and prepared by the and impregnation method was investigated in the Dry reforming of methane. The Mo_x promotion significantly enhanced the physicochemical properties of the prepared catalysts even though All metal doped Ni-based Al_2O_3-CeO_2 catalysts showed slightly lower surface area than the Ni/Al_2O_3-CeO_2 catalyst and Al_2O_3-CeO_2 support. TPR profiles exhibited that Mo_x addition, improved the catalytic reducibility due to the reduction-oxidation potential. In addition, the ($PtFeMo/Ni/Al_2O_3$-CeO_2) catalyst possessed higher activity than others. The reactants conversions increased with increase in reaction temperature from 550 to 700 °C, due to the endothermic nature of the DRM reaction and showed the highest stability and resistance against coke deposition, due to the improvement of nickel dispersion and modification of the metal-support interaction.

Paper III, five Ni-based Al_2O_3-CeO_2 composite catalysts for DRM reaction have been prepared and studied. Four Pt, Fe, and Mg doped Ni-based Al_2O_3-CeO_2 catalysts were compared with Ni/Al_2O_3-CeO_2 catalyst and bare Al_2O_3-CeO_2 support. The physicochemical properties of all composite catalysts were characterized. All metal-doped Ni-based Al_2O_3-CeO_2 catalysts showed slightly lower surface area than the Ni/Al_2O_3-CeO_2 catalyst and Al_2O_3-CeO_2 support. Moreover, higher metal dispersion and catalysts reducibility were resulted through doping additional metals (Pt, Fe, and Mg) within the Ni-based Al_2O_3-CeO_2. Catalytic activity results revealed the the impact of trimetallic promoters on Ni-based Al_2O_3-CeO_2 catalyst and the highest conversion for methane

(>85%) and CO_2 (~90%), respectivitly and high selectivity towards H_2/CO ratio were obtained over Pt/MgFe/Ni/Al_2O_3-CeO_2 composite catalyst. The order of activity of the catalysts, based on the turnover frequencies, was Pt/MgFe/Ni/Al_2O_3-CeO_2>MgFe/Ni/Al_2O_3-CeO_2> PtFe/Ni/Al_2O_3-CeO_2> Fe/Ni/Al_2O_3-CeO_2>Ni/Al_2O_3-CeO_2.

Papers IV Herein, we reported the preparation ZSM-5 zeolite with various metal dopants (V, Cr, Ga) using wet impregnation technique. The catalytic behavior of these catalysts was evaluated in oxidative dehydrogenation of propane in presence and absence of CO_2 is presented atmosphere. Characterization results of the catalysts suggested that the physiochemical properties of the H-ZSM-5 were modified by incorporation of metal dopants. The catalytic results indicated that the product distribution varied with the type of metal doped, and that propane conversion was impact by the acidity of catalyst in the presence of CO_2. The NH_3-TPD, and catalytic evaluation results demonstrated that the metal-doped H-ZSM-5 possessed more weak to moderate-strong acid, which accounted for its superior catalytic performance. Unlike the lower methane ethylene selectivity, the amount of propene and BTX compounds were enhanced in the presence of CO_2 over all metal-doped H-ZSM-5. It seemed that high dispersion of gallium species which could increase the efficiency of gallium species played a crucial role in light alkane dehydrogenation reaction. Framework Al atoms of HZSM-5 was reported to be quite useful in dispersing Ga_2O_3 through their strong interaction with GaO_x species, which would enhance the Lewis acidity of gallia species as well as their abilities in activation of C-H bond of propane.

3.2. RECOMMENDATIONS

This study targeting the significant challenge in the development of sustainable processes to produce valuable chemicals is the identification and efficient use of renewable resources. Carbon dioxide (CO_2) can be considered an ideal building block and inexhaustibly available carbon source since it is a by-product of fuel combustion and of many industrial processes. To understand the mechanism these processes. Our recommendations, based on that, will be:

- Studying the affect each metal individually and then re-combination them.
- Studying effect, the connection the in-situ instruments to simulate the change inside the reactor such like X-ray absorption spectroscopy (XANES), temperature programmed reduction (TPR), X-Ray photoelectron spectroscopy (XPS), ^{27}Al MAS NMR and infrared (IR) spectroscopy of adsorbed pyridine …etc.
- A mechanism for the dehydrogenation is proposed, supported by physicochemical characterization, kinetic experiments and DFT (Density functional theory) calculations using the Vienna ab initio simulation package (VASP).
- Analysis of coke formation in details and coke consumption.
- Studying impact different type of zeolite with different network and acidity towards propene.

BIBLIOGRAPHY

[1] L. Nurrokhmah, T. Mezher, M. R. M. Abu-Zahra, *Environ. Sci. Technol.* **2013**, *47*, 13644–13651.

[2] M. A. Atanga, F. Rezaei, A. Jawad, M. Fitch, A. A. Rownaghi, *Appl. Catal. B Environ.* **2017**, *220*, 429–445.

[3] Z.-Z. Yang, Y. Zhao, G. Ji, H. Zhang, B. Yu, X. Gao, Z. Liu, *Green Chem.* **2014**, *16*, 3724.

[4] M. North, R. Pasquale, C. Young, *Green Chem.* **2010**, *12*, 1514.

[5] D. W. Kim, R. Roshan, J. Tharun, A. Cherian, D. W. Park, *Korean J. Chem. Eng.* **2013**, *30*, 1973–1984.

[6] C. Lucarelli, A. Vaccari, *Green Chem.* **2011**, *13*, 1941.

[7] E. G. Moschetta, N. A. Brunelli, C. W. Jones, *Appl. Catal. A Gen.* **2015**, *504*, 429–439.

[8] R. Srivastava, D. Srinivas, P. Ratnasamy, *Microporous Mesoporous Mater.* **2006**, *90*, 314–326.

[9] S. R. Jagtap, V. P. Raje, S. D. Samant, B. M. Bhanage, *J. Mol. Catal. A Chem.* **2007**, *266*, 69–74.

[10] X. Zhang, N. Zhao, W. Wei, Y. Sun, *Catal. Today* **2006**, *115*, 102–106.

[11] J. Ma, N. Sun, X. Zhang, N. Zhao, F. Xiao, W. Wei, Y. Sun, *Catal. Today* **2009**, *148*, 221–231.

[12] M. S. Fan, A. Z. Abdullah, S. Bhatia, *ChemSusChem* **2011**, *4*, 1643–1653.

[13] A. Al-Mamoori, A. Krishnamurthy, A. A. Rownaghi, F. Rezaei, *Energy Technol.* **2017**, *5*, 834–849.

[14] F. Magzoub, X. Li, J. Al-Darwish, F. Rezaei, A. A. Rownaghi, *Appl. Catal. B Environ.* **2019**, *245*, 486–495.

[15] J. Baltrusaitis, W. L. Luyben, *ACS Sustain. Chem. Eng.* **2015**, *3*, 2100–2111.

[16] Y. Wu, Y. He, T. Chen, W. Weng, H. Wan, *Appl. Surf. Sci.* **2006**, *252*, 5220–5226.

[17] S. a. Al-Ghamdi, H. I. De Lasa, *Fuel* **2014**, *128*, 120–140.

[18] J. Zhang, S. Lu, X. Su, S. Fan, Q. Ma, T. Zhao, *J. CO2 Util.* **2015**, *12*, 95–100.

[19] J. Klankermayer, S. Wesselbaum, K. Beydoun, W. Leitner, *Angew. Chemie - Int. Ed.* **2016**, *55*, 7296–7343.

[20] J. Klankermayer, W. Leitner, *Science (80-.).* **2015**, *350*, 629–630.

[21] C. Das Neves Gomes, O. Jacquet, C. Villiers, P. Thuéry, M. Ephritikhine, T. Cantat, *Angew. Chemie - Int. Ed.* **2012**, *51*, 187–190.

[22] P. G. Jessop, F. Joó, C. C. Tai, *Coord. Chem. Rev.* **2004**, *248*, 2425–2442.

[23] Q. Lu, J. Rosen, Y. Zhou, G. S. Hutchings, Y. C. Kimmel, J. G. Chen, F. Jiao, *Nat. Commun.* **2014**, *5*, 1–6.

[24] F. Roschangar, J. Colberg, P. J. Dunn, F. Gallou, J. D. Hayler, S. G. Koenig, M. E. Kopach, D. K. Leahy, I. Mergelsberg, J. L. Tucker, et al., *Green Chem.* **2017**, *19*, 281–285.

[25] J. Clark, D. Macquarrie, Handbook of Green Chemistry and Technology, **2002**.

[26] R. A. Sheldon, *Green Chem.* **2017**, *19*, 18–43.

[27] K. Huang, C. L. Sun, Z. J. Shi, *Chem. Soc. Rev.* **2011**, *40*, 2435–2452.

[28] N. Mac Dowell, P. S. Fennell, N. Shah, G. C. Maitland, *Nat. Clim. Chang.* **2017**, *7*, 243–249.

[29] G. Q. Chen, M. K. Patel, *Chem. Rev.* **2012**, *112*, 2082–2099.

[30] W. Leitner, J. Klankermayer, S. Pischinger, H. Pitsch, K. Kohse-Höinghaus, *Angew. Chemie - Int. Ed.* **2017**, *56*, 5412–5452.

[31] B. Schäffner, F. Schäffner, S. P. Verevkin, A. Börner, *Chem. Rev.* **2010**, *110*, 4554–4581.

[32] M. North, F. Pizzato, P. Villuendas, *ChemSusChem* **2009**, *2*, 862–865.

[33] T. Sakakura, J. C. Choi, H. Yasuda, *Chem. Rev.* **2007**, *107*, 2365–2387.

[34] B. Song, L. Guo, R. Zhang, X. Zhao, H. Gan, C. Chen, J. Chen, W. Zhu, Z. Hou, *J. CO2 Util.* **2014**, *6*, 62–68.

[35] S. Zhong, L. Liang, B. Liu, J. Sun, *J. CO2 Util.* **2014**, *6*, 75–79.

[36] R. Luo, X. Zhou, S. Chen, Y. Li, L. Zhou, H. Ji, *Green Chem.* **2014**, *16*, 1496–1506.

[37] J. W. Comerford, I. D. V. Ingram, M. North, X. Wu, *Green Chem.* **2015**, 1966–1987.

[38] J. A. Castro-Osma, M. North, W. K. Offermans, W. Leitner, T. E. Müller, *ChemSusChem* **2016**, *9*, 791–794.

[39] M. Peña-López, H. Neumann, M. Beller, *European J. Org. Chem.* **2016**, *2016*, 3721–3727.

[40] G. C. Chung, H. J. Kim, S. H. Jun, M. H. Kim, *Electrochem. commun.* **1999**, *1*, 493–496.

[41] J. Li, Y. Lin, H. Yao, C. Yuan, J. Liu, *ChemSusChem* **2014**, *7*, 1901–1908.

[42] C. Murugan, H. C. Bajaj, Indian J. Chem. - Sect. A Inorganic, Phys. Theor. Anal. Chem. **2010**, 49, 1182–1188.

[43] M. Yadollahi, H. Bouhendi, M. J. Zohuriaan-Mehr, H. Farhadnejad, K. Kabiri, *Polym. Sci. Ser. B* **2013**, *55*, 327–335.

[44] H. Zhang, H. B. Liu, J. M. Yue, *Chem. Rev.* **2014**, *114*, 883–898.

[45] M. North, R. Pasquale, *Angew. Chemie - Int. Ed.* **2009**, *48*, 2946–2948.

[46] D. J. Darensbourg, M. S. Zimmer, *Macromolecules* **1999**, *32*, 2137–2140.

[47] Y. Inoue, Y. Sasaki, H. Hashimoto, *J. Chem. Soc. Chem. Commun.* **1975**, 718–719.

[48] A. I. Adeleye, S. Kellici, T. Heil, D. Morgan, M. Vickers, B. Saha, *Catal. Today* **2015**, *256*, 347–357.

[49] J. Lauwaert, E. De Canck, D. Esquivel, J. W. Thybaut, P. Van Der Voort, G. B. Marin, *ChemCatChem* **2014**, *6*, 255–264.

[50] M. W. McKittrick, C. W. Jones, *J. Catal.* **2004**, *227*, 186–201.

[51] B. M. Bhanage, S. Fujita, Y. Ikushima, M. Arai, *Appl. Catal. A Gen.* **2001**, *219*, 259–266.

[52] A. Jawad, F. Rezaei, A. A. Rownaghi, *J. CO2 Util.* **2017**, *21*, 589–596.

[53] J. He, T. Wu, Z. Zhang, K. Ding, B. Han, Y. Xie, T. Jiang, Z. Liu, *Chem. - A Eur. J.* **2007**, *13*, 6992–6997.

[54] L. G. Ding, B. J. Yao, W. L. Jiang, J. T. Li, Q. J. Fu, Y. A. Li, Z. H. Liu, J. P. Ma, Y. Bin Dong, *Inorg. Chem.* **2017**, *56*, 2337–2344.

[55] H. Zhou, Y. M. Wang, W. Z. Zhang, J. P. Qu, X. B. Lu, *Green Chem.* **2011**, *13*, 644–650.

[56] M. Zhu, D. Srinivas, S. Bhogeswararao, P. Ratnasamy, M. A. Carreon, *Catal. Commun.* **2013**, *32*, 36–40.

[57] A. H. Jadhav, G. M. Thorat, K. Lee, A. C. Lim, H. Kang, J. G. Seo, *Catal. Today* **2016**, *265*, 56–67.

[58] A. Jawad, F. Rezaei, A. A. Rownaghi, *J. CO2 Util.* **2017**, *21*, 589–596.

[59] J. N. Appaturi, F. Adam, *Appl. Catal. B Environ.* **2013**, *136–137*, 150–159.

[60] V. B. Saptal, T. Sasaki, K. Harada, D. Nishio-Hamane, B. M. Bhanage, *ChemSusChem* **2016**, *9*, 644–650.

[61] F. Adam, J. N. Appaturi, E. P. Ng, *J. Mol. Catal. A Chem.* **2014**, *386*, 42–48.

[62] A. H. Jadhav, G. M. Thorat, K. Lee, A. C. Lim, H. Kang, J. G. Seo, *Catal. Today* **2016**, *265*, 56–67.

[63] F. M. Al-Qaisi, M. Nieger, M. L. Kemell, T. J. Repo, *ChemistrySelect* **2016**, *1*, 545–548.

[64] X. Wang, Y. Zhou, Z. Guo, G. Chen, J. Li, Y. Shi, Y. Liu, J. Wang, *Chem. Sci.* **2015**, *6*, 6916–6924.

[65] T. Ema, Y. Miyazaki, J. Shimonishi, C. Maeda, J. Y. Hasegawa, *J. Am. Chem. Soc.* **2014**, *136*, 15270–15279.

[66] Y. He, A. Jawad, X. Li, M. Atanga, F. Rezaei, A. A. Rownaghi, **2016**, *341*, 149–159.

[67] J. A. Kozak, J. Wu, X. Su, F. Simeon, T. A. Hatton, T. F. Jamison, *J. Am. Chem. Soc.* **2013**, *135*, 18497–18501.

[68] D. Liu, X. Y. Quek, W. N. E. Cheo, R. Lau, A. Borgna, Y. Yang, *J. Catal.* **2009**, *266*, 380–390.

[69] M. Levy, R. Levitan, E. Meirovitch, A. Segal, H. Rosin, R. Rubin, *Sol. Energy* **1992**, *48*, 395–402.

[70] S. Wang, G. Q. (Max) Lu, G. J. Millar, *Energy & Fuels* **1996**, *10*, 896–904.

[71] S. Wang, Z. H. Zhu, *Energy and Fuels* **2004**, *18*, 1126–1139.

[72] Y. Lou, M. Steib, Q. Zhang, K. Tiefenbacher, A. Horváth, A. Jentys, Y. Liu, J. A. Lercher, *J. Catal.* **2017**, *356*, 147–156.

[73] F. A. J. Al-doghachi, Y. Hin, *RSC Adv.* **2016**, *6*, 10372–10384.

[74] C. Courson, E. Makaga, C. Petit, A. Kiennemann, *Catal. Today* **2000**, *63*, 427–437.

[75] L. Yang, L. Pastor-pérez, S. Gu, A. Sepúlveda-escribano, T. R. Reina, *Appl. Catal. B Environ.* **2018**, *232*, 464–471.

[76] H. Ay, D. Üner, *Appl. Catal. B Environ.* **2015**, *179*, 128–138.

[77] S. Wang, G. . (Max) Lu, *Appl. Catal. B Environ.* **1998**, *19*, 267–277.

[78] J. Niu, X. Du, J. Ran, R. Wang, *Appl. Surf. Sci.* **2016**, *376*, 79–90.

[79] E. H. Yang, Y. S. Noh, S. Ramesh, S. S. Lim, D. J. Moon, *Fuel Process. Technol.* **2015**, *134*, 404–413.

[80] M. Yu, K. Zhu, Z. Liu, H. Xiao, W. Deng, X. Zhou, *Appl. Catal. B Environ.* **2014**, *148–149*, 177–190.

[81] A. Kant, Y. He, A. Jawad, X. Li, F. Rezaei, J. D. Smith, A. A. Rownaghi, *Chem. Eng. J.* **2017**, *317*, 1–8.

[82] F. Pompeo, N. N. Nichio, M. M. V. M. Souza, D. V. Cesar, O. A. Ferretti, M. Schmal, *Appl. Catal. A Gen.* **2007**, *316*, 175–183.

[83] X. Zhao, H. Li, J. Zhang, L. Shi, D. Zhang, *Int. J. Hydrogen Energy* **2016**, *41*, 2447–2456.

[84] M. C. J. Bradford, M. A. Vannice, *J. Catal.* **1999**, *183*, 69–75.

[85] A. M. O'Connor, Y. Schuurman, J. R. H. Ross, C. Mirodatos, *Catal. Today* **2006**, *115*, 191–198.

[86] Y. H. Hu, E. Ruckenstein, *Catal. Letters* **1996**, *36*, 145–149.

[87] U. Olsbye, T. Wurzel, L. Mleczko, *Ind. Eng. Chem. Res.* **1997**, *36*, 5180–5188.

[88] Y. Cui, H. Zhang, H. Xu, W. Li, *Appl. Catal. A Gen.* **2007**, *318*, 79–88.

[89] C. A. M. Abreu, D. A. Santos, J. A. Pacífico, N. M. L. Filho, *Ind. Eng. Chem. Res.* **2008**, *47*, 4617–4622.

[90] Y. J. O. Asencios, E. M. Assaf, *Fuel Process. Technol.* **2013**, *106*, 247–252.

[91] G. S. Gallego, F. Mondragón, J. Barrault, J. M. Tatibouët, C. Batiot-Dupeyrat, *Appl. Catal. A Gen.* **2006**, *311*, 164–171.

[92] J. H. Bitter, K. Seshan, J. A. Lercher, *J. Catal.* **1998**, *176*, 93–101.

[93] P. Djinović, J. Batista, A. Pintar, *Int. J. Hydrogen Energy* **2012**, *37*, 2699–2707.

[94] L. Pino, A. Vita, F. Cipitì, M. Laganà, V. Recupero, *Appl. Catal. B Environ.* **2011**, *104*, 64–73.

[95] S. Uhlig, R. Struis, H. Schmid-Engel, J. Bock, A. C. Probst, O. Freitag-Weber, I. Zizak, R. Chernikov, G. Schultes, *Diam. Relat. Mater.* **2013**, *34*, 25–35.

[96] A. Olafsen, C. Daniel, Y. Schuurman, L. B. Råberg, U. Olsbye, C. Mirodatos, *Catal. Today* **2006**, *115*, 179–185.

[97] J. Guo, H. Lou, H. Zhao, D. Chai, X. Zheng, *Appl. Catal. A Gen.* **2004**, *273*, 75–82.

[98] S. Sokolov, E. V. Kondratenko, M. M. Pohl, A. Barkschat, U. Rodemerck, *Appl. Catal. B Environ.* **2012**, *113–114*, 19–30.

[99] J. H. B. Rostrup-Nielsen, J. R.; Hansen, *J. Catal.* **1993**, *144*, 38–49.

[100] H. Wu, G. Pantaleo, V. La Parola, A. M. Venezia, X. Collard, C. Aprile, L. F. Liotta, *Appl. Catal. B Environ.* **2014**, *156–157*, 350–361.

[101] Z. Bian, S. Das, M. H. Wai, P. Hongmanorom, S. Kawi, *ChemPhysChem* **2017**, *18*, 3117–3134.

[102] N. H. Elsayed, N. R. M. Roberts, B. Joseph, J. N. Kuhn, *"Applied Catal. B, Environ.* **2015**, *179*, 213–219.

[103] I. Amghizar, L. A. Vandewalle, K. M. Van Geem, G. B. Marin, *Engineering* **2017**, *3*, 171–178.

[104] A. T. B. Jason Wu, Shaama Mallikarjun Sharada, Chris Ho, Andreas W.Hauser, MartinHead-Gordon, *Appl. Catal. A Gen.* **2015**, *506*, 25–32.

[105] J. Q. Chen, A. Bozzano, B. Glover, T. Fuglerud, S. Kvisle, *Catal. Today* **2005**, *106*, 103–107.

[106] M. A. Atanga, F. Rezaei, A. Jawad, M. Fitch, A. A. Rownaghi, *Appl. Catal. B Environ.* **2017**, *220*, 429–445.

[107] D. Pietrogiacomi, M. C. Campa, S. Tuti, V. Indovina, *Appl. Catal. B Environ.* **2003**, *41*, 301–312.

[108] F. R. Chen, G. Coudurier, J. F. Joly, J. C. Vedrine, *Am. Chem. Soc. Div. Pet. Chem. Prepr.* **1991**, *36*, 878–886.

[109] K. Ridge, *Appl. Catal. A Gen.* **1996**, *145*, 267–284.

[110] K. Takehira, Y. Ohishi, T. Shishido, T. Kawabata, K. Takaki, Q. Zhang, Y. Wang,

VITA

Abbas Jawad was born in Babylon, Iraq. He received his B.Sc. and M.Sc. degree in Chemical Engineering from University of Technology, Baghdad, Iraq in 2004 and 2007. He received his second Master of Science in Chemical and Biochemical Engineering from Missouri University of Science & Technology in June 2017.

He was granted a PhD scholarship by the Higher Committee for Education Development in Iraq in 2014. He joined Missouri University of Science and Technology in Fall Semester 2015.

Abbas Jawad was interested in converted carbon dioxide (CO_2) conversion into value-added chemicals and fuels. He presented his research at many conferences and published in many journals. He received his PhD in Chemical Engineering from Missouri University of Science & Technology in December 2020.